THE USE OF FRACTALS AND NON-FOSTER CIRCUITS FOR WIDEBAND METAMATERIALS AND ANTENNAS

by

Kathryn Leigh Smith

A thesis submitted to the faculty of
The University of North Carolina at Charlotte
in partial fulfillment of the requirements
for the degree of Master of Science in
Electrical Engineering

Charlotte

2015

Approved by:

_____

Dr. Ryan S. Adams

_____

Dr. Thomas P. Weldon

_____

Dr. Mehdi Miri

ABSTRACT

KATHRYN LEIGH SMITH. The use of fractals and non-Foster circuits for wideband metamaterials and antennas.
(Under the direction of DR. RYAN S. ADAMS)

Implementations of two methods for broadening the performance bandwidth of resonant electromagnetic structures are presented. The first method is the use of non-Foster loading elements, and the second method is the use of fractal geometries. Non-Foster loading is used in the context of negative permittivity and negative permeability metamaterials. A capacitively loaded strip unit cell with non-Foster loading is presented and the effects of parasitic resistances in the non-Foster element are explored, as well as the effect of variations in the test fixture. The unit cell is shown in simulation and measurement to exhibit sub-unity permittivity over a 133% bandwidth. A split ring resonator unit cell with non-Foster loading is presented next. The effects of parasitic resistance in the non-Foster element and variations in the test fixture are demonstrated for this unit cell, and the structure is shown in simulation to exhibit negative permeability over a bandwidth of 100%. Fractal geometries are utilized next, first in the context of a negative permittivity metamaterial unit cell, and then in the context of 3D-printable monopole antennas. The fractal metamaterial unit cell is shown to exhibit negative permittivity over a bandwidth of 6.4% in a coaxial test fixture, which is estimated, based on simulations, to correspond to a bandwidth of 32.9% in free space. Two fractal antennas are presented. The first is based on a branching cube pattern and is shown in simulation to have 181% bandwidth and poor polarization at high frequencies. The other is based on a branching cone pattern and shown in simulation and measurement to have 180% bandwidth, and in simulation to have considerably better polarization than the cubic version.

ACKNOWLEDGEMENTS

This material is based upon work supported by the National Science Foundation under Grant No. ECCS-1101939. Any opinions, findings, and conclusions or recommendations expressed in this material are those of the author(s) and do not necessarily reflect the views of the National Science Foundation.

My sincere thanks go to the following:

To Dr. Ryan Adams, for generously giving of his time and of his extensive technical and practical knowledge, both as a teacher and as a mentor, and for his unfailing patience and encouragement.

To Dr. Thomas Weldon, for many hours spent in the lab explaining ideas and theories, for sharing his practical insight and technical expertise, and for not discounting the improbable.

To Dr. Mehdi Miri, for serving on my committee.

To the other students who have worked with me in the lab - Josh, Varun, Darwino, John, Omar, Vandita, and Sam, for their collaboration in study and research, and for their friendship. They made me glad to come in every morning.

To the three sides of my family - the Smith family, the Bartholomew family, and the Rehobeth family - and also to the DeBoers, for their invaluable support and encouragement.

Finally, to Him who is from everlasting to everlasting, who formed the earth by the word of His power, who sustains the universe by His mighty hand, and who alone teaches man knowledge; to the LORD, my Redeemer - I will praise You as long as I have being, for You have dealt wondrously with me.

TABLE OF CONTENTS

LIST OF FIGURES

LIST OF TABLES

LIST OF ABBREVIATIONS

CLS	capacitively loaded strip
EDR	electric disk resonator
MUI	material under investigation
PEC	perfect electric conductor
PMC	perfect magnetic conductor
SRR	split ring resonator
TRL	thru-reflect-line

CHAPTER 1: INTRODUCTION

The desired behavior of many electromagnetic structures is closely tied to the resonant frequency of those structures, which results in a very narrow bandwidth of performance. This thesis presents three applications of two band-broadening techniques. The first utilizes non-Foster circuit elements to achieve broadband performance of negative permeability and permittivity metamaterial unit cells, the second utilizes fractal geometries to achieve broadband performance of a passive negative permittivity unit cell, and the third utilizes fractal geometries to achieve broadband performance of a monopole antenna.

1.1 Motivation

The development of broadband electromagnetic metamaterials has been driven by the potential they hold to provide otherwise unattainable control over electromagnetic fields. This control will enable the development of technologies such as magnetic conductors [1], electrically small antennas [2], perfect flat lenses [3], and invisibility cloaks [4].

The unique properties of materials having both negative permeability and negative permittivity were first presented by Veselago in 1968 [5]. At the time of his publication, no double-negative materials were known. Still, Veselago made several mathematical predictions about the behavior of such materials, such as a reversal of Snell's law and negative phase velocity. These predictions, and their potential applications, prompted the research community to begin investigating methods for achieving negative-index materials. The majority of the progress in this area has been in the development of electromagnetic metamaterials - materials composed of periodic arrays of electrically small but super-atomic structures that are used to deliberately

induce electromagnetic interaction ordinarily determined by the unalterable atomic properties of matter.

In November 1999, Pendry presented the first negative-permeability metamaterial [6]. This metamaterial was composed of an array of concentric C-shaped conductive resonators, or split rings, and displayed negative permeability over a narrow band of frequencies near resonance. The first measurement of a double-negative material, composed of split ring resonators to provide negative permeability and conductive strips to provide negative permittivity, was presented less than a year later, in May 2000 [7]. However, the frequency range of the negative index behavior was very narrow (approximately 4.70 GHz to 5.15 GHz, or 9%).

Since the utility of many metamaterial applications, such as cloaking and beam focusing, would be severely hampered by the naturally narrow bandwidth of these metamaterials, many researchers have turned their attention to developing methods for widening the band of operation. One method that has been proposed to achieve broadband metamaterials is to include non-Foster loading in each unit cell to cancel the intrinsic reactance of the structure [8]. As will be shown, the result of such loading is to maintain the performance of the unit cell over a band limited only by the quality of the match between the non-Foster load and the intrinsic impedance of the unit cell [9]. Another method for achieving broadband performance is the inclusion of fractal geometries. This allows multiple resonances to appear at various frequencies, repeating the desired behavior at each resonance and collectively resulting in broadband performance. Fractal geometries can also be used to increase the operating bandwidth of antennas.

The driving force behind broadband antenna development is the increasingly ubiquitous use of wireless communication. Thousands of everyday applications, from radio and cellular communication to bluetooth and wi-fi, require antennas to send and receive information. Every application has an assigned frequency spectrum, within

which individual signals must find frequencies where noise from other nearby users will not drown the signal. Multiple closely-spaced antennas will conflict with one another, as cross-talk between the various systems creates noise and even changes the antenna radiation patterns. The ability to integrate multiple communication systems and consolidate to a single antenna resolves these issues, however, it requires that the single antenna be able to operate over a broad range of frequencies.

1.2 Topic Overview

Chapter 2 of this thesis provides some general background information about metamaterials, non-Foster loading, and fractals in electromagnetics. Reversal of Snell's law and opposing phase and group velocity are demonstrated for double-negative materials through simulation.

Chapter 3 presents research results for non-Foster loading of two unit cell geometries: the capacitively loaded strip and the split ring resonator. The capacitively loaded strip, or CLS, is a resonant structure first suggested by Ziolkowski in [10]. The structure produces a negative electric susceptibility over a very narrow band of frequencies above resonance. A detailed mathematical analysis of the structure is given in [10], and a very similar three-dimensional structure is analyzed in [8]. This chapter will present a simulated CLS unit cell loaded with an ideal negative inductance, to show the wideband response, and also to show that negative permittivity is tunable by varying the load impedance. A mathematical model for a unit cell loaded with a non-Foster circuit having parasitic resistances is developed, and calculated, simulated, and measured results for the unit cell with a non-ideal load are presented. Portions of this material have been published previously, in [9].

The split ring resonator, or SRR, is a resonant structure first suggested by Pendry in [6] that produces a negative magnetic susceptibility over a very narrow band of frequencies above resonance. This was the negative permeability structure utilized in the first measurement of a double-negative material, presented in [11]. A detailed

mathematical analysis of the structure is given in [10] and [12]. To overcome the bandwidth limitations of this structure, [8] suggests loading the resonator with a non-Foster circuit designed to nullify the intrinsic reactance of the unit cell. This chapter will present a simulated split ring resonator unit cell loaded with an ideal negative capacitance, to show the wideband response, and also to show that the permeability of the unit cell is tunable by changing the load impedance. A mathematical model for a unit cell loaded with a non-Foster circuit having parasitic resistances is developed, and calculated and simulated results for the unit cell with a non-ideal load are presented.

This chapter will also present a novel nearly-hollow coaxial metamaterial test fixture. This fixture and its calibration standards are made up of a set of 3D printable pieces, which are covered with copper foil to achieve conductivity over the surfaces of the inner and outer tubes. The specific details of the printed pieces are presented, along with several control measurements, to demonstrate the continuity of measured and simulated results.

Chapter 4 introduces a novel negative permittivity unit cell that utilizes fractal methods to achieve broadband performance. Portions of this material have been published in [13]. One of the most effective unit cell geometries to achieve negative permittivity is the electric disk resonator (EDR) [8]. This structure provides a large surface to interact with the incident electric field, and often exhibits a moderate frequency range over which an effective negative permittivity is attainable. Unfortunately, this structure is not easily manufactured because of its three dimensional shape. To simplify manufacturing and implementation, this structure may be approximated with a capacitively loaded strip [10], which is simply a two-dimensional rendering of the three-dimensional geometry. This 2D structure has been explored and found to effectively induce negative permittivity, although its bandwidth is narrower, and the field interaction is weaker, than the three-dimensional version.

To broaden the bandwidth of the CLS structure, [14] proposed a fractal expansion

of the basic I-shape with additional replicas of this shape that would resonate at different frequencies. Unfortunately, the proposed fractal structure lacked continuous bandwidth, instead exhibiting multiple bands over which the desired response was achieved. In this chapter, the work of [14] and [15] is combined, with modification of the individual lengths of each part of the geometry, as well as the addition of discrete capacitively coupled resonators that broaden the bandwidth of this structure.

This chapter also presents a comparison of several results in parallel plate, coaxial, and rectangular waveguide test environments, and explains in detail the key attributes of each case. Measurement results for metamaterials located in coaxial and rectangular waveguides are related to parallel plate results via simulation.

Chapter 5 presents a broadband fractal tree monopole antenna. Portions of this material have been published in [16]. Dipole antennas are widely utilized in communication applications, because they have excellent cross-polarization and a symmetric radiation pattern. They radiate over a very narrow band, typically at the frequency where the length of the antenna is half of the wavelength. However, dipoles typically require complicated feed structures, such as baluns, to balance the feed to the two sides of the antenna [17]. Monopole antennas overcome this complication by using a ground plane to mirror a single radiating element, emulating the behavior of a dipole without the necessity of feeding two sides. Monopole antennas are attractive alternatives to dipoles because of their simple construction and because they are smaller than dipoles without sacrificing a dipole's excellent cross-polarization and symmetric radiation pattern. However, like dipoles, they also are extremely narrowband. The antennas presented here have a monopole configuration, but use fractal methods to improve the bandwidth.

Chapter 6 concludes this document with a summary of presented results for each of the topics covered in the preceding chapters. Several recommendations for further lines of inquiry are also presented.

CHAPTER 2: BACKGROUND

2.1 Metamaterials

Relative electric permittivity and magnetic permeability are macroscopic material parameters that are derived from atomic scale phenomena (the electric and magnetic moments of atoms). The relative permittivity ϵ_r of a given material is modeled as [18]:

$$\epsilon_r = 1 + \chi_e \tag{2.1}$$

where χ_e is the electric susceptibility, defined by the following equation:

$$\vec{P}_e = \epsilon_0 \chi_e \vec{E}_a. \tag{2.2}$$

In this equation, $\vec{P}_e$ is the electric dipole moment per unit volume, or polarization, ϵ_0 is the electric permittivity of free space, equal to 8.854×10^{-12} $\frac{C^2}{N \cdot m^2}$, and $\vec{E}_a$ is the applied electric field. Similarly, the relative permeability is can be modeled by:

$$\mu_r = 1 + \chi_m \tag{2.3}$$

where χ_m is the magnetic susceptibility, defined by the following equation:

$$\vec{M} = \chi_m \vec{H}_a \tag{2.4}$$

where $\vec{M}$ is the magnetic dipole moment per unit volume, or magnetization, and $\vec{H}_a$ is the applied magnetic field [17]. The permeability and permittivity of a normal material thus depend only on the atomic properties of that material, and cannot be changed at will. The premise of metamaterial engineering is that the scale of the unit

that produces $\vec{P}_e$ and $\vec{M}$ need not be atomic - indeed, that the absolute scale of that unit is irrelevant. Rather, the only limit on the size of the unit cell is relative to the wavelength of the applied field. Engineered "materials" of this sort, constructed of periodic arrays of *electrically small* unit cells, are called "metamaterials".

Maxwell's equations, which govern the behavior of electric and magnetic phenomena, are given below, assuming time harmonic fields ($\sim e^{j\omega t}$).

$$\nabla \times \vec{E} = -j\omega\vec{B} \tag{2.5}$$

$$\nabla \times \vec{H} = j\omega\vec{D} + \vec{J} \tag{2.6}$$

$$\nabla \cdot \vec{D} = \rho \tag{2.7}$$

$$\nabla \cdot \vec{B} = 0 \tag{2.8}$$

where $\vec{E}$ is the electric field in Volts per meter, $\vec{H}$ is the magnetic field in Amperes per meter, $\vec{J}$ is the electric current density in Amperes per square meter, and ρ is the electric charge density in Coulombs per square meter. The magnetic flux density $\vec{B}$ and electric flux density $\vec{D}$ are related to the relative permeability and permittivity through the constitutive relations, which for a non-dispersive medium are given by:

$$\vec{B} = \mu_0\mu_r\vec{H} \tag{2.9}$$

and

$$\vec{D} = \epsilon_0\epsilon_r\vec{E} \tag{2.10}$$

where μ_0 is the magnetic permeability of free space, equal to $4\pi \times 10^{-7}\ \frac{T \cdot m}{A}$, and ϵ_0 is the electric permittivity of free space, equal to $8.854 \times 10^{-12}\ \frac{C^2}{N \cdot m^2}$ [18].

If the values of μ_r and ϵ_r may be either positive or negative, there are four possible combinations, as shown in Fig. 2.1. Note that both μ_r and ϵ_r may also potentially

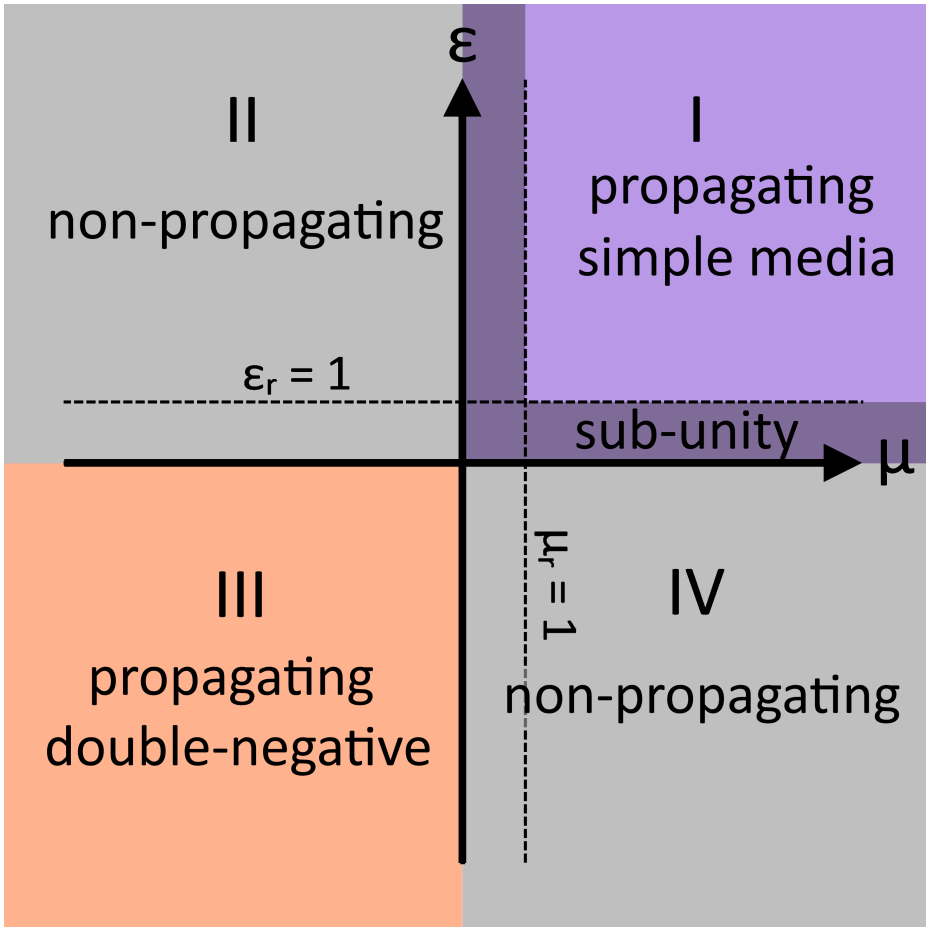

Figure 2.1: The four possible sign combinations of μ_r and ϵ_r.

be complex, which introduces many other possible combinations. For the sake of this discussion, only the lossless case is considered, where μ_r and ϵ_r are purely real. Quadrants I and III of Fig. 2.1 represent materials in which an electromagnetic wave may propagate, and quadrants II and IV represent materials in which an electromagnetic wave may not propagate.

To demonstrate this point, consider the case of a plane wave traveling in a lossless dielectric, with electric field given by $\vec{E} = E_\circ e^{-j\beta r}\vec{a_E}$, where $E_\circ$ is the amplitude of the electric field, r is the spacial dimension in which the wave is propagating, $\vec{a_E}$ is a unit vector perpendicular to the direction of propagation, pointing in the direction of electric field oscillation, and β is the propagation constant, given by $\beta = \omega\sqrt{\mu_r\epsilon_r}/c$,

where c is the speed of light in a vacuum, approximately equal to 3×10^8 m/s. Clearly, if both μ_r and ϵ_r have the same sign, as in quadrants I and III of Fig. 2.1, β is a real number, and $\vec{E}$ represents a propagating wave. However, if either μ_r or ϵ_r is negative, while the other is positive, as in quadrants II and IV of Fig. 2.1, β is purely imaginary, and the wave represented by $\vec{E}$ becomes evanescent. No known naturally occurring materials fall in quadrant III [11].

In 1964, Veselago posited that if a material could be created that had simultaneously negative permeability and permittivity, such "double-negative" materials would have several unique properties, such as a left-handed $\vec{E}$, $\vec{H}$, $\vec{k}$ triplet, negative index of refraction, and phase velocity in the opposite direction of the Poynting vector [5].

The index of refraction of a given material is defined by:

$$n = \pm\sqrt{\mu_r\epsilon_r} \tag{2.11}$$

where μ_r and ϵ_r are the relative permeability and permittivity of the material. Veselago showed that for a left handed medium, in which both μ_r and ϵ_r are negative (quadrant III of Fig. 2.1), the negative root of n must be chosen. The time-averaged pointing Poynting vector, which indicates the direction of power flow, is given by:

$$\vec{S}_{av} = \frac{1}{2}Re\{\vec{E}\times\vec{H}^*\} \tag{2.12}$$

where $\vec{E}$ is the electric field vector, and $\vec{H}^*$ is the complex conjugate of the magnetic field vector. The phase velocity $\vec{v}_{ph}$ of a plane wave travelling in a medium is given by:

$$\vec{v}_{ph} = \frac{c}{n}\frac{\vec{S}_{av}}{|\vec{S}_{av}|} \tag{2.13}$$

where c is the speed of light in a vacuum. The propagation vector $\vec{k}$ is given by:

$$\vec{k} = \frac{\omega}{|\vec{v}_{ph}|^2}\vec{v}_{ph} \tag{2.14}$$

where ω is the angular frequency, equal to 2π times the frequency in Hz.

It can be seen from these equations that, for a plane wave traveling in a medium, changing the sign of n will change the direction of phase velocity, but not the direction of power flow. This principle is demonstrated in Fig. 2.2. This figure shows the magnitude of the electric field in a parallel plate waveguide. The waveguide is divided into three sections. The left-hand and right-hand sections are filled with a vacuum, where $\epsilon_r = 1$, $\mu_r = 1$, and $n = 1$. The middle section is filled with a material where $\epsilon_r = -1$, $\mu_r = -1$, and $n = -1$. The phase of the excitation is varied from 0° (top) to 180° (bottom), in steps of 30°. The wave is excited at the left side of the plot, and it can be observed in the progression from the top plot to the bottom plot that the phase moves from left to right (positive phase velocity) in the left-hand and right-hand sections, but from right to left (negative phase velocity) in the center section. Power flow, indicated by the direction of $\vec{S}_{av}$, is consistently directed to the right.

Snell's law for refraction of light at an interface between two materials is given by:

$$\frac{\sin\theta_i}{\sin\theta_t} = \frac{n_2}{n_1} \tag{2.15}$$

or

$$\theta_t = \sin^{-1}\left(\frac{n_1}{n_2}\sin\theta_i\right) \tag{2.16}$$

where n_1 is the index of refraction in the first medium, n_2 is the index of refraction in the second medium, θ_i is the incident angle, measured between the direction of propagation in the first medium and the normal to the plane of incidence, and θ_t is the transmitted angle, measured between the direction of propagation in the second medium and the normal to the plane of incidence. The direction of propagation is given by the Poynting vector. By definition, positive θ_t is located on the opposite side of the normal from the incident wave. There is also a reflected wave, at angle $\theta_r = \theta_i$ on the opposite side of the normal from the incident wave. This is visually

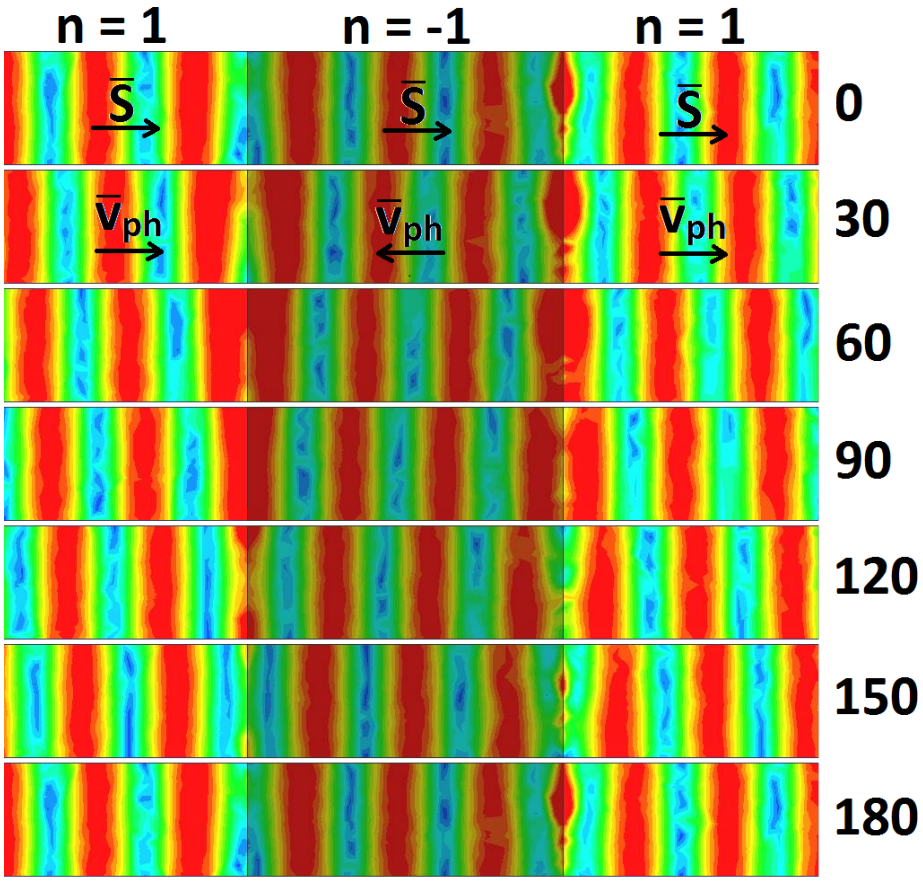

Figure 2.2: Effect of a chunk of $n = -1$ material on v_{ph}.

depicted in Fig. 2.3, where $\vec{S}_i$, $\vec{S}_r$, and $\vec{S}_t$ are the time-averaged Poynting vectors of the incident wave, the reflected wave, and the transmitted wave, respectively. The range of θ_i is $[0°, 90°)$, because of the way that θ_i is defined. The range of $\sin(\theta_i)$, then, is $[0, 1)$, and the range of θ_t for $n_1, n_2 > 0$ or $n_1, n_2 < 0$, is $[0°, 90°]$. In order to bend light past the normal, into the range $\theta_t = [-90°, 0°)$, transmission must be from a left-handed material ($n < 0$) into a right-handed material ($n > 0$), or vice versa.

Figure 2.4 demonstrates this phenomenon. Figure 2.4 (a) shows a plane wave propagating in a vacuum, where $\theta_i = 45°$, incident upon a $n = 1 : n = 2$ boundary. The magnitude of $\vec{E}$ is plotted as a color gradient, and the direction of $\vec{S}_{av}$ is plotted as a grid of black arrows. Based on (2.16), the transmitted wave should have $\theta_t = 20.7°$.

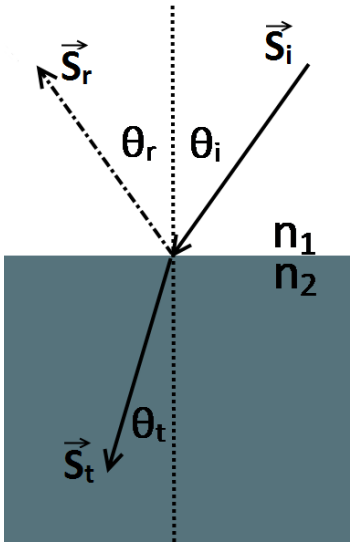

Figure 2.3: Snell's law diagram for transmission and reflection of a ray of light at a dielectric interface.

Though the exact numerical analysis is lacking in the figure, it is clear that the direction of propagation in the second medium has bent toward the normal, when compared to the direction of propagation in the first medium. Figure 2.4 (b) shows a plane wave propagating in a vacuum, where $\theta_i = 45°$, incident upon a $n = 1 : n = -2$ boundary. Again, the magnitude of $\vec{E}$ is plotted as a color gradient and the direction of $\vec{S}_{av}$ is plotted as a grid of black arrows. From (2.16), we expect the transmitted wave to propagate at an angle of $\theta_t = -20.7°$, at the same magnitude as the previous figure, but on the opposite side of the normal. It is clearly shown in Fig. 2.4 (b) that transmission from a $n > 0$ material to a $n < 0$ material caused the direction of propagation to bend past the normal, into the $\theta_t < 0$ region. It is also noted that the $\vec{k}$ vector in the second medium points opposite to propagation, as predicted.

Figure 2.5 shows the behavior of a wave travelling in a vacuum incident upon a single-negative medium. Figure 2.5 (a) shows a wave with $\theta_i = 45°$ incident upon a medium with $\mu_r = -2$, $\epsilon_r = 2$, so that $n = -j2$. Figure 2.5 (b) shows a wave with $\theta_i = 45°$ incident upon a medium with $\mu_r = 2$, $\epsilon_r = -2$, so that $n = -j2$. These are quadrant II and quadrant IV materials, which do not support wave propagation. As

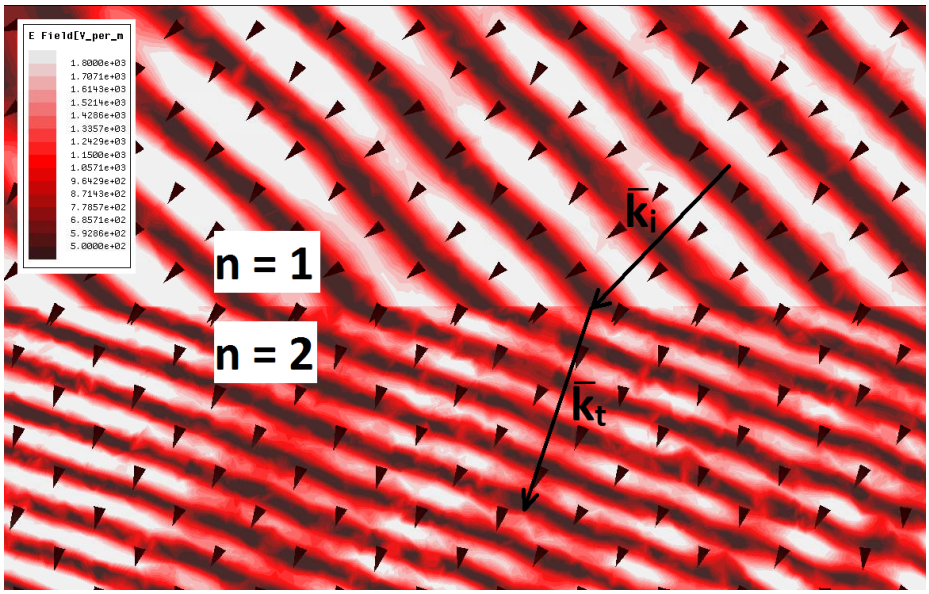

(a)

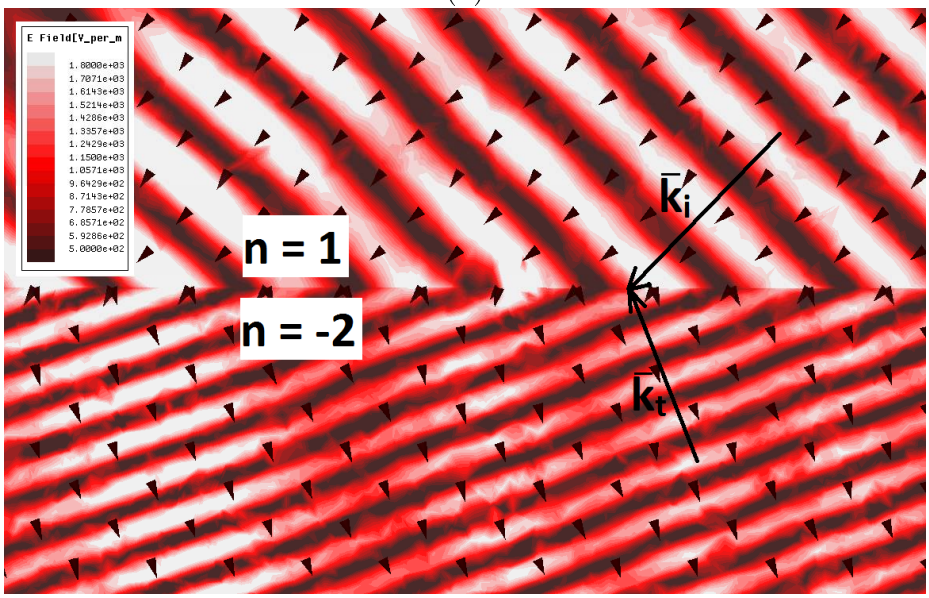

(b)

Figure 2.4: (a) A plane wave incident upon a $n = 1 : 2$ boundary. (b) A plane wave incident upon a $n = 1 : -2$ boundary. The time-averaged Poynting vector is given by the grid of small black arrows

shown, in both cases the wave quickly decays upon incidence with the imaginary-index material, and ultimately reflects back into the first medium, creating the interference pattern shown.

Double-negative materials are shown to enable heretofore impossible manipulation

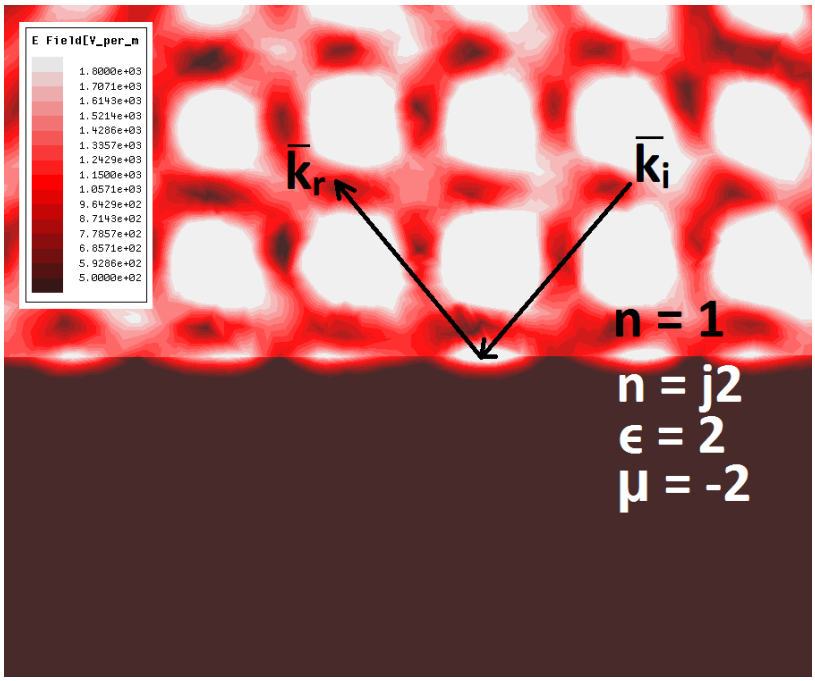

(a)

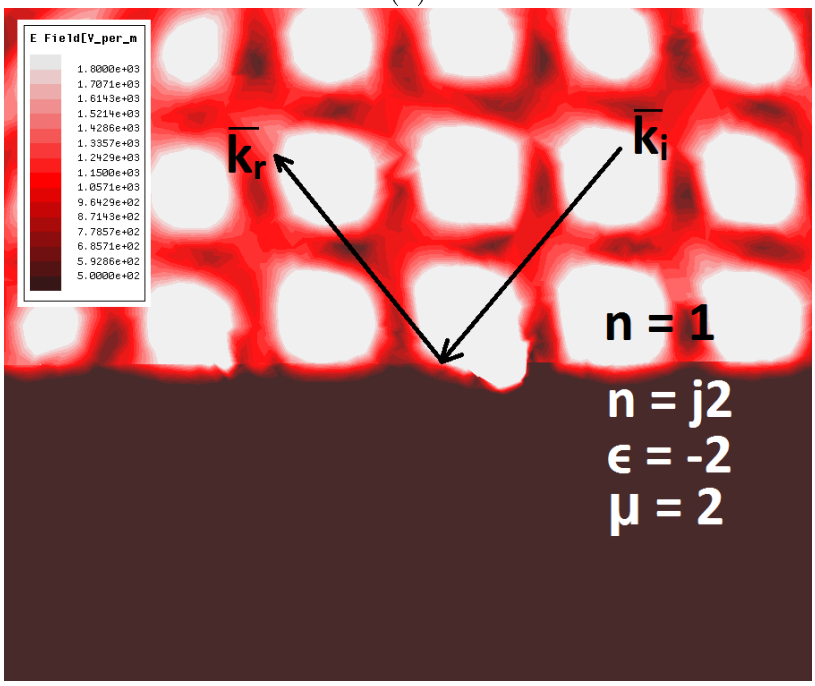

(b)

Figure 2.5: (a) A plane wave incident upon a $n = 1 : j2$ boundary, where $\mu_r = -2$ and $\epsilon_r = 2$ (Quadrant II). (b) A plane wave incident upon a $n = 1 : j2$ boundary, where $\mu_r = 2$ and $\epsilon_r = -2$ (Quadrant IV).

of electromagnetic fields. Many practical applications for such materials have been proposed, such as perfect flat lenses [3], electromagnetic cloaking [19], and wideband

artificial magnetic conductors [1], as well as more speculative applications, such as time reversal [20] and history editing [21].

Since no known double-negative materials exist in nature to allow realization of these propositions, the development of metamaterials to achieve negative permittivity and negative permeability has become a topic of extensive research. Several resonant structures have been proposed that exhibit negative parameters. One such structure is the split ring resonator, which exhibits negative permeability at frequencies slightly above resonance [6]. Another is the capacitively loaded strip, which exhibits negative permittivity at frequencies slightly above resonance [10]. A double-negative metamaterial was first measured in 2000, using SRRs and copper wire strips [7].

2.2 Non-Foster Loading of Metamaterials

Because the desired behavior of the structures being used to achieve negative permeability and permittivity is so closely tied to the resonance of the intrinsic capacitance and inductance of the structure, it naturally occurs over a tightly limited frequency band. It is desireable for many applications to find means of broadening the band of performance.

Foster's reactance theorem states that the reactance of any passive, lossless network composed solely of inductors and capacitors strictly increases with frequency [22]. A non-Foster element such as a negative capacitor or negative inductor is an active circuit that provides a port across which reactance decreases with frequency. Such a circuit operates by inverting the impedance of a loading element, and is characterized as a negative capacitor or a negative inductor, depending on the nature of the loading element [23].

In theory, non-Foster circuits lend themselves quite naturally to the problem of creating broadband metamaterials. By inserting negative inductance and capacitance into a metamaterial structure, the intrinsic reactance of that structure may be minimized across a wide band, rather than solely at the natural resonance [8]. Thus, the

desired behavior can be achieved across a frequency band that is limited only by the quality of the match between the natural impedance of the metamaterial structure and the non-Foster load impedance. In practice, the appropriate non-Foster values are often difficult to ascertain, and the non-Foster circuits themselves are prone to instability and variation over frequency. Such circuits also inevitably possess parasitic resistance, which further limits the bandwidth of the desired performance [9, 24–26].

2.3 Fractal Metamaterials and Antennas

Another method that has been proposed for creating broadband metamaterials is to utilize the self-similarity of fractals. A fractal is a shape that is formed of an infinite succession of progressively smaller iterations of some geometric motif. The word "fractal" was coined by Mandelbrot, from the Latin *fractus*, meaning "broken". However, the existence of infinitely jagged, non-differentiable geometries in nature had been noted decades earlier by Jean Perrin, who found such geometries in the path of particles undergoing Brownian motion [27], and by Lewis Fry Richardson, who found that the measured length of a coastline depends on the length of the unit with which it is measured [28].

Fractals also occur quite often in plant growth patterns. For example, Fig. 2.6 shows a head of Romanesco broccoli, which exhibits fractal behavior in the repetition of the vaguely conical shape of the broccoli head in smaller conical elements repeated in a spiral around the head. Each of these conical elements are likewise composed of a spiral of conical components that are smaller yet. Figure 2.7 shows a fern frond, which exhibits similar repetition of the overall shape of the structure at several increasingly minuscule scales.

Several mathematical algorithms have been proposed to generate various numerical fractals, such as the Koch [31], Sierpinski [32] and Mandelbrot [27] fractals. A true mathematical fractal has an infinite number of iterations, and is infinitely long, though it fits in a bounded space. This space-filling property of fractal geometries

Figure 2.6: A head of Romanesco broccoli [29].

Figure 2.7: A fern frond [30].

has often been utilized in electromagnetics to miniaturize resonant structures, both metamaterials and antennas. The property of self-similarity is also useful, since it allows currents to set up in the entirety of the structure (at low frequencies) or in part of the structure (at high frequencies) while maintaining similar radiation and resonant properties. This property is demonstrated quite clearly in [33], using a Sierpinski monopole antenna. These multiple resonant bands may be engineered to occur at closely spaced frequencies. The desired behavior, being repeated at each reso-

nance, is thus maintained across the band. This property is exploited in [14, 34, 35], among others, to achieve wideband and multiband performance in metamaterials. Fractal geometries are also exploited to miniaturize or improve the bandwidth of loop antennas [36], monopole antennas [37–39], and dipole antennas [40].

CHAPTER 3: NON-FOSTER LOADED METAMATERIALS

The development of wideband metamaterials has been driven by the potential they hold to provide otherwise unattainable control over electromagnetic fields. This control will enable the development of technologies such as wideband magnetic conductors [1], electrically small antennas [2], perfect flat lenses [3], and invisibility cloaks [4]. One method that has been proposed to achieve wideband performance is the inclusion of fractal geometries, to provide resonance at several closely related frequencies [41]. Another is to use non-Foster loading to cancel the intrinsic reactance of the unit cell [8], which is the method explored in this chapter. As will be shown, the result of such loading is to maintain the performance of the unit cell over a band limited only by the quality of the match between the non-Foster load and the intrinsic impedance of the unit cell [9]. Two unit cell geometries are explored: the capacitively loaded strip and the split ring resonator.

The CLS is a resonant structure first suggested by Ziolkowski in [10]. The structure produces a negative electric susceptibility over a very narrow band of frequencies above resonance. A detailed mathematical analysis of the structure is given in [10], and a very similar three-dimensional structure is analyzed in [8]. To overcome the bandwidth limitations of the structure, [8] suggests loading the CLS with a non-Foster circuit designed to cancel the intrinsic reactance of the unit cell. This chapter will present a simulated capacitively loaded strip unit cell loaded with an ideal negative capacitance, to show the wideband response, and also to show that the negative permittivity is tunable by varying the load impedance. A mathematical model for a unit cell loaded with a non-Foster circuit having parasitic resistances is developed, and calculated, simulated, and measured results for the unit cell with a non-ideal load

are presented. Portions of this material have been published previously, in [9].

The SRR is a resonant structure first suggested by Pendry in [6] that produces a negative magnetic susceptibility over a very narrow band of frequencies above resonance. This was the negative permeability structure utilized in the first measurement of a double-negative material, presented in [11]. A detailed mathematical analysis of the structure is given in [10] and [12]. To overcome the bandwidth limitations of this structure, [8] suggests loading the resonator with a non-Foster circuit designed to nullify the intrinsic reactance of the unit cell. This chapter will present a simulated split ring resonator unit cell loaded with an ideal negative inductance, to show the wideband response, and also to show that the permeability of the unit cell is tunable by changing the load impedance. A mathematical model for a unit cell loaded with a non-Foster circuit having parasitic resistances is developed, and calculated and simulated results for the unit cell with a non-ideal load are presented.

3.1 Metamaterial Parameter Extraction Methods

In [42], a method for extracting relative permeability and permittivity from measured S-parameters is presented. This method assumes that the material under investigation (MUI) is embedded in free space having characteristic impedance 377 Ω, but is easily adjustable for various embedding materials, as long as their characteristic impedance is known. Once the S-parameters are obtained, this extraction method is as follows. First, the characteristic impedance of the MUI is obtained by:

$$\eta_s = \pm\eta_\circ \sqrt{\frac{(S_{11}+1)^2 - S_{21}^2}{(S_{11}-1)^2 - S_{21}^2}} \tag{3.1}$$

where η_0 is the characteristic impedance of free space. It is noted in [42] that the choice of the positive or negative root of η_s will change several intermediate values, but will not affect the final values of extracted permeability and permittivity. If the

positive root of η_s is chosen, the transmission term is given by:

$$e^{-jk_sd} = \frac{S_{21}(\eta_s + \eta_\circ)}{(\eta_s + \eta_\circ) - S_{11}(\eta_s - \eta_\circ)} \tag{3.2}$$

where k_s is the wavenumber in the MUI, and d is the thickness of the MUI in the direction of propagation, in meters. The wavenumber is obtained from (3.2) by:

$$k_s = \frac{j}{d}\ln(e^{-jk_sd}) \tag{3.3}$$

where 'ln' denotes the complex natural logarithm. Because of the periodic nature of the complex exponential, (3.3) does not result in a single solution for k_s. All the possible values of k_s are given by:

$$k_s = \frac{j}{d}\left[\Re e\{\ln\left(e^{-jk_sd}\right)\} + j\left(\Im m\{\ln\left(e^{-jk_sd}\right)\} + 2p\pi\right)\right] \tag{3.4}$$

where p is an integer. Note that the first term in the right hand side of (3.4) corresponds to the imaginary part of k_s, and is unambiguous. This is because, unlike phase, loss can be measured absolutely. The value of p in the second term must be zero at low frequencies ($k_sd \approx 0$), and as frequency increases p must be chosen to enforce continuity of relative permeability and permittivity over frequency. Finally, the permeability and permittivity of the MUI are given by:

$$\mu_s = \frac{k_s\eta_s}{\omega} \tag{3.5}$$

and

$$\epsilon_s = \frac{k_s}{\omega\eta_s} \tag{3.6}$$

where ω is the frequency of the wave, in radians per second. It should be noted that the relative permeability and permittivity are obtained from $\mu_r = \frac{\mu_s}{\mu_\circ}$ and $\epsilon_r = \frac{\epsilon_s}{\epsilon_\circ}$.

A second extraction method is presented in [43]. This method follows a very similar procedure, except that the material is assumed to be causal, and the Kramers-Kronig relations are used to calculate the ambiguous real part of k_s from the unambiguous imaginary part. This paper was accompanied by a published script that automated the extraction process for comma separated S-parameter data files. This script forced the imaginary parts of permeability and permittivity to be positive for passive materials. In this document, a modified version of that script is used, where the imaginary parts of permeability and permittivity are negative for passive materials.

3.2 Validation of Measurement Fixture

All the measurements presented in this chapter are made using a measurement fixture consisting of a coaxial line section with a length of 76.2 mm, an outer radius of 57.5 mm, an inner radius of 28 mm, and a characteristic impedance of approximately 52 Ω. The outer conductor is supported by a 1 mm thick pipe of ABS plastic. This coaxial line section also includes tapering sections of 77.1 mm in length on either end, transitioning from N-type connectors, but these are mathematically eliminated from the measured results using TRL calibration.

Unless otherwise noted, all extractions performed in this chapter are according to the method described in [43], modified so that negative imaginary parts indicate loss. The characteristic impedance of the embedding material was also adjusted for the measurement cases, using the measured phase of S_{21} for an empty fixture and the assumption that the permeability of the empty fixture was equal to one.

The fixture and calibration pieces were fabricated of ABS plastic using a Makerbot Replicator 2X, and copper foil was used to achieve conductivity over the surfaces of the inner and outer conductors. Detailed diagrams of the measurement fixture and its calibration pieces are presented in Appendix A.

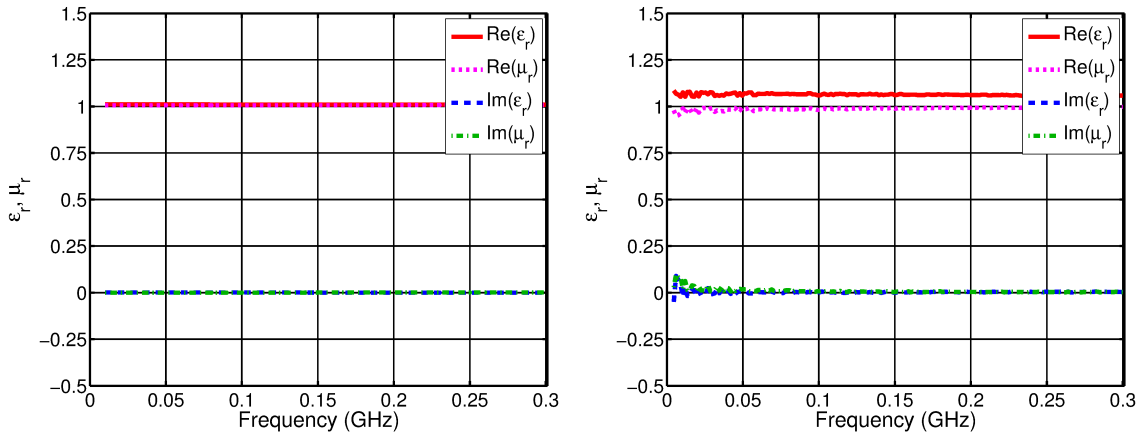

Figure 3.1: (a) Simulation results from HFSS for an empty test fixture. (b) Measured results for an empty test fixture.

3.2.1 Control Measurement 1: Empty Fixture

Since this fixture constitutes a new measurement methodology, it is appropriate to first present a few control measurements, to validate the subsequent results. The first such measurement is of the empty measurement fixture. This measurement is expected to have relative permeability equal to one, since the fixture is almost entirely empty.

The extracted relative permeability and permittivity for an HFSS simulation of the empty fixture is shown in Fig. 3.1 (a). Here, and throughout this chapter, the real and imaginary parts of permittivity and real and imaginary parts of permeability are shown in solid red, dashed blue, dotted magenta, and dash-dotted green, respectively. This simulation shows an extracted relative permittivity of $1.01 + j0.00$, and an extracted relative permeability of $1.01 + j0.00$ across the band. The extracted relative permeability and permittivity from the measurement of the empty fixture is shown in Fig. 3.1 (b). This extraction shows relative permittivity of approximately $1.06 + j0.00$ and relative permeability of approximately $0.99 + j0.00$ across the band, though there is some visible noise at the low end of the frequency spectrum. The slight difference between the simulated and extracted values of permittivity is probably due to the

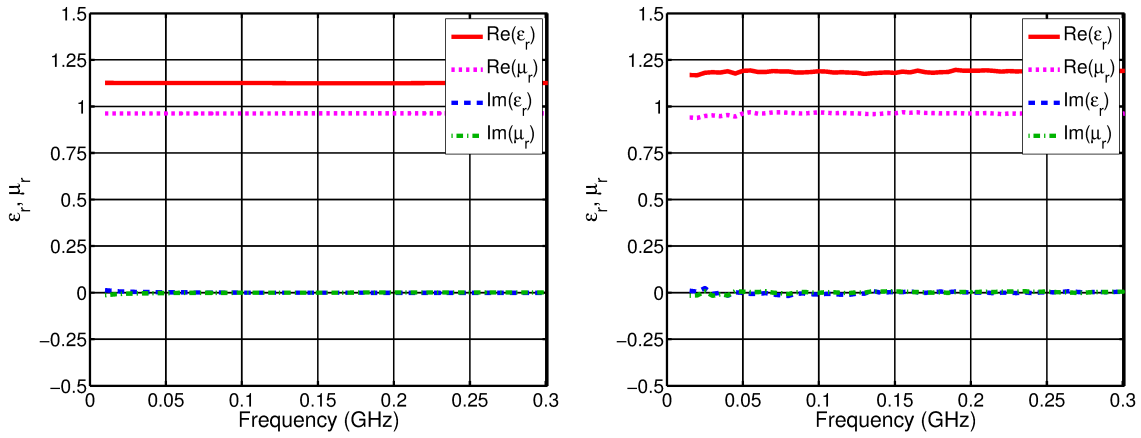

Figure 3.2: (a) Relative permeability and permittivity for the HFSS simulation of the metal rectangle on an FR-4 substrate. (b) Relative permeability and permittivity for the measurement of the metal rectangle on an FR-4 substrate.

ABS plastic of the support material having a slightly higher dielectric constant than was used in simulation.

3.2.2 Control Measurement 2: Metal Rectangle

The second control measurement is of a copper rectangle having a thickness of 0.035 mm, a length of 70 mm, and a width of 22 mm, on an FR-4 substrate with dimensions 76.2 mm × 32 mm × 0.79 mm. Figure 3.2 (a) shows the extracted values for this simulation in HFSS. As shown, the simulated relative permittivity is $1.11 + j0.00$ across the band, and the simulated relative permeability is $0.97 + j0.00$. Figure 3.2 (b) shows the extracted values for the measurement of the metal sheet. As shown, the measured relative permittivity is approximately $1.18 + j0.00$, and the measured relative permeability is approximately $0.96 + j0.00$.

3.2.3 Control Measurement 3: Passive CLS

The third control measurement is of the CLS unit cell that will be discussed in Section 3.3, having a passive load of 820 nH in series with 80.6 Ω located at the end of the extending traces. The left-hand graphs of Figure 3.3 show the parameters extracted using the method described in [43], and the right-hand graphs show the

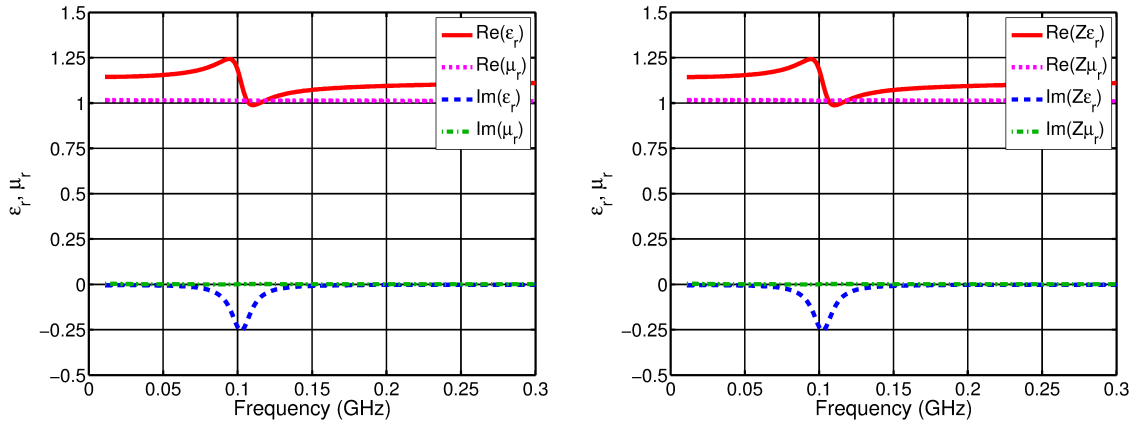

(a)

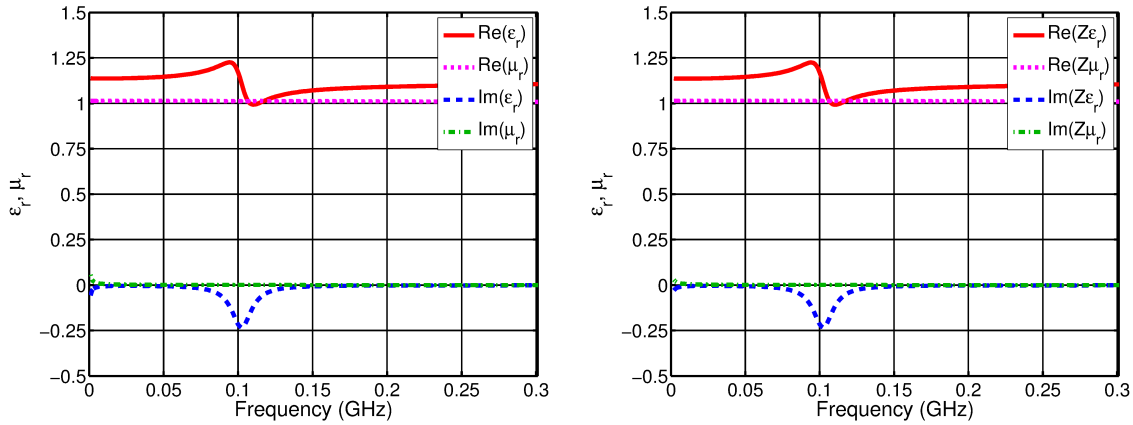

(b)

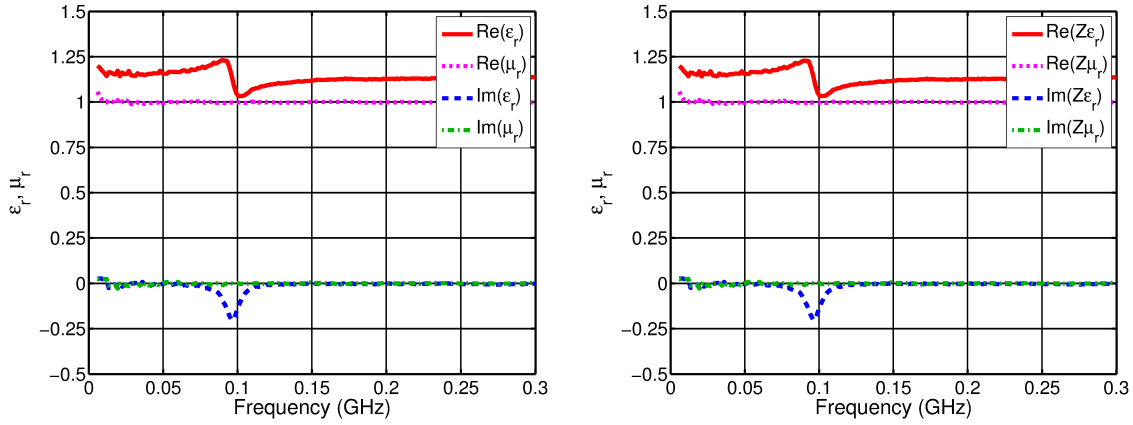

(c)

Figure 3.3: Extracted parameters for the CLS with a load of 820 nH in series with 80.6 Ω, obtained from (a) simulation in ADS, using CLS S-parameters from HFSS. (b) simulation purely in HFSS. (c) measurement in the fixture. The left-side figures are extracted using [43], and the right-side figures are extracted using [42].

parameters extracted using the method described in [42]. Figure 3.3 (a) shows the extracted values for a simulation conducted in ADS, using 4-port parameters from HFSS for the CLS. This simulation shows a small rise in the real part of permittivity, followed by a small dip. These fluctuations in the real part of permittivity are accompanied by a dip in the imaginary part of permittivity. The maximum real part of permittivity is 1.24 at 94 MHz, and the minimum is 0.99 at 110 MHz. The minimum of the imaginary part of permittivity is -0.26 at 102 MHz. The extracted value of permeability is approximately $1.01 + j0.00$ across the band.

This same structure was simulated entirely in HFSS, using lumped element RLC boundaries on two series sheets at the ends of the protruding traces. The results from this simulation, using a modified version of the extraction method presented in [43], are shown in Fig. 3.3 (b). As in the ADS simulation, the HFSS simulation shows a small rise then dip in the real part of permittivity, accompanied by a dip in the imaginary part of permittivity. The maximum value of the real part of permittivity in the HFSS simulation is 1.22 at 94 MHz, and the minimum value is 0.99 at 110 MHz. The imaginary part of permittivity has a minimum at 102 MHz of -0.23. The extracted permeability is approximately $1.01 + j0.00$ across the band. These values are almost identical to those resulting from the ADS simulation.

This structure was measured in the fixture, and Figure 3.3 (c) shows the resulting values of permeability and permittivity. As in the simulations, the real part of permittivity shows a local maximum followed by a local minimum, while the imaginary part of permittivity shows loss. The maximum measured value of permittivity is 1.22 at 90 MHz, and the minimum is 1.03 at 100 MHz. The minimum value of the imaginary part of permittivity is -0.20 at 96 MHz. The extracted permeability is approximately $0.99 + j0.00$ across the band.

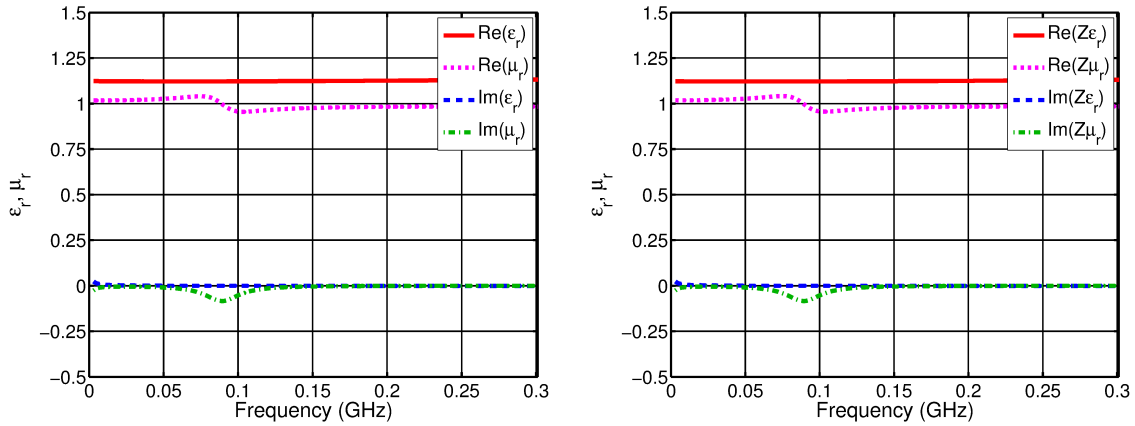

(a)

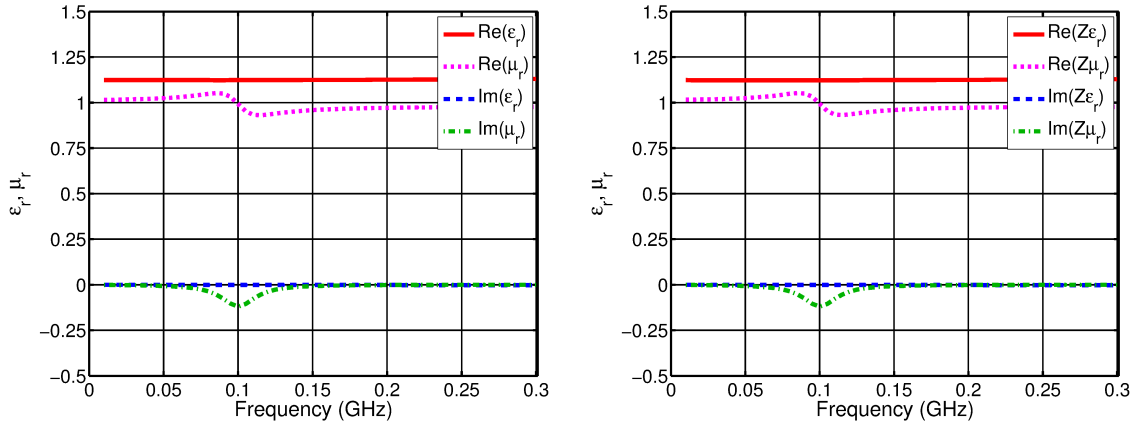

(b)

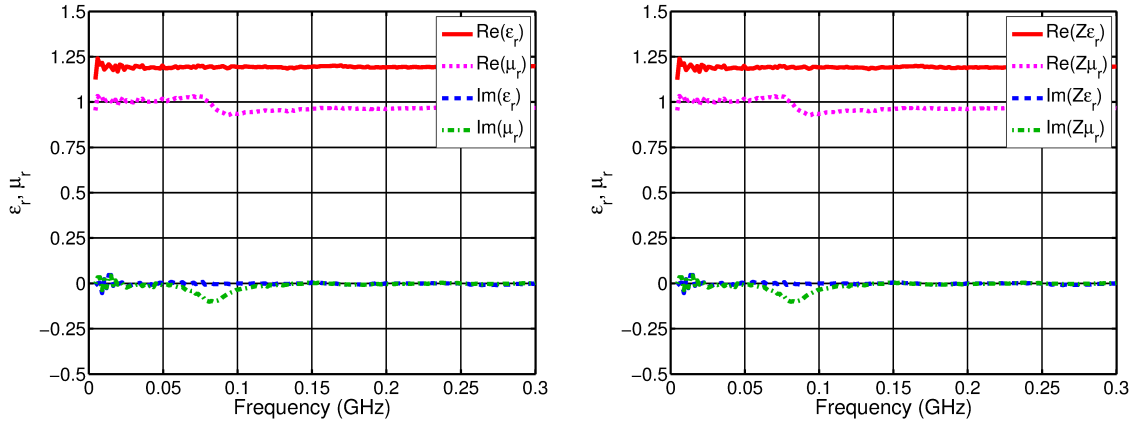

(c)

Figure 3.4: Extracted parameters for the SRR with a load of 18 pF in parallel with 301 Ω, obtained from (a) simulation in ADS, using SRR S-parameters from HFSS. (b) simulation purely in HFSS. (c) measurement in the fixture. The left-side figures are extracted using [43], and the right-side figures are extracted using [42].

3.2.4 Control Measurement 4: Passive SRR

The fourth control measurement is of the single split ring resonator that will be discussed in Section 3.6, loaded with a passive 20 pF capacitor in parallel with a 300 Ω resistor. Figure 3.4 (a) shows the extracted values for a simulation conducted in ADS, using 4-port parameters from HFSS for the ring. This simulation shows a small rise and then dip in the real part of permeability, accompanied by a dip in the imaginary part of permeability. The maximum real part of permeability is 1.04, and occurs at 74 MHz. The minimum real part of permeability is 0.95, and occurs at 104 MHz. The minimum of the imaginary part of permeability is -0.084, at 89 MHz. The permittivity is approximately $1.12 + j0.00$ across the band.

This same structure was also simulated entirely in HFSS, using a lumped RLC boundary on a sheet at the ends of the two protruding traces. The results from this simulation are shown in Fig. 3.4 (b). As in Fig. 3.4 (a), this figure shows a small rise in the real part of permeability, followed by a small dip. This behavior is accompanied by a dip in the imaginary part of permeability. The maximum value of the real part of permeability is 1.05, and occurs at 85 MHz. The minimum value of the real part of permeability is 0.93, and occurs at 115 MHz. The minimum value of the imaginary part of permeability is -0.11, and occurs at 100 MHz. The extracted permittivity is approximately $1.12 + j0.00$ across the band.

Finally, this structure was measured in the fixture. These results are shown in Fig. 3.4 (c). As in simulation, the real part of permeability demonstrates a slight rise, followed by a small dip. The imaginary part of permeability displays a dip in the same frequency region. The maximum measured value of permeability is 1.03, at 73 MHz. The minimum real part of permeability is 0.93, at 93 MHz. The minimum value of the imaginary part of permeability is -0.10, at 84 MHz. The measured permittivity is approximately $1.18 + j0.00$ across the band.

These control measurements show very good correlation between measured and

simulated results, as well as between parameters obtained through application of two different extraction techniques.

3.3 I-shaped Resonator Theory

The I-shaped metamaterial unit cell presented in this section is based on the CLS presented in [10]. The CLS is formed of copper traces with a thickness of 0.035 mm and a width of 1 mm on a 76.2 mm × 32 mm × 0.79 mm FR-4 substrate. The length of the metal arms of the CLS is 70 mm, and the separation between the arms is 20 mm, as shown in Fig. 3.5. The CLS also has two traces that extend away from the structure itself, to provide support for an external circuit, such as a non-Foster or other load.

A CLS unit cell may be modeled as a very small electric dipole with capacitance C_d and length ℓ_d loaded with inductance L_d, in an effective volume V_d, with narrowband negative electric susceptibility given by:

$$\chi_e = \frac{\ell_d^2 / (\epsilon_\circ V_d)}{s\left(sL_d + 1/(sC_d)\right)} = \frac{(C_d \ell_d^2) / (\epsilon_\circ V_d)}{1 + s^2 L_d C_d} , \tag{3.7}$$

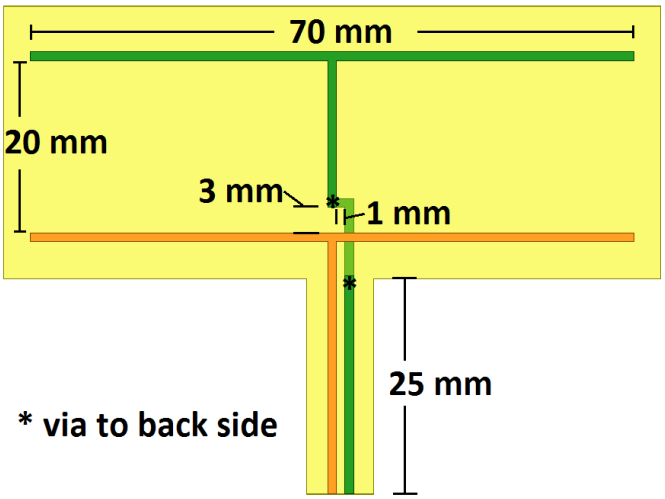

Figure 3.5: The dimensions of the CLS unit cell on a 1/32 slab of FR-4. All traces have a width of 1 mm.

where s is the Laplace $s = j\omega$ and $\epsilon_\circ = 8.85 \times 10^{-12}$ F/m is the permittivity of free space [10]. By replacing the inductive post in the CLS with capacitance C_p having both a series parasitic resistance R_s and a parallel parasitic resistance R_p, as shown in Fig. 3.6, the result of (3.7) becomes

$$\chi_e = \frac{\ell_d^2 C_d \left(s \left(R_s + R_p\right) C_p + 1\right) / \left(\epsilon_\circ V_d\right)}{s^2 R_s R_p C_d C_p + s \left(R_p (C_p + C_d) + R_s C_p\right) + 1} \,. \tag{3.8}$$

For $R_p = \infty$ and $R_s = 0$ the result in (3.8) becomes independent of frequency at low frequencies and can be approximated as

$$\chi_e \approx \frac{\ell_d^2}{\epsilon_\circ V_d} \, \frac{C_p C_d}{C_p + C_d} \,, \tag{3.9}$$

where (3.9) has the same wideband form as the result in [8] for a similar unit cell. Note that χ_e can become a relatively large negative value when $C_p < 0$, $C_p + C_d > 0$, and $|C_p + C_d| << |C_d C_p|$.

As demonstrated in (3.8) and (3.9), the theoretical effective electric susceptibility χ_e and effective relative permittivity $\epsilon_r = 1 + \chi_e$ of the non-Foster loaded CLS unit cell is bandlimited by the parasitic resistances R_p and R_s that lead to the quadratic in

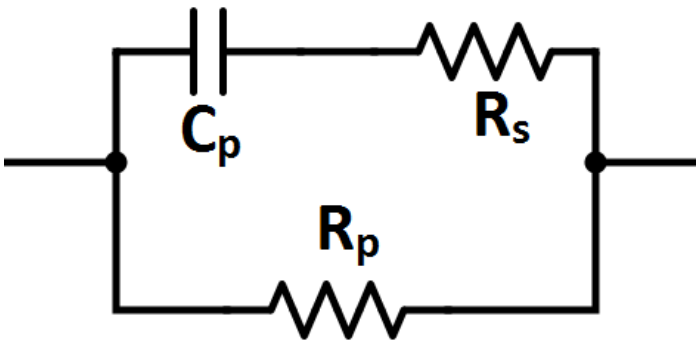

Figure 3.6: The non-Foster capacitance with parasitic series and parallel resistance.

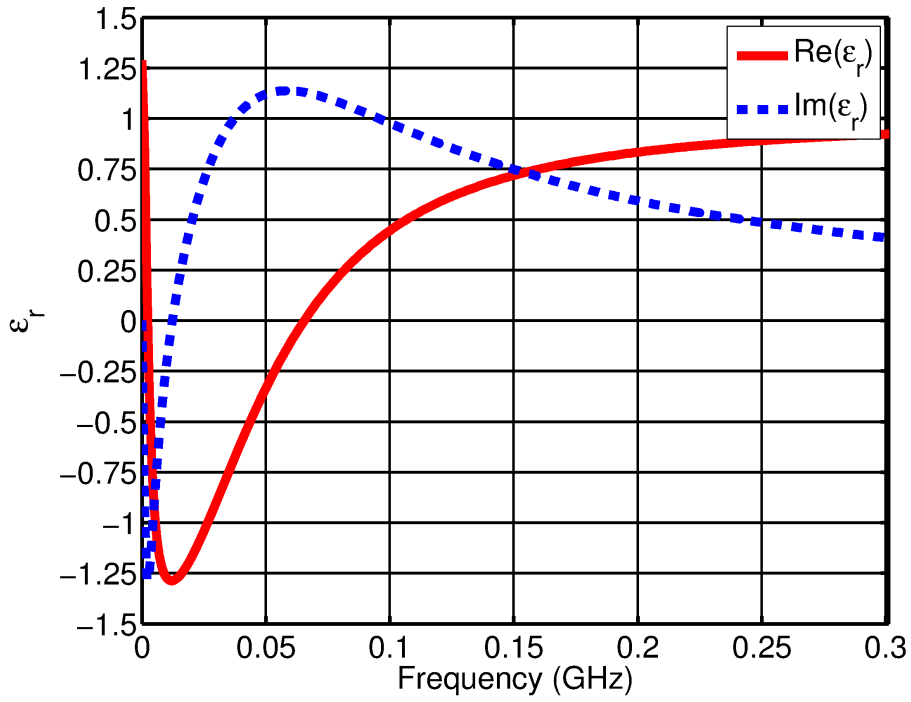

Figure 3.7: Theoretical relative permittivity for the case where $R_s = -133\ \Omega$, $R_p = 220\ \text{k}\Omega$, $C_d = 2.7$ pF, $C_p = -2.4$ pF, $l_d = 0.02$ m, and $V_d = 4.24 \times 10^{-4}$ m^3.

the denominator of (3.8). The real and imaginary parts of $\epsilon_r = 1 + \chi_e$ calculated from (3.8) for the case where $R_s = -133\ \Omega$, $R_p = 220\ \text{k}\Omega$, $C_d = 2.7$ pF, $C_p = -2.4$ pF, $l_d = 0.02$ m, and $V_d = 4.24 \times 10^{-4}$ m^3 are shown in Fig. 3.7. The real part of ϵ_r is shown to be sub-unity over a band from 2 MHz to approximately 300 MHz, a bandwidth of 196%. The minimum value of permittivity occurs at 12 MHz, where $\epsilon_r = -1.288 - j0.0219$. Loss, indicated by the negative imaginary part of ϵ_r, is observed from approximately 0 MHz to 12 MHz. Gain, indicated by the positive imaginary part of ϵ_r, is observed from approximately 12 MHz to 300 MHz. This is understandable, given that the parallel parasitic resistance, which dominates at low frequencies, is positive and absorbs power, while the series parasitic resistance, which is negative, dominates at high frequencies and injects power (see Fig. 3.6).

For contrast, Fig. 3.8 shows the real and imaginary parts of ϵ_r calculated from (3.8) for the case where $R_s = 0\ \Omega$, $R_p = 220\ \text{G}\Omega$, $C_d = 2.7$ pF, $C_p = -2.4$ pF, $l_d = 0.02$ m, and $V_d = 4.24 \times 10^{-4}$ m^3. As shown, this eliminates the effects of the

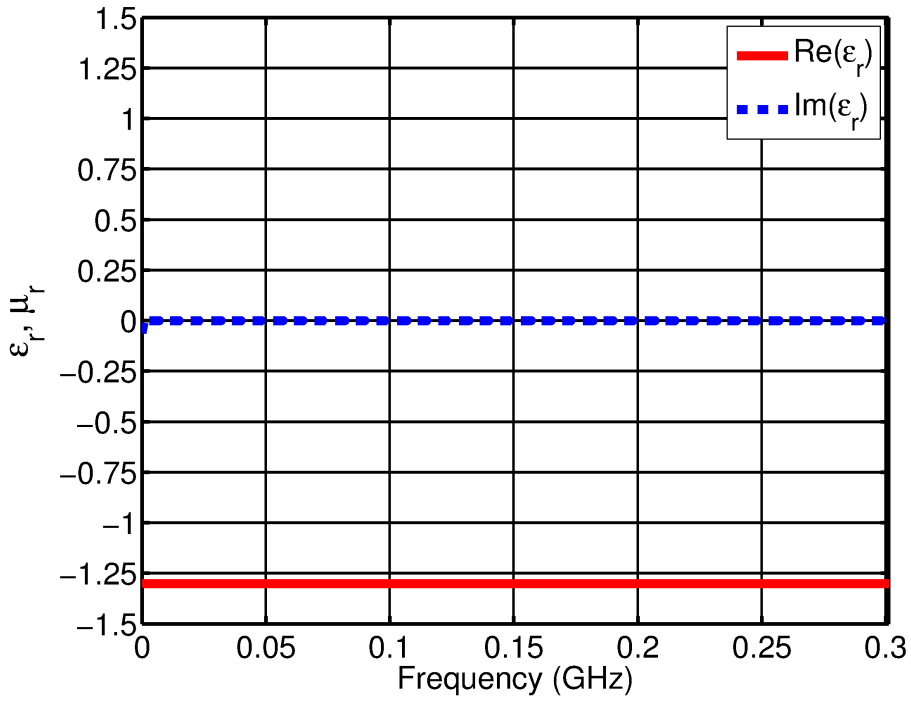

Figure 3.8: Theoretical relative permittivity for the case where $R_s = 0\ \Omega$, $R_p = 220\ \text{G}\Omega$, $C_d = 2.7$ pF, $C_p = -2.4$ pF, $l_d = 0.02$ m, and $V_d = 4.24 \times 10^{-4}$ m^3.

parasitics (except at very low frequencies, where the impedance of C_p begins to have the same scale as R_p), and results in wideband negative permittivity. Across the entire band of interest, the permittivity is given by $\epsilon_r \approx -1.300 + j0.00$. It must be noted that this calculation assumes that in the presence of non-Foster loading the intrinsic impedance of the CLS can be perfectly modeled as a single capacitor, which, while a good approximation at low frequencies, is not entirely accurate.

3.4 Simulation of I-shaped Resonator

The CLS unit cell was first simulated in a parallel plate waveguide, using Ansys HFSS software. Figure 3.9 shows the simulation configuration. The waveguide is formed of a box with a width of 165.3 mm and a height of 33.7 mm. The two sides normal to $\vec{z}$ were defined as PEC; the two sides normal to $\vec{y}$ were defined as PMC, and the two sides normal to $\vec{x}$ were defined as waveports. The two lines extending from the main body of the CLS protruded from the top side of the waveguide into a

vacuum box with radiation boundaries, and an ideal non-Foster negative capacitance was positioned at their end, with the current line defined from one trace to the other.

Figure 3.10 (a) shows the extracted values of permeability and permittivity for the CLS unit cell with an ideal lumped capacitor load of -2.8 pF. As shown, this results in a high dielectric constant ($\sim$3) at low frequencies. From (3.9), this corresponds to expected behavior for values of $|C_p|$ slightly larger than C_d. This simulation also exhibits negative permittivity from 155 MHz to 220 MHz. The minimum value of ϵ_r is $-1.654 - j2.535$ at 170 MHz. Figure 3.10 (b) shows the result for an ideal lumped capacitor load of -2.7 pF. This simulation shows negative ϵ_r from 10 MHz to 170 MHz, and sub-unity permittivity across the range of the simulation. From 10 MHz to 120 MHz, the real part of ϵ_r is approximately flat, with an average value of approximately -1.25, which topologically matches the behavior shown in Fig. 3.8. This indicates that the intrinsic capacitance C_d of this CLS is most likely approximately equal but slightly greater than 2.7 pF. Figure 3.10 (c) shows the extracted values for an ideal lumped capacitor load of -2.5 pF. This graph shows ϵ_r sub-unity across the simulated band, from 10 MHz to 300 MHz, but never negative. The minimum value of ϵ_r exhibited by this simulation is $0.5859 - j0.0647$ at 50 MHz. Comparison of this graph with (3.9) leads to the conclusion that, in this case, $C_p + C_d$ is a positive value

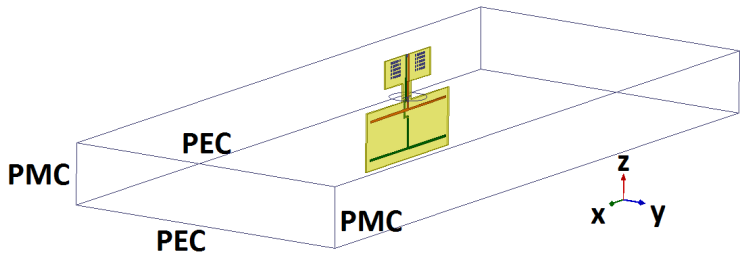

Figure 3.9: HFSS model of a CLS unit cell in a parallel plate waveguide.

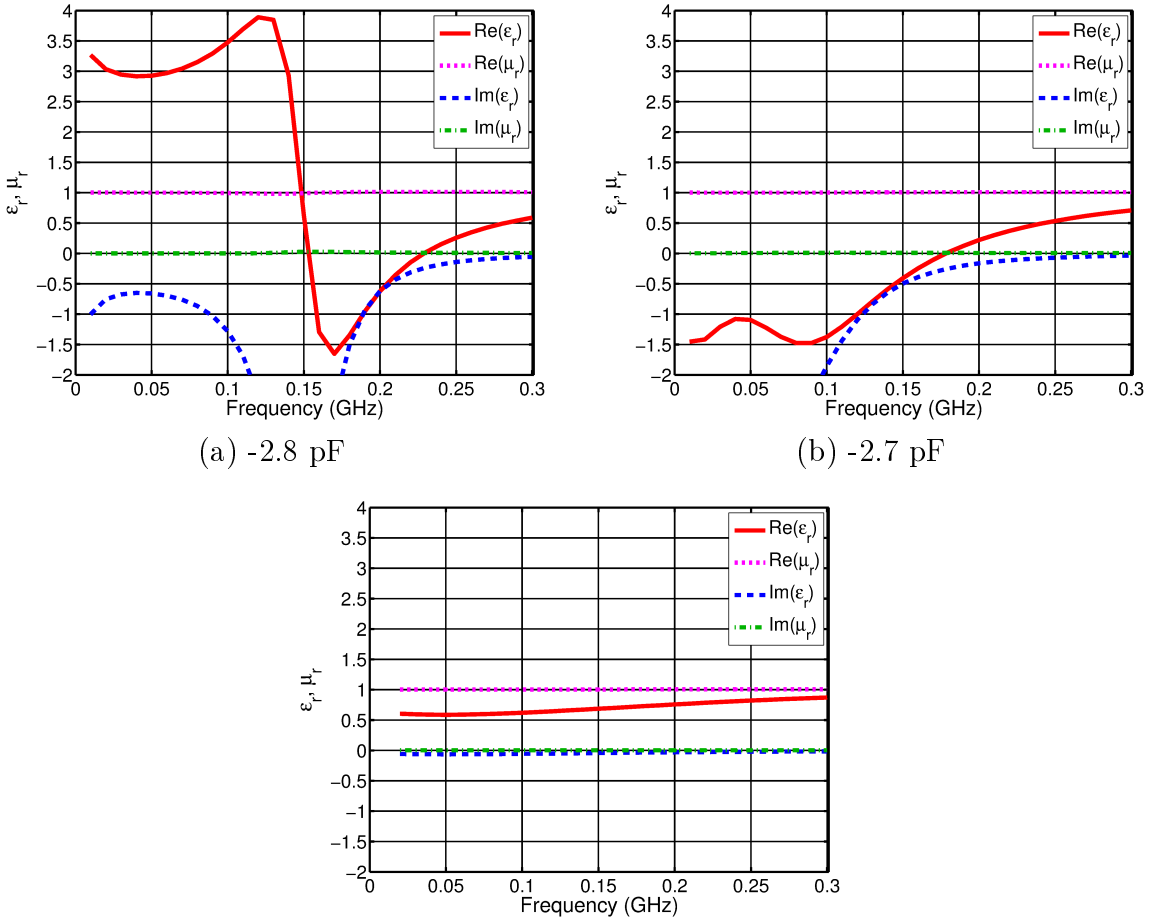

(a) -2.8 pF

(b) -2.7 pF

(c) -2.5 pF

Figure 3.10: HFSS simulation results for the CLS in a parallel plate waveguide loaded with (a) an ideal -2.8 pF capacitor. (b) an ideal -2.7 pF capacitor. (c) an ideal -2.5 pF capacitor.

only slightly smaller than $|C_p C_d|$, which results in a small negative value of χ_e, and thus to a weak response. These three simulations show that the value of ϵ_r can be tuned by changing the value of the non-Foster loading capacitance.

Next, the CLS was simulated in the same parallel plate waveguide with non-ideal non-Foster loading. The value of R_s is set to $-133\ \Omega$, and the value of R_p is set to 220 kΩ. Figure 3.11 (a) shows the extracted permeability and permittivity for a load capacitance of -2.5 pF. The low-frequency dielectric constant of ~ 2.5 indicates that the value of $C_p + C_d$ is negative. Figure 3.11 (b) shows the extracted results for a load capacitance of -2.4 pF. As shown, the real part of permittivity is sub-unity

from 5 MHz to 38 MHz, corresponding to a bandwidth of 153%. The minimum value of ϵ_r is $-1.784 + j0.5646$, at 18 MHz. As predicted, loss is observed at low frequencies, from 5 MHz to 18 MHz, and gain is observed at higher frequencies, from 18 MHz to 300 MHz. Figure 3.11 (c) shows the extracted results for a load capacitance of -2.3 pF. This simulation exhibits sub-unity permittivity from 5 MHz to 70 MHz, which is a bandwidth of 173%. It is interesting to note that, though weaker, this is a wider reponse than is seen in Fig. 3.11 (b). The minimum value of ϵ_r is $0.3280 + j0.08655$, at 20 MHz. Loss is observed from 10 MHz to 18 MHz, and gain is

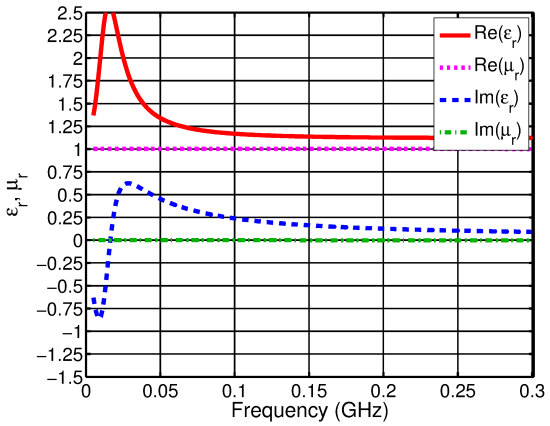

(a) -2.5 pF

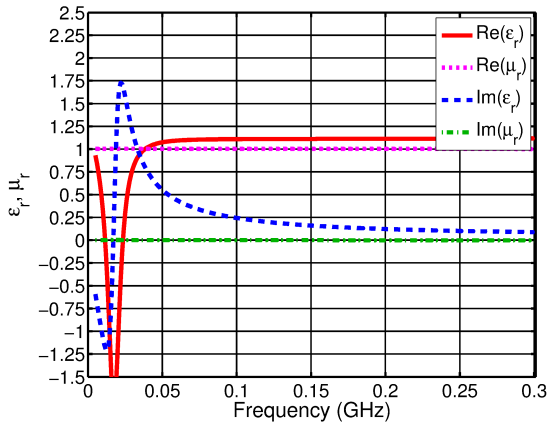

(b) -2.4 pF

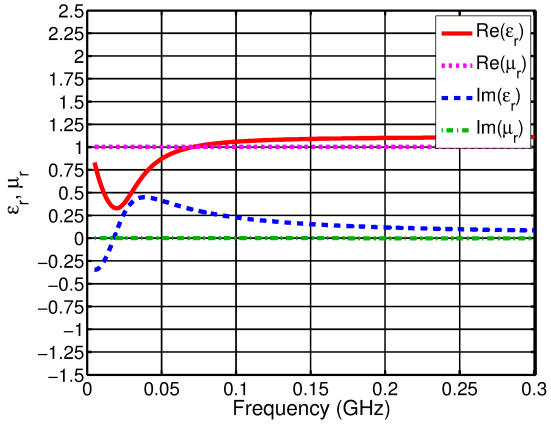

(c) -2.3 pF

Figure 3.11: HFSS simulation results for the CLS in a parallel plate waveguide, loaded with (a) a non-ideal -2.5 pF load, where $R_s = -133\ \Omega$ and $R_p = 220\ \text{k}\Omega$. (b) a non-ideal -2.4 pF load, where $R_s = -133\ \Omega$ and $R_p = 220\ \text{k}\Omega$. (c) a non-ideal -2.3 pF load, where $R_s = -133\ \Omega$ and $R_p = 220\ \text{k}\Omega$.

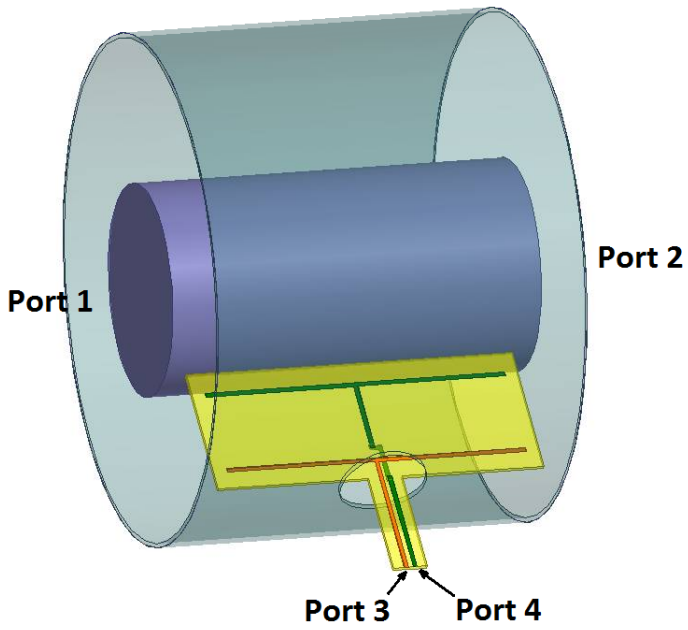

Figure 3.12: The CLS unit cell in a coaxial line section.

observed from 18 MHz to 300 MHz. Comparing the results of Fig. 3.11 to the results of Fig. 3.10, the band-limiting property of the added parasitic resistance is clearly demonstrated. It is also interesting to note that the addition of parasitic resistance shifted the value of negative capacitance needed to achieve the optimal result from ~ -2.7 pF to ~ -2.4 pF. Up to this point in the discussion, all simulations and calculations have been conducted using a parallel plate waveguide. However, the structure was measured in the 3D printed coaxial fixture discussed in Section 3.2. The differences between parallel plate and coaxial test environments are expounded upon in detail in Chapter 4. Two traces, with a 1 mm separation, protruded through a hole in the coax shield, providing access to the metamaterial from outside, as shown in Fig. 3.12.

A structure having this geometry was simulated in HFSS, using non-ideal loading with $R_s = -133\ \Omega$ and $R_p = 220\ \text{k}\Omega$. The resulting extracted permeability and permittivity are shown in Fig. 3.13. Figure 3.13 (a) shows the extracted values for a load capacitance of -2.4 pF. The low-frequency dielectric constant of $\sim$2.2 indicates

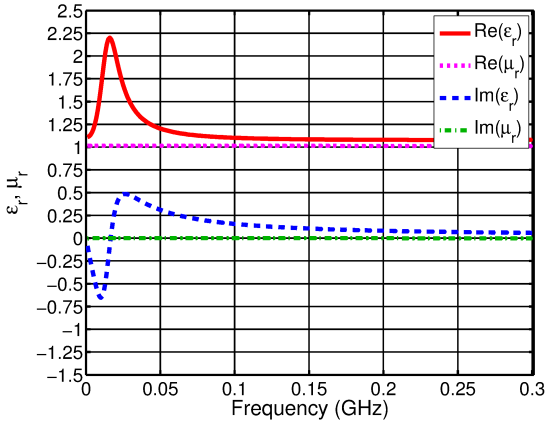

(a) -2.4 pF

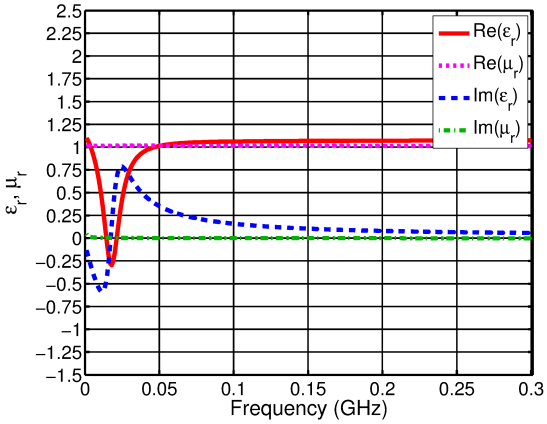

(b) -2.3 pF

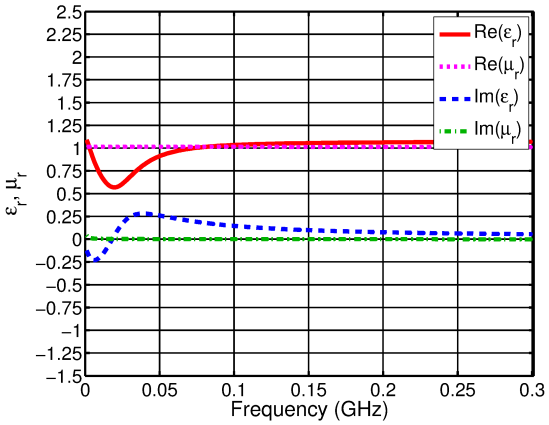

(c) -2.2 pF

Figure 3.13: HFSS simulation results for the CLS in a coaxial waveguide, loaded with (a) a non-ideal -2.4 pF load, where $R_s = -133\ \Omega$ and $R_p = 220\ \text{k}\Omega$. (b) a non-ideal -2.3 pF load, where $R_s = -133\ \Omega$ and $R_p = 220\ \text{k}\Omega$. (c) a non-ideal -2.2 pF load, where $R_s = -133\ \Omega$ and $R_p = 220\ \text{k}\Omega$.

that in this case $|C_p|$ is greater than C_d. Figure 3.13 (b) shows the extracted values for a load capacitance of -2.3 pF. This simulation shows sub-unity ϵ_r over a range of 4 MHz to 46 MHz, a bandwidth of 168%. The minimum value of ϵ_r occurs at 18 MHz, where $\epsilon_r = -0.2973 + j0.151$. Loss is observed from 1 MHz to 18 MHz, and gain is observed from 18 MHz to 300 MHz. Figure 3.13 (c) shows the extracted values for a load capacitance of -2.2 pF. Sub-unity ϵ_r is shown from 3 MHz to 73 MHz, a bandwidth of 184%, with a minimum of $\epsilon_r = 0.5685 + j0.0496$ at 20 MHz. Loss is observed from 1 MHz to 18 MHz, and gain is observed from 18 MHz to 300 MHz.

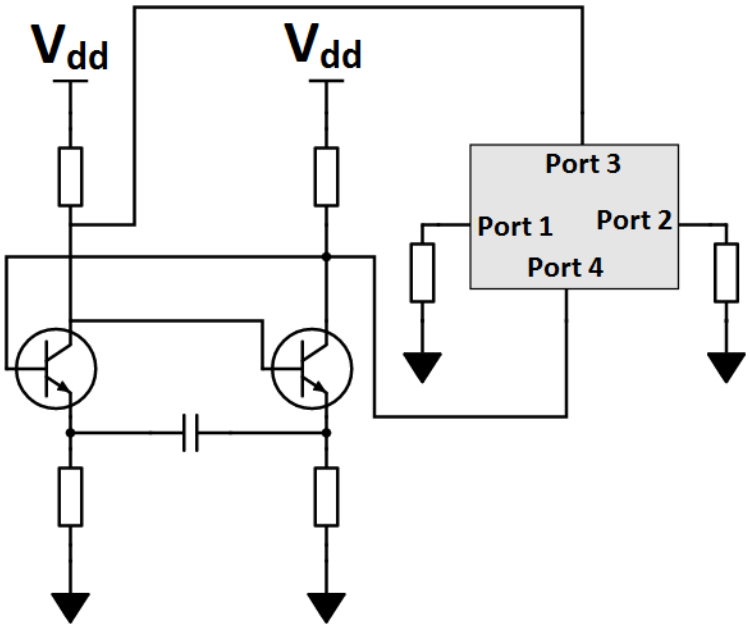

Figure 3.14: Schematic for Linvill negative capacitance circuit [23] with four-port parameters from HFSS

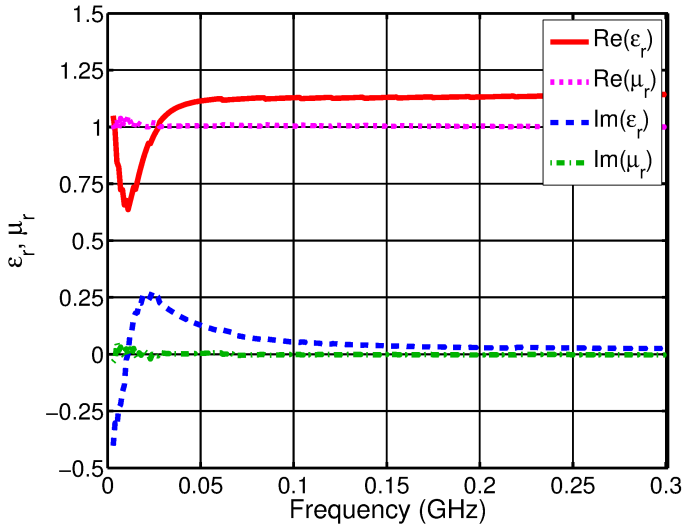

Figure 3.15: Transistor-level simulation results from Keysight ADS, using the Linvill circuit of Fig. 3.14.

A Linvill negative capacitor, shown in Fig. 3.14, was designed and simulated in the Keysight ADS simulator, and is shown in simulation to have the $R_s = -133\ \Omega$ $R_p = 220\ \text{k}\Omega$, and $C_p = 2.4$ pF [23].

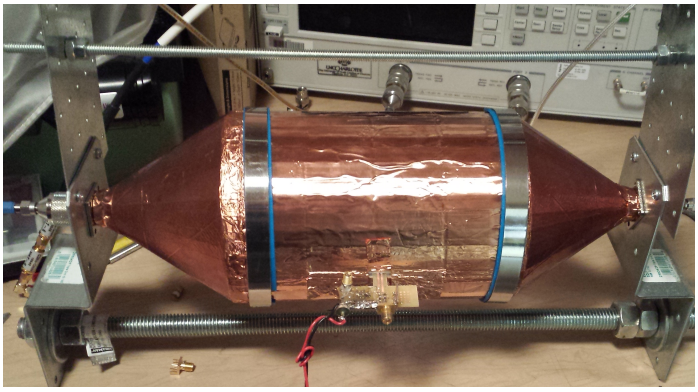

Figure 3.16: Measurement fixture with non-Foster circuit protruding from the slot

The unit cell without non-Foster loading in the coaxial line section was simulated once more in Ansys HFSS, this time with lumped ports defined at either end of the coaxial line, and also at the ends of each of the two traces that protruded through the coax shield, as shown in Fig. 3.12.

The four-port parameters from the HFSS simulation were imported into ADS, and the negative capacitor is connected between ports 3 and 4, as shown in Fig. 3.14. The resulting S-parameters between ports 1 and 2 were used with the extraction method presented in [42] to obtain the effective permeability and permittivity values of the unit cell. These simulation results are shown in Fig. 3.15. In this figure, the real part of permittivity is sub-unity from 5 MHz to 33 MHz. The minimum value of permittivity is observed at 14 MHz, where $\epsilon_r = 0.412 - j0.012$. Loss is observed from 5 MHz to 14 MHz, and gain is observed from 14 MHz to 300 MHz.

3.5 Measurement of I-shaped Resonator

The CLS unit cell was milled out on 1/64" FR-4 epoxy, and the non-Foster circuit of Fig. 3.14 was built at the end of it, using a variable capacitor to enable tuning of the non-Foster load during measurement. Figure 3.16 shows the finished measurement fixture, with the non-Foster circuit protruding from the slot, and Fig. 3.17 shows the milled out CLS, with the non-Foster circuit. The measured permittivity and permeability of the unit cell are presented in Fig. 3.18 (a), using the same color

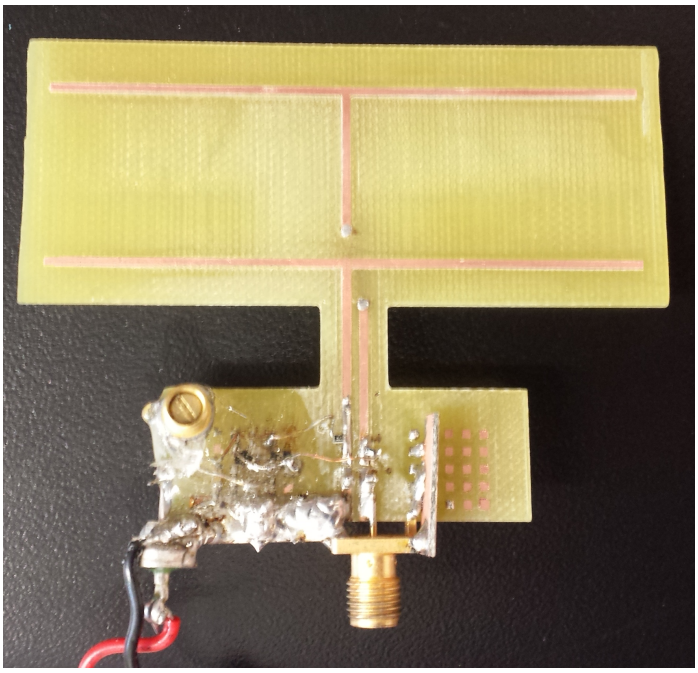

Figure 3.17: Milled CLS on FR-4, and non-Foster circuit

scheme as presented previously. This extraction was performed using the method described in [43], modified as noted earlier. Measured permittivity is shown to be sub-unity from 5 MHz to 25 MHz, corresponding to a 5:1 bandwidth, or 133%. The minimum value of permittivity occurs at 13.5 MHz, where $\epsilon_r = 0.533 - j0.019$. Loss is observed from 15 MHz to 18 MHz, and gain is observed from 18 MHz to 135 MHz. These measured results of show remarkable agreement with the simulation results of Fig. 3.15. Both Fig. 3.15 and Fig. 3.18 (a) also compare well, in both bandwidth and topological behavior over frequency, to the theoretical results of Fig. 3.7, although there appears to be an offset bias in measured dielectric constant relative to theory. The elevated high-frequency dielectric constant of $\sim$1.25 in Fig. 3.15 and Fig. 3.18 (a), is most likely due to FR-4 and ABS loading effects not included in the theoretical results of Fig. 3.7.

To demonstrate the tunability of the permittivity, Fig. 3.18 (b) shows the effect of a slight decrease in the magnitude of the negative capacitor. This figure shows the real part of permittivity to be sub-unity from 10 MHz to 41 MHz, with a minimum

permittivity of $\epsilon_r = 0.925 + j0.046$ at 19.5 MHz. Loss is shown from 1.5 MHz to 16.5 MHz, and gain is shown from 16.5 MHz to 141 MHz. It would not have been practical to disassemble the unit to measure the impedance of the negative capacitor directly, but it can be qualitatively observed from Fig. 3.18 (b) that decreasing the magnitude of the negative capacitance decreases the negativity of ϵ_r, as predicted by (3.8). Similarly, Fig. 3.18 (c) shows the effect of a slight increase in the magnitude of the negative capacitor. This graph shows sub-unity permittivity from 7.5 MHz to 19.5 MHz, with a minimum permittivity of $\epsilon_r = 0.062 + j0.069$, at a frequency of 12 MHz. Loss is observed from 1.5 MHz to 12 MHz, and gain is observed from 12 MHz to 120 MHz. Again, it can be qualitatively observed that, as predicted by (3.8), increasing the magnitude of the negative capacitance increases the negativity of ϵ_r.

This constitutes the first measurement of a non-Foster loaded wideband negative permittivity structure where the metamaterial is not electrically connected to the test fixture, emulating the free space condition. The fact that the measured response of the single unit cell is sub-unity, rather than actually negative, is likely due to averaging of the local negative response of the CLS over the entire volume of the length of coax in which it resides. This phenomenon is demonstrated in a general sense in Chapter 4, Fig. 4.18. For a more specific demonstration, five CLS unit cells were placed in the same length of coax, at intervals of 72° around the x-axis, as shown in Fig. 3.19. Each unit cell was loaded with -2.2 pF, having series resistance of $-133\ \Omega$ and parallel resistance 220 kΩ. This is the same loading that was used to produce the results in Fig. 3.13 (c), where the coax contained only a single CLS unit cell. Figure 3.20 shows the extracted values of permeability and permittivity for the case with five CLS unit cells. This figure shows a minimum value of permittivity at 20 MHz, just as in Fig. 3.13 (c), but this time the minimum value is $\epsilon_r = -1.166 + j0.263$, rather than $\epsilon_r = 0.5685 + j0.0496$. The permittivity in this simulation is negative from 7 MHz to

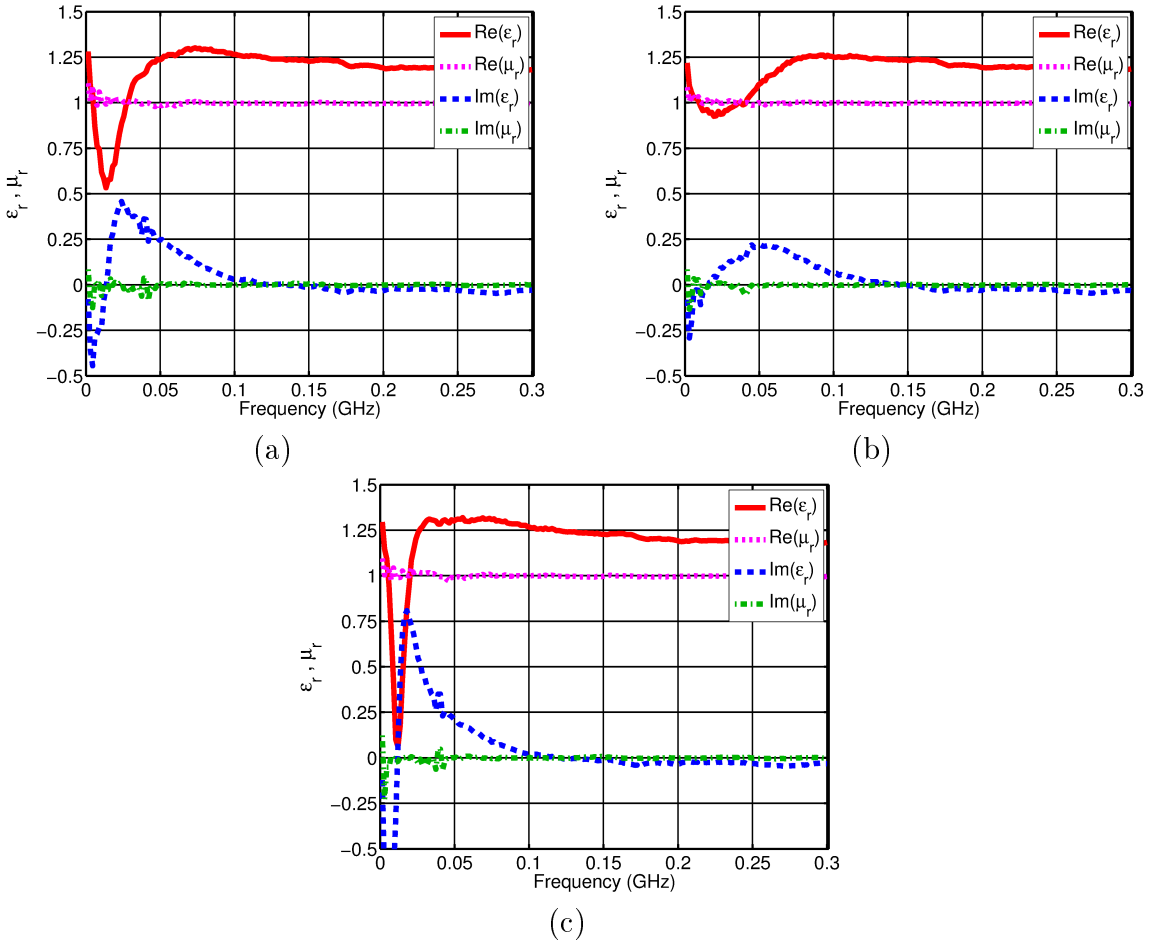

Figure 3.18: (a) Measured results for a prototype showing extracted results for the non-Foster loaded unit cell of Fig. 3.12. (b) Extracted results for measurement of the CLS loaded with slightly less negative capacitance than in (a). (c) Extracted results for measurement of the CLS loaded with slightly more negative capacitance than in (a).

39 MHz, a bandwidth of 139%.

Many of the applications of negative permittivity metamaterials require that they be paired with negative permeability structures to produce a composite double-negative medium. Therefore, the next section in this chapter will focus on developing a wideband negative permeability structure to compliment the measured negative permittivity CLS.

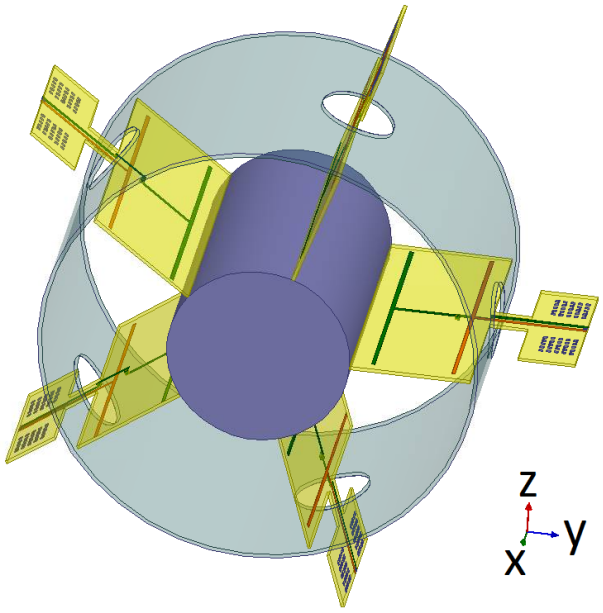

Figure 3.19: Five CLS unit cells, each loaded with -2.2 pF having series resistance of $-133\ \Omega$ and parallel resistance 220 kΩ, arranged around the x-axis at intervals of 72°.

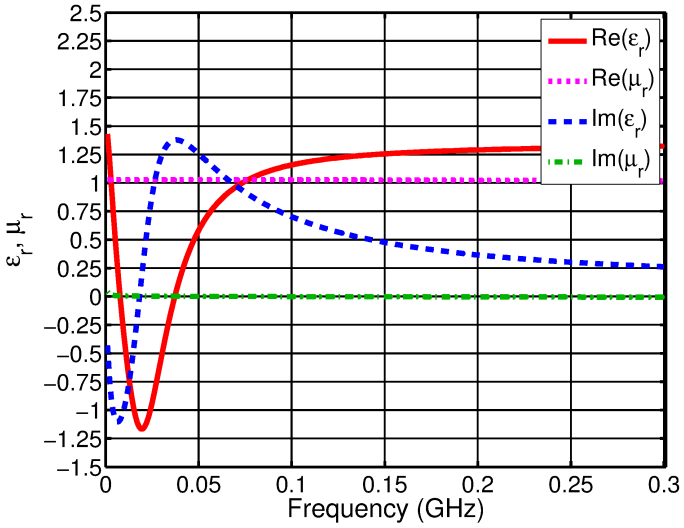

Figure 3.20: Extracted permeability and permittivity for case of five CLS unit cells, each loaded with -2.2 pF having series resistance of $-133\ \Omega$ and parallel resistance 220 kΩ.

3.6 Split Ring Resonator Theory

The rectangular ring unit cell presented in this section is based on the SRR presented in [6]. The SRR is formed of copper traces with a thickness of 0.035 mm and

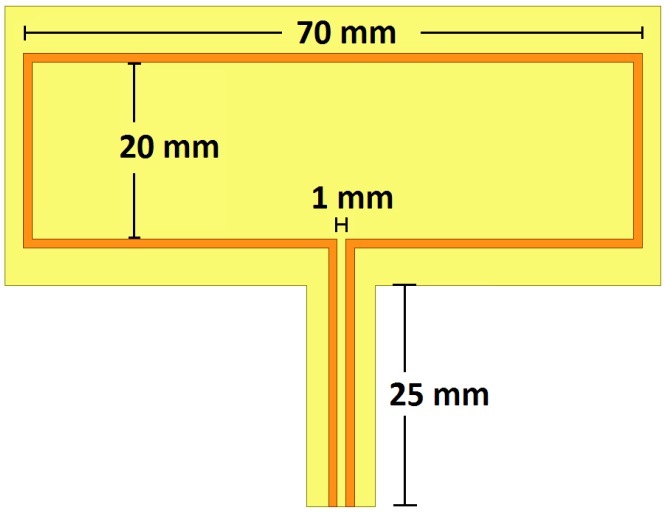

Figure 3.21: The dimensions of the SRR unit cell. All traces have a width of 1 mm.

a width of 1 mm on a 76.2 mm × 32 mm × 0.79 mm FR-4 substrate. The length of the rectangular ring is 70 mm, and the inside width is 20 mm, as shown in Fig. 3.21. The SRR has a gap of 1 mm, and two traces that extend from that gap, to provide support for non-local loading.

In the absence of non-Foster loading, an SRR unit cell may be modeled as a electrically small loop with area A_r, inductance L_r, effective volume V_r, and gap capacitance C_r. The narrowband magnetic susceptibility of the SRR is given by:

$$\chi_m = \frac{-s(\mu_0 A_r^2/V_r)}{sL_r + (1/sC_r)} \tag{3.10}$$

as shown in [10].

By replacing the capacitive gap in the SRR with inductance L_p, having both a series parasitic resistance R_s and a parallel parasitic resistance R_p, as shown in Fig. 3.22, the result of (3.10) becomes:

$$\chi_m = \frac{-(\mu_0 A_r^2/V_r)\,(s^2 L_p + s(R_p + R_s))}{s^2 L_p L_r + s(R_p(L_p + L_r) + L_r R_s) + R_p R_s} \tag{3.11}$$

For $R_s = 0$ and $R_p = \infty$, this result becomes independent of frequency at low

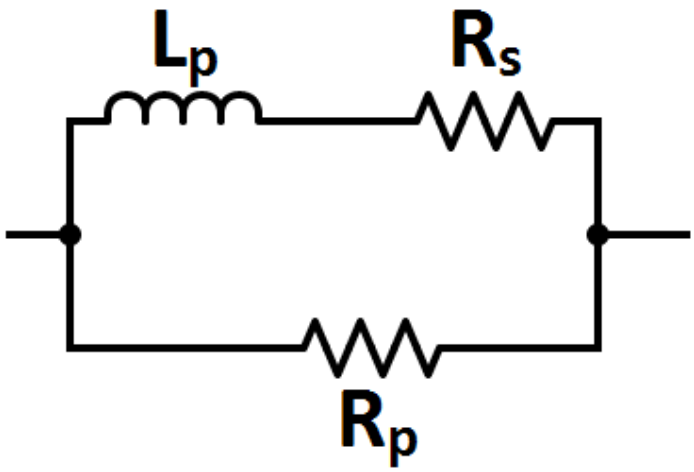

Figure 3.22: The non-Foster inductance with parasitic series and parallel resistance.

frequency, and can be approximated as:

$$\chi_m \sim -\frac{\mu_0 A_r^2}{V_r}\frac{1}{L_p + L_r} \tag{3.12}$$

where (3.12) has the same wideband form as that noted in [8] for a similar unit cell. Note that χ_m can become a relatively large negative value when $L_p + L_r << 1$. Thus the theoretical effective magnetic susceptibility χ_m and effective relative permeability $\mu_r = 1 + \chi_e$ of the non-Foster loaded CLS unit cell is bandlimited by the parasitic resistances R_p and R_s that lead to the quadratic in the denominator of (3.11).

The real and imaginary parts of $\mu_r = 1+\chi_e$ calculated from (3.11) for the case where $R_s = -0.5\ \Omega$, $R_p = 2\ \text{k}\Omega$, $L_r = 128$ nH, $L_p = -125$ nH, $A = 0.0014\ \text{m}^2$, and $V_r = 4.24\times10^{-4}\ \text{m}^3$ are plotted in Fig. 3.23. The real part of μ_r is shown to be negative over a band from 21 MHz to 76 MHz, which is a bandwidth of 113%. The minimum value of permeability occurs at 40 MHz, where $\mu_r = -0.8445 + j0.0158$. Gain is observed from 0 MHz to 40 MHz, and loss is observed from 40 MHz to 300 MHz. This is to be expected, since the series parasitic resistance, which is negative, dominates at low frequencies and injects power, while the parallel parasitic resistance, which is positive, dominates at high frequencies and absorbs power (see Fig. 3.22).

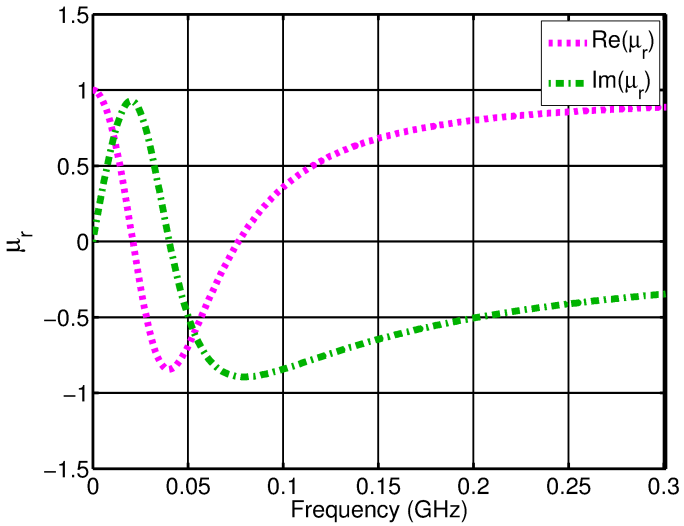

Figure 3.23: Theoretical relative permittivity for the case where $R_s = -0.5\ \Omega$, $R_p = 2\ \text{k}\Omega$, $L_r = 128$ nH, $L_p = -125$ nH, $A_r = 0.0014\ \text{m}^2$, and $V_r = 4.24 \times 10^{-4}\ \text{m}^3$.

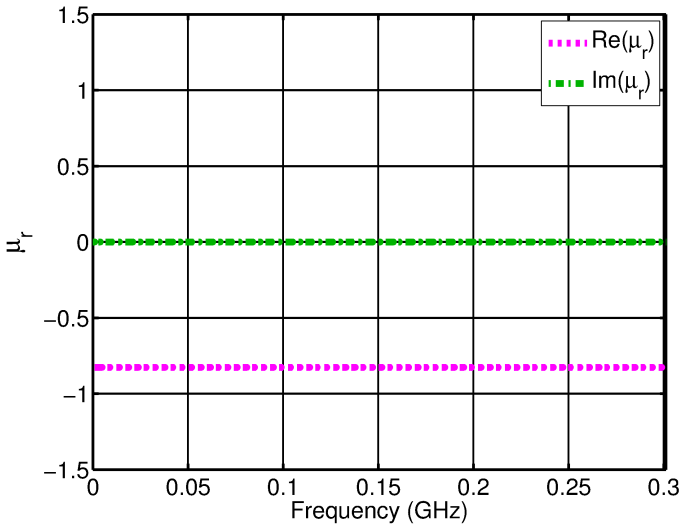

Figure 3.24: Theoretical relative permittivity for the case where $R_s = 0\ \Omega$, $R_p = 10^9\ \Omega$, $L_r = 128$ nH, $L_p = -125$ nH, $A = 0.0014\ \text{m}^2$, and $V_r = 4.24 \times 10^{-4}\ \text{m}^3$.

For contrast, Fig. 3.24 shows the calculated real and imaginary parts of μ_r for the case where $R_s = 0\ \Omega$, $R_p = 10^9\ \Omega$, $L_r = 128$ nH, $L_p = -125$ nH, $A_r = 0.0014\ \text{mF}^2$, and $V_r = 4.24 \times 10^{-4}\ \text{m}^3$. This approximates the case of (3.12). In this case, the bandwidth is not limited by the parasitic resistances, and across the entire band the permeability is given by $\mu_r = -0.8252 + j0.00$. It must be noted that this calculation

assumes that all the capacitance across the gap in the SRR is eliminated by insertion of the non-Foster element. In reality, it is likely that a non-trivial amount of fringing capacitance persists, and will become active at high frequencies, limiting the band of performance.

3.7 Simulation of Split Ring Resonator

The SRR unit cell was first simulated in a parallel plate waveguide, using Ansys HFSS software. Figure 3.25 shows the simulation configuration. The waveguide was formed of a box with a width of 163.3 mm and a height of 33.7 mm. The two lines extending from the main body of the SRR protruded from the top side of the waveguide into a vacuum box with radiation boundaries, and an ideal non-Foster negative inductance was positioned at their end, with the current line defined from one trace to the other.

The values of permeability and permittivity were extracted from the S-parameters resulting from this simulation using the method [43], modified so that negative imaginary parts of μ_r and ϵ_r indicate loss. These extracted parameters are shown in Fig. 3.26. Figure 3.26 (a) shows the results for a load of -129 nH. As shown, the low-frequency permeability of this simulation was quite high (around 3.7), which is predicted by (3.12) for cases where $|L_p| > L_r$. This simulation also exhibits negative permeability from 45 MHz to 95 MHz, which is a bandwidth of 71%. The minimum value of extracted permeability $-43.29 - j9.79$ occurs at 50 MHz. Figure 3.26 (b)

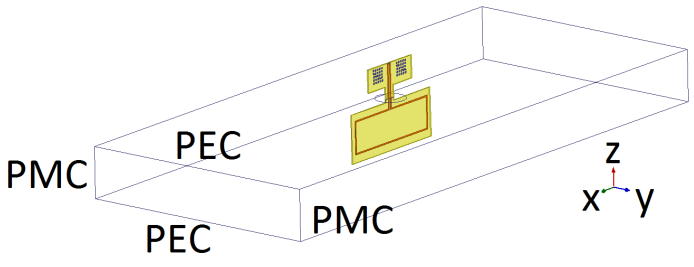

Figure 3.25: HFSS model of an SRR unit cell in a parallel plate waveguide

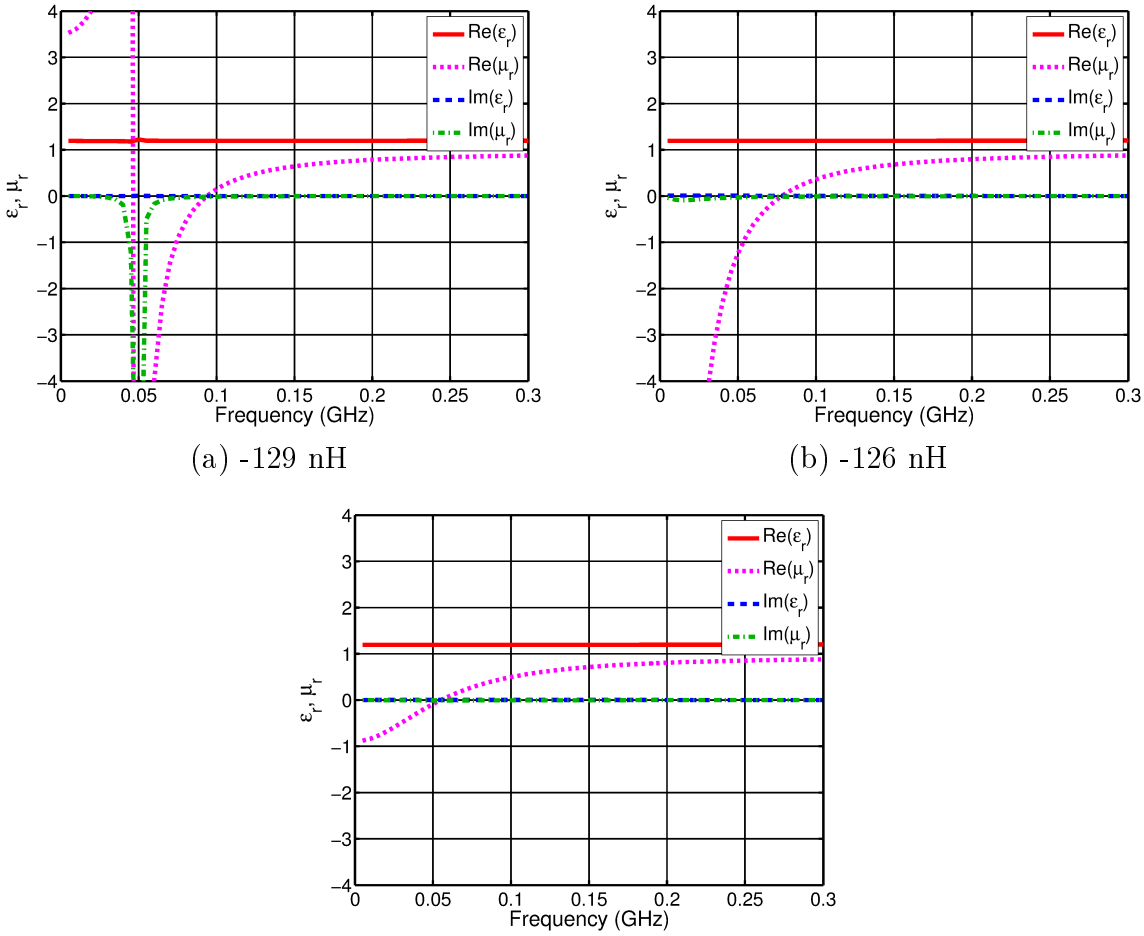

(a) -129 nH

(b) -126 nH

(c) -123 nH

Figure 3.26: HFSS simulation results for the SRR in a parallel plate waveguide loaded with (a) an ideal -129 nH inductor. (b) an ideal -126 nH inductor. (c) an ideal -123 nH inductor.

shows the results for a load of -126 nH. In this case, the low-frequency permeability has a large negative value, which is predicted by (3.12) for the cases where $|L_p| \sim L_r$ but $|L_p| < L_r$. The minimum extracted permeability for this case is -23.19 at 5 MHz, and the permeability is negative from 5 MHz to 80 MHz, a bandwidth of 176%. Finally, Fig. 3.26 (c) shows the extracted values for the SRR with a load of -123 nH. In this case the SRR exhibits a very weak negative magnetic susceptibility, with a minimum value of -0.88 at 5 MHz. This indicates that the magnitude of the load inductance is smaller than the intrinsic inductance, and that $L_p + L_r$ is a larger number than in the previous case. The permeability is negative from 5 MHz to 55 MHz,

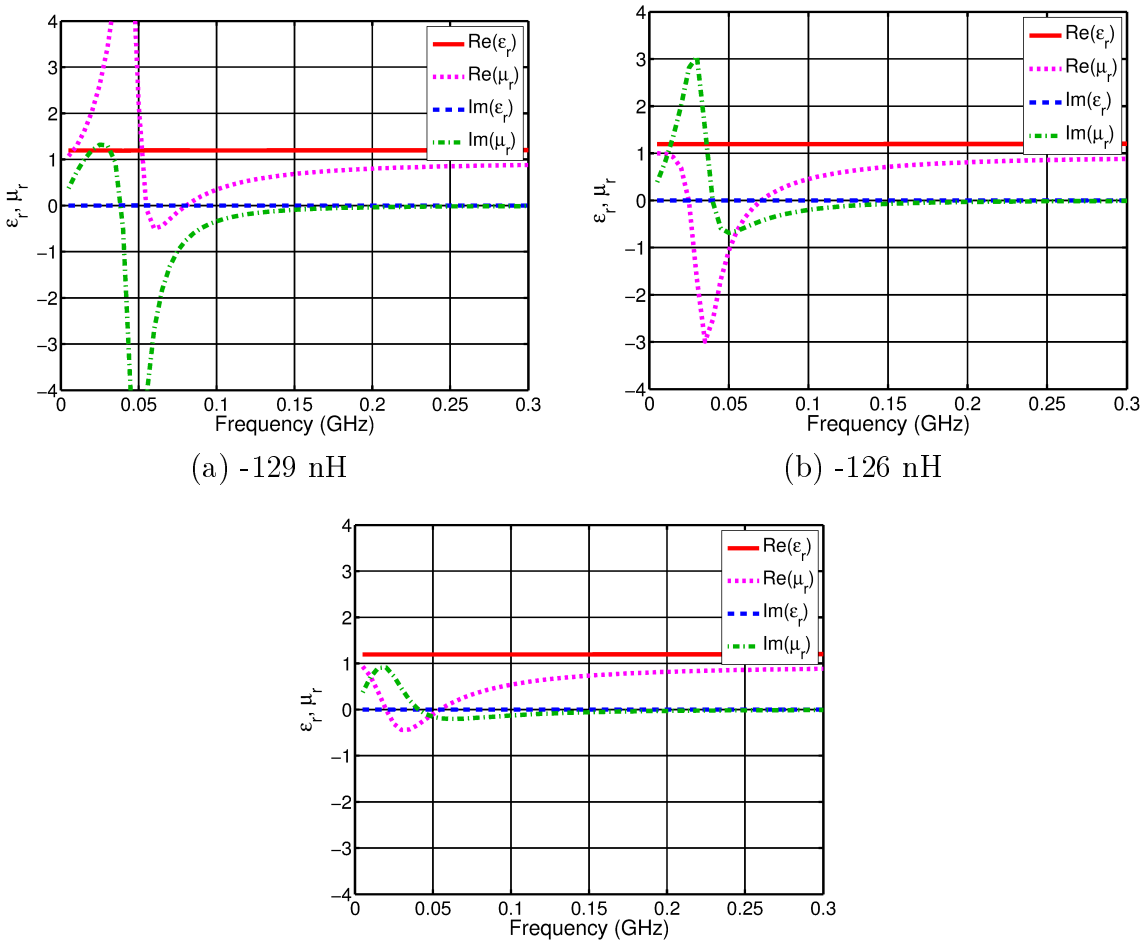

(a) -129 nH

(b) -126 nH

(c) -123 nH

Figure 3.27: HFSS simulation results for the SRR in a parallel plate waveguide loaded with (a) a -129 nH inductor having parasitic resistances $R_s = -0.5\ \Omega$ and $R_p = 2\ \text{k}\Omega$. (b) a -126 nH inductor having parasitic resistances $R_s = -0.5\ \Omega$ and $R_p = 2\ \text{k}\Omega$. (c) a -123 nH inductor having parasitic resistances $R_s = -0.5\ \Omega$ and $R_p = 2\ \text{k}\Omega$.

which is a bandwidth of 167%. These three simulations show that the value of μ_r can be tuned by changing the value of the non-Foster loading inductance.

Figure 3.27 presents the HFSS simulation results for a realistic non-Foster negative inductance, having series resistance $R_s = -0.5\ \Omega$ and parallel resistance $R_p = 2\ \text{k}\Omega$, in a parallel plate guide. Figure 3.27 (a) shows the results for a load inductance of -129 nH. As shown, this simulation shows high positive permeability at low frequencies, followed by a region of negative permittivity from 55 MHz to 80 MHz, a bandwidth of 37%. Gain is exhibited from 10 MHz to 40 MHz, and loss is exhibited from 40 MHz

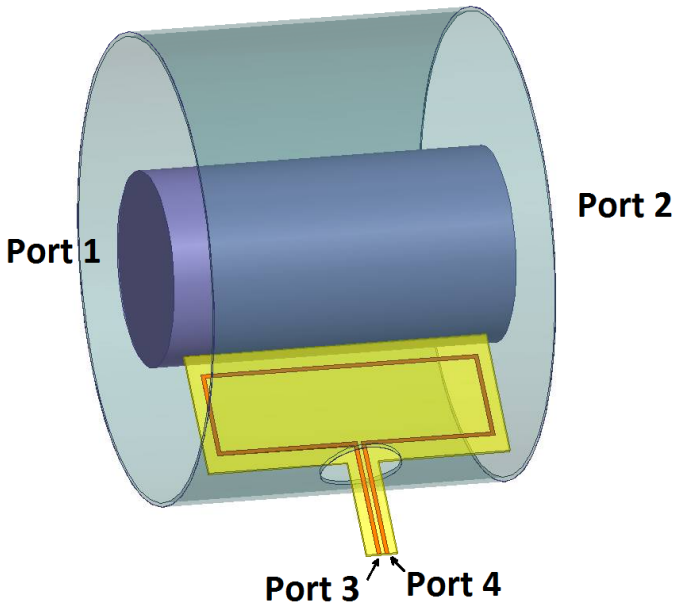

Figure 3.28: The SRR unit cell in a coaxial line section.

to 300 MHz. Figure 3.27 (b) shows the results for a load inductance of -126 nH. This simulation exhibits negative permeability from 25 MHz to 75 MHz, a bandwidth of 100%, with a minimum value of $-2.99 + j1.51$ at 35 MHz. Gain is observed from 10 MHz to 40 MHz, and loss is observed from 40 MHz to 300 MHz. Figure 3.27 (c) shows the extracted results for a load inductance of -123 nH. This simulation shows negative permeability over a bandwidth of 86%, from 20 MHz to 50 MHz. The minimum value of permeability is $-0.44 + j0.45$ at 30 MHz.

All the simulated and calculated results discussed thus far have been of the SRR in a parallel plate waveguide. However, the SRR was to be measured in the 3D printed test fixture discussed in section 3.2, as shown in Fig. 3.28. A simulation reflecting this geometry was performed in HFSS, using non-ideal loading with $R_s = -0.5\ \Omega$ and $R_p = 2\ \text{k}\Omega$. The resulting extracted parameters are shown in Fig. 3.29. Figure 3.29 (a) shows the results for a load inductance of -118 nH. This figure shows high permeability at frequencies below resonance, followed by a region of sub-unity permeability beginning at 50 MHz. The minimum value of permeability is

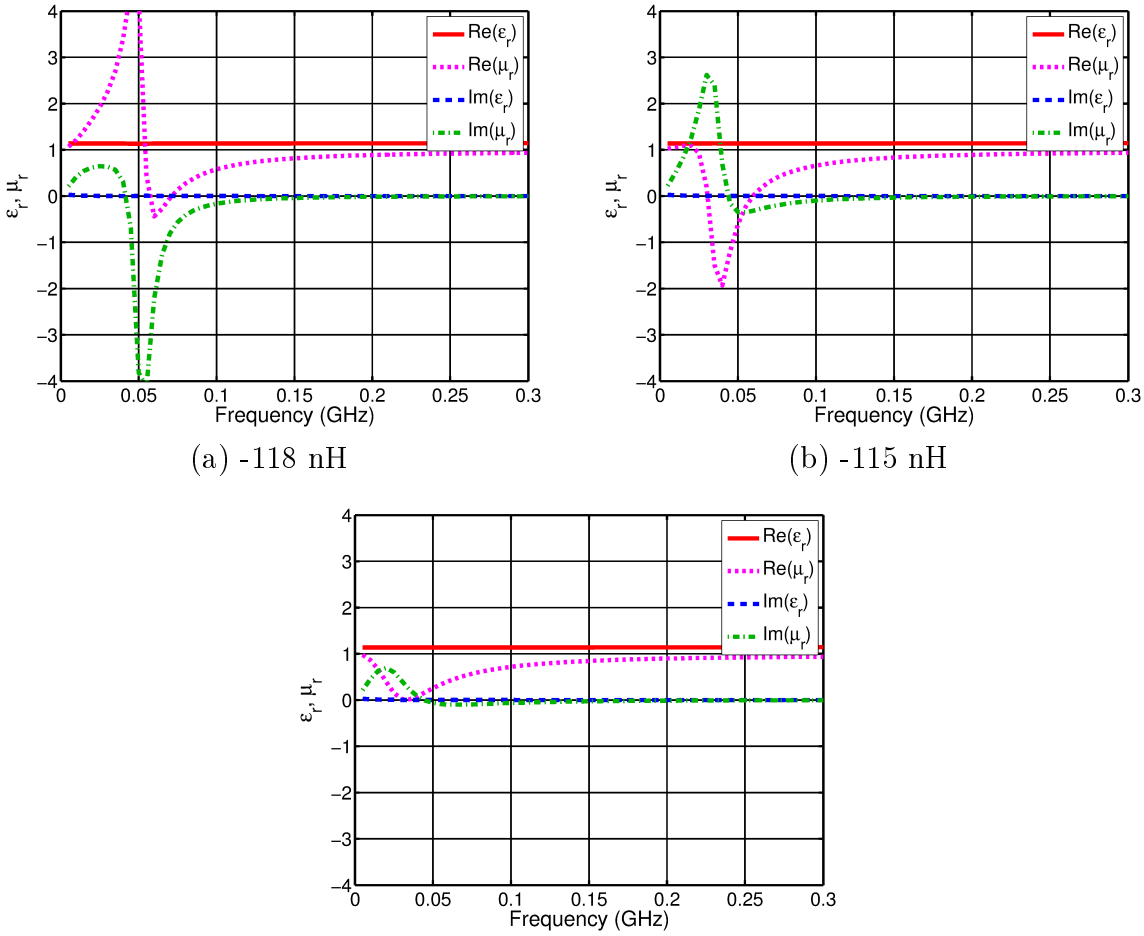

(a) -118 nH

(b) -115 nH

(c) -112 nH

Figure 3.29: HFSS simulation results for the SRR in a coaxial test fixture loaded with (a) a -118 nH inductor having parasitic resistances $R_s = -0.5\ \Omega$ and $R_p = 2\ \text{k}\Omega$. (b) a-115 nH inductor having parasitic resistances $R_s = -0.5\ \Omega$ and $R_p = 2\ \text{k}\Omega$. (c) a -112 nH inductor having parasitic resistances $R_s = -0.5\ \Omega$ and $R_p = 2\ \text{k}\Omega$.

$-0.4407 - j2.212$ at 60 MHz. Figure 3.29 (b) shows the results for a load inductance of -115 nH. This simulation shows a region of negative permeability from 35 MHz to 60 MHz, corresponding to a bandwidth of 50%. The minimum value of permeability is $-1.933 + j0.6859$ at 40 MHz. Gain is observed from 5 MHz to 45 MHz, and the rest of the spectrum is passive. Figure 3.29 (c) shows the permeability and permittivity resulting from a load inductance of -112 nH. This simulation does not show negative permeability, though permeability is significantly below unity over a large portion of the simulated range. The minimum value of permeability is $0.0132 + j0.2249$ at

35 MHz. Gain is observed from 5 MHz to 45 MHz, and the behavior is passive over the remainder of the simulated range.

As in the case of the CLS, it is likely that the measured response would be much stronger if the unit cell were repeated around the circumference of the coaxial line section. The frequency range of the negative permeability provided by this SRR overlaps with the range of the negative permittivity provided by the CLS presented in the previous section. The next goal of this research is to combine the two structures to form a wideband double-negative effective material. Such a wideband negative-index material can be integrated with electrically small antennas to increase their efficiency [2]. The unit cells presented here may also be used to develop cloaking devices [4] and perfect lenses [3] at low frequencies. Using more sophisticated fabrication techniques, they may also be scaled to allow performance at higher frequencies.

CHAPTER 4: FRACTAL METAMATERIAL

One of the most effective unit cell geometries to achieve negative permittivity is the electric disk resonator (EDR) [8] (see Fig. 4.1 (a)). This structure provides a large surface to interact with the incident electric field, and often exhibits a moderate frequency range over which an effective negative permittivity is attainable. Unfortunately, this structure is not easily manufactured because of its three dimensional shape. To simplify manufacturing and implementation, this structure may be approximated with a capacitively loaded strip [10] (see Fig. 4.1 (b)), which is simply a two-dimensional rendering of the three-dimensional geometry. This 2D structure has been explored and found to effectively induce negative permittivity, although its bandwidth is narrower, and the field interaction is weaker, than the three-dimensional version.

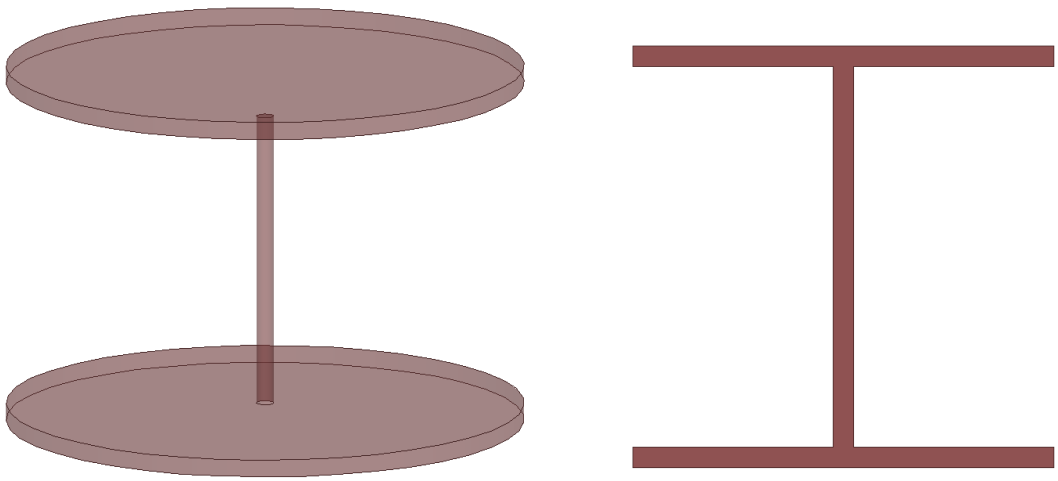

(a) (b)

Figure 4.1: (a) A three-dimensional EDR unit cell. (b) A two-dimensional CLS unit cell.

To broaden the bandwidth of this structure, [14] proposed a fractal expansion of the basic I-beam shape with additional replicas of this shape that would resonate at different frequencies. Unfortunately, the proposed fractal structure lacked continuous bandwidth, and instead exhibited multiple bands over which the desired response was achieved. In this chapter, the work of [14] and [15] is combined, with modification of the individual lengths of each part of the geometry, as well as the addition of discrete capacitively coupled resonators that broaden the bandwidth of this structure significantly.

4.1 The Single Unit Cell

Fig. 4.2 shows a single unit cell of the fractal metamaterial structure under consideration. The conductive traces have a thickness of 0.035 mm, and are positioned on a substrate of FR-4 epoxy having a thickness of 0.790 mm. The I-shape is central to the structure, with four secondary I-shapes on the ends of the primary I-shape. Two additional I-shapes were added in the middle of each side and are capacitively

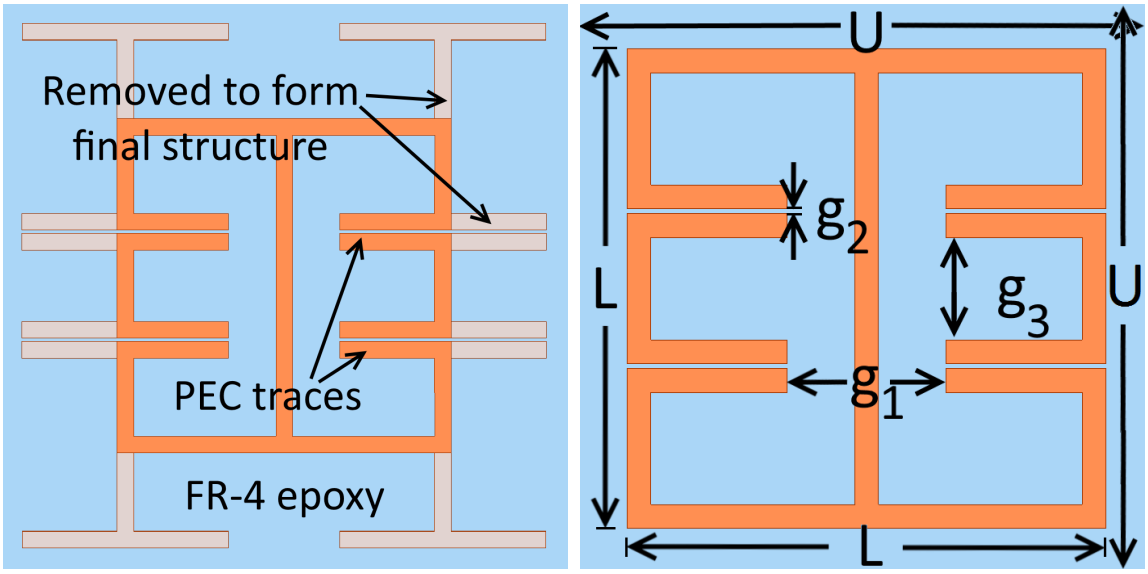

(a) (b)

Figure 4.2: (a) The complete fractal metamaterial unit cell. (b) The truncated fractal metamaterial unit cell, with dimensions $L = 20$ mm, $U = 22$ mm, $g_1 = 5$ mm, $g_2 = 0.5$ mm, $g_3 = 3.67$ mm, where all traces are 1 mm wide.

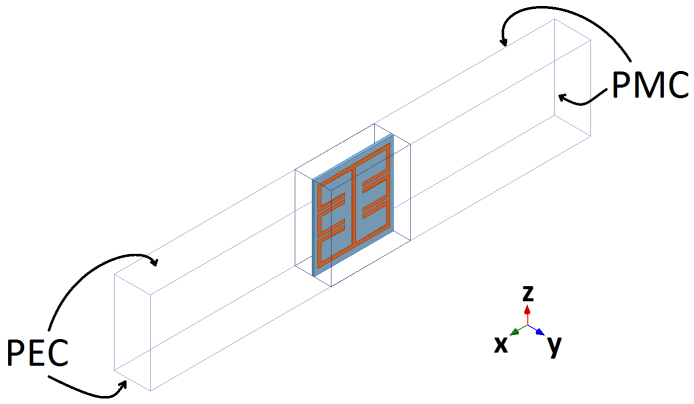

Figure 4.3: HFSS model of the fractal metamaterial in a parallel plate waveguide.

coupled to the primary fractal structure. The lengths of each section were optimized to widen the bandwidth over which the effective permittivity is negative. To improve performance of this unit cell, and reduce overall size, the geometry of Fig. 4.2 (a) was modified by truncation of the grayed-out sections to form the final structure shown in Fig. 4.2 (b), where $L = 20$ mm, $U = 22$ mm, $g_1 = 5$ mm, $g_2 = 0.5$ mm, $g_3 = 3.67$ mm, and all traces are 1 mm wide.

The single unit cell described above was simulated within a vacuum filled parallel plate waveguide using Ansys HFSS, as shown in Fig. 4.3. Parallel plate waveguide is commonly used for metamaterial characterization, because it supports TEM fields, and therefore the metamaterial in the parallel plate waveguide interacts with the field in a manner analagous to that of a metamaterial suspended in free space. The parallel plate waveguide model used in this simulation was 10 mm wide and 25 mm high. The horizontal sides at the top and bottom of the waveguide were defined as perfect electric conductor (PEC) and the vertical sides at the front and back were defined as perfect magnetic conductor (PMC).

The reflection and transmission resulting from simulation of this metamaterial are presented in Fig. 4.4. This figure reveals two resonant frequencies, characterized by high reflection. The first of these occurs at 1.45 GHz, where the unit cell size is slightly less than $\lambda_\circ/10$, and the second resonance occurs at 2.15 GHz. To demonstrate

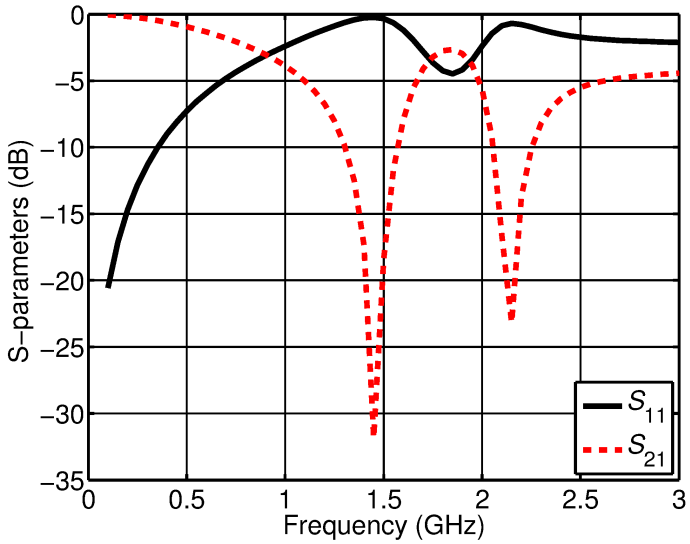

Figure 4.4: The reflection and transmission resulting from simulation of the single fractal metamaterial unit cell.

the nature of these resonances, the fields and currents are plotted at each resonant frequency. Figure 4.5 (a) shows the currents on the structure at 1.45 GHz, viewed from the positive y axis. As shown, the highest concentration of current is in the center trace, with the return path on the left and right sides. This current pattern is analogous to that of CLS, which is known to be a negative permittivity structure [10]. Figure 4.5 (b) shows the electric field in the waveguide at 1.45 GHz, viewed from the positive y-axis. Excitation is from the left. As shown, the incident field, which is pointing upward, flips direction to point downward as it travels into the unit cell. The incident field also undergoes drastic attenuation, so that very little of the field penetrates to the right side of the unit cell; both images are consistent with negative permittivity.

Figure 4.6 shows similar information for the second resonant frequency. Figure 4.6 (a) shows the currents on the structure at 2.15 GHz. In this case, the current is concentrated in the left side of the structure, with the return path on the center and right side posts. This current pattern is analogous to that of an SRR, which is a known negative-permeability structure. Figure 4.6 (b) shows the structure of the

magnetic field in the guide at 2.15 GHz, viewed from the positive z-axis. Excitation is from the left. As the electric field did at the previous resonance, the magnetic field exhibits a complete reversal as it passes into the unit cell. This figure also shows that the transmitted field is very small. Each of these results is consistent with a negative permeability material.

The relative permeability and permittivity of this metamaterial structure were calculated directly from the simulated scattering parameters using the extraction algorithm described in [43], modified so that negative imaginary permeability and permittivity correspond to loss. Fig. 4.7 shows the real parts of the extracted relative permeability and relative permittivity. As expected from the field plots of Figs. 4.5 and 4.6, the first resonance is characterized by negative permittivity, and the second by negative permeability. Permittivity is negative in the range 1.3 GHz – 1.75 GHz, corresponding to a bandwidth of 29.5%, and permeability is negative in the range 2.05 GHz – 2.45 GHz, corresponding to a bandwidth of 17.8%. It should be noted that in the region of negative permeability the unit cell is approximately $\lambda_\circ/7$ and thus may not be considered electrically small. It is also noteworthy that the value of the extracted effective permittivity is quite high far from resonance. At 100 MHz the extracted permittivity is 5.1. This is most likely due to the presence of metal in the parallel plate waveguide. To demonstrate this effect in isolation, a square of metal,

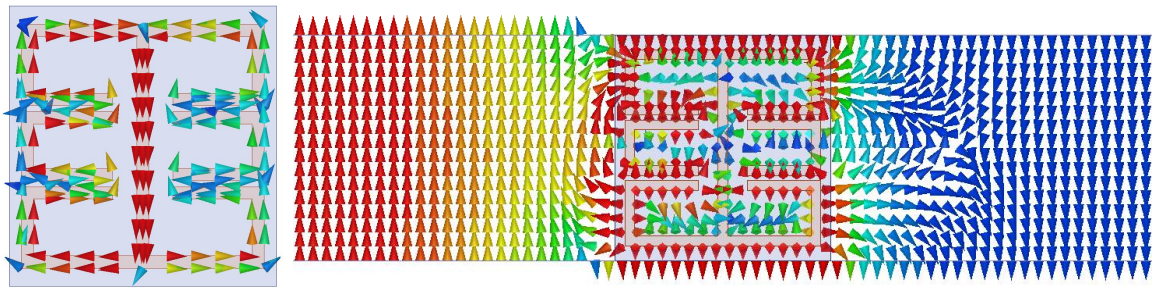

(a) (b)

Figure 4.5: (a) The current on the structure at 1.45 GHz, viewed from the positive y direction. (b) The E-field inside the waveguide at 1.45 GHz, viewed from the positive y direction.

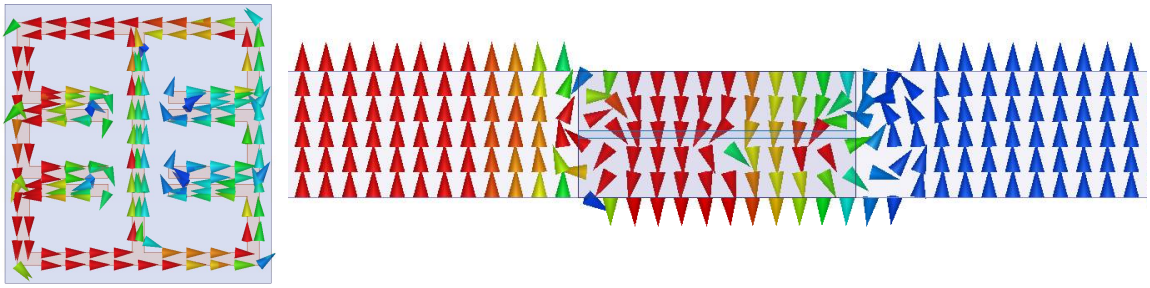

(a) (b)

Figure 4.6: (a) The current on the structure at 2.15 GHz, viewed from the positive y direction. (b) The H field inside the waveguide at 2.15 GHz, viewed from the positive z direction.

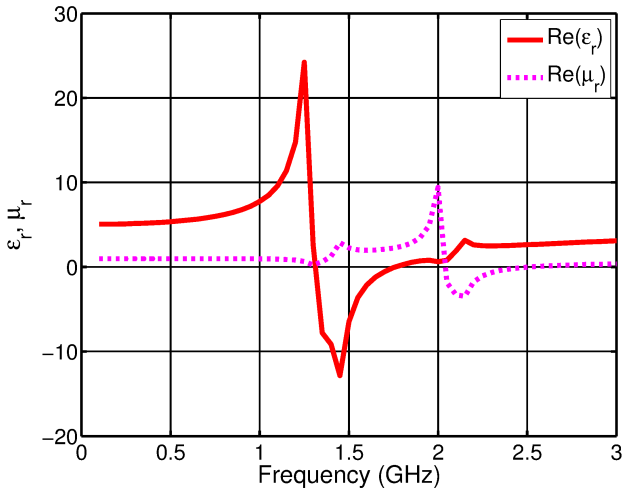

Figure 4.7: The real part of the extracted permeability and permittivity for the simulation of the proposed unit cell.

having height and width of 20 mm, to match the fractal structure, was simulated. This structure is shown in Fig. 4.8 (a), and its extracted effective permeability and permittivity are shown in Fig. 4.8 (b). As shown, the presence of the plain metal sheet in the waveguide resulted in elevated extracted effective permittivity. At 100 MHz, this structure results in an extracted permittivity of 5.3. The increase of permittivity with increased frequency is probably due to a resonance of the metal sheet itself, which occurs at a frequency above the range of the present sweep.

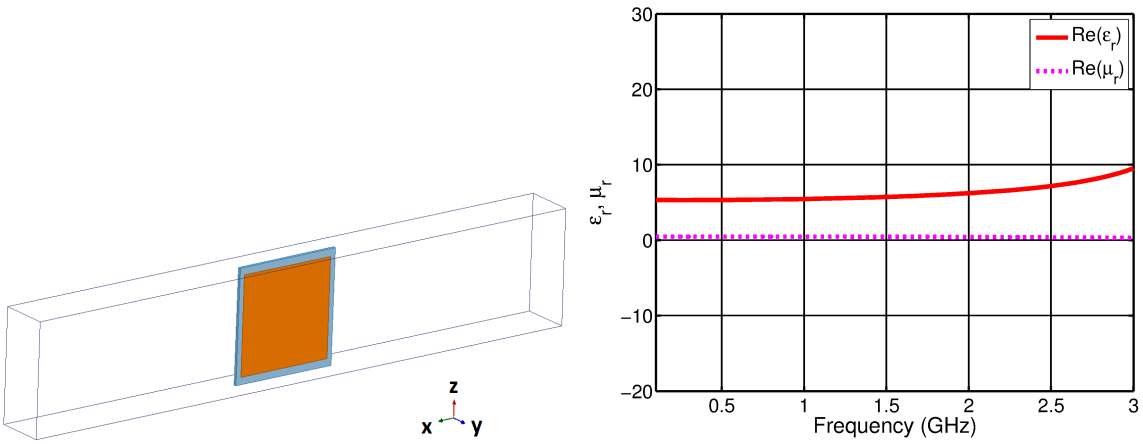

(a) (b)

Figure 4.8: (a) A metal sheet with the same dimensions as the fractal structure. (b) The extracted effective permeability and permittivity of the metal sheet.

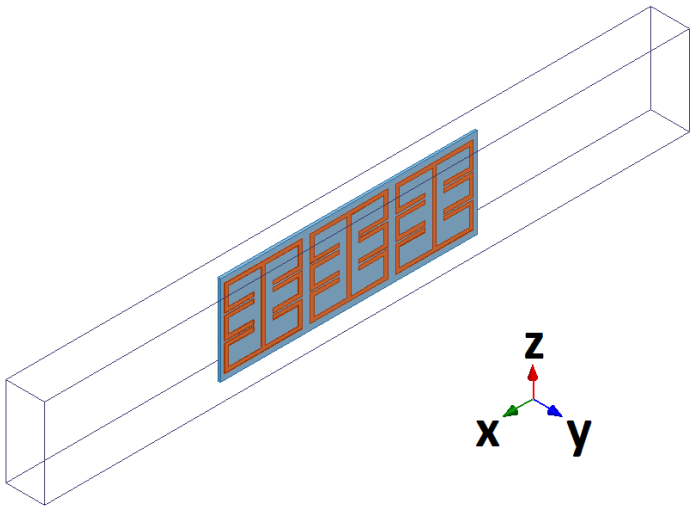

Figure 4.9: Three fractal structures in the same waveguide as discussed previously.

4.2 Simulation of Three Unit Cells

The single unit cell was then extended to three side-by-side structures, as shown in Fig. 4.9. The three unit cells were simulated in the same parallel plate waveguide model as discussed previously, where the height of the guide was 22 mm, the width was 10 mm, and the horizontal and vertical sides were defined as PEC and PMC, respectively.

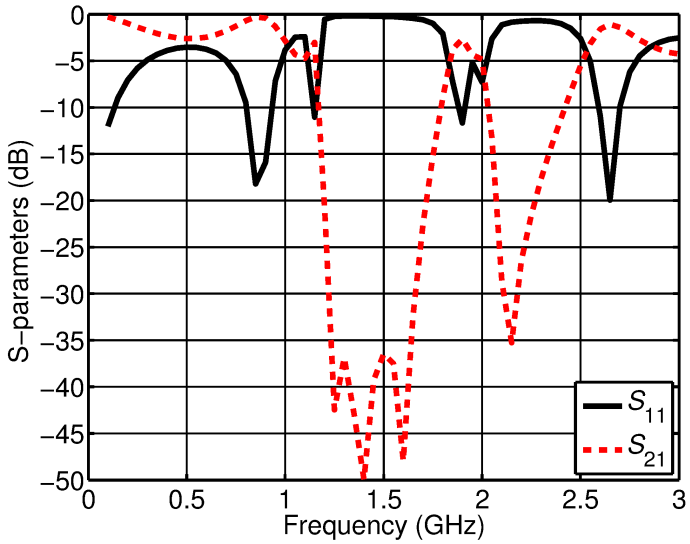

Figure 4.10: S-parameters resulting from the simulation of three side-by-side fractal unit cells in a parallel plate waveguide.

Figure 4.10 shows the S-parameters resulting from this simulation. In this case, instead of exhibiting a single sharply defined resonance at 1.45 GHz, as in the case of the single unit cell, the first reflective region appears to consist of three closely spaced resonances at 1.25 GHz, 1.40 GHz, and 1.60 GHz. The second reflection remained a single point at 2.15 GHz. These changes are most likely a product of inter-element coupling between the three unit cells. Fig. 4.11 shows the extracted values of permeability and permittivity. As shown, this simulation has a region of negative permittivity from 1.25 GHz to 1.80 GHz, corresponding to a bandwidth of approximately 36%. This is a 6.5% increase over the single-cell simulation. The region of negative permeability extends from 2.05 GHz to 2.40 GHz, corresponding to a bandwidth of 15.7%. This is a decrease of 2.1% from the single-cell case.

To explore the significance of various features of the unit cell, two additional structures were simulated. In the first case, shown in Fig. 4.12, the two gaps in each of the left and right side posts have been replaced by a single gap, having the same dimensions as the in the original case. This structure resembles one presented in [44]. The S-parameters and extracted permeability and permittivity are shown in Fig. 4.13.

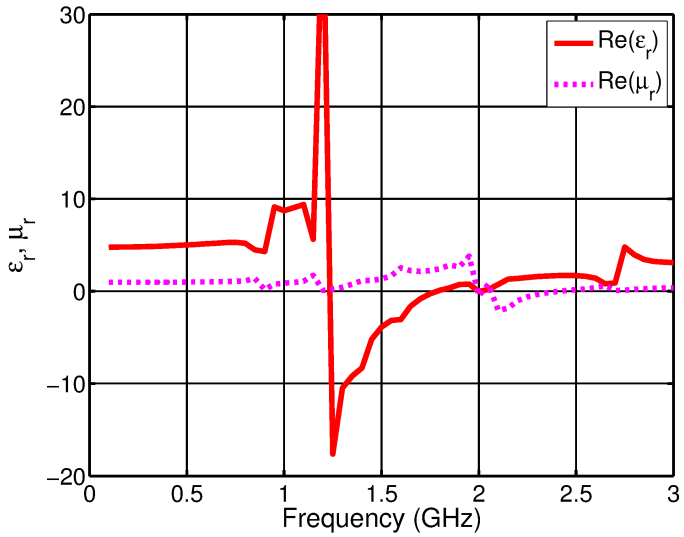

Figure 4.11: Extracted permeability and permittivity from the simulation of three side-by-side fractal unit cells in a parallel plate waveguide.

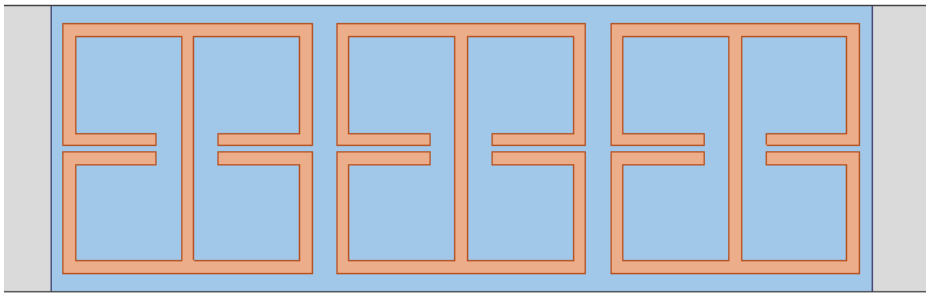

Figure 4.12: Three unit cells for a structure where a single gap has replaced the two gaps on either side of each unit cell.

As shown in Fig. 4.13 (a), this structure resonates at three frequencies: 1.05 GHz, 1.15 GHz, and 1.5 GHz. The extraction shows that the first two resonances correspond to negative permittivity, which is demonstrated from 1.05 GHz to 1.25 GHz, a bandwidth of 17.4%. The third resonance corresponds to negative permeability, which is demonstrated from 1.4 GHz to 1.8 GHz. By comparison of these results with the results shown in Fig. 4.11, it can bee seen that the effect of the second gap is to broaden the bandwidth, and to strengthen the magnetic response.

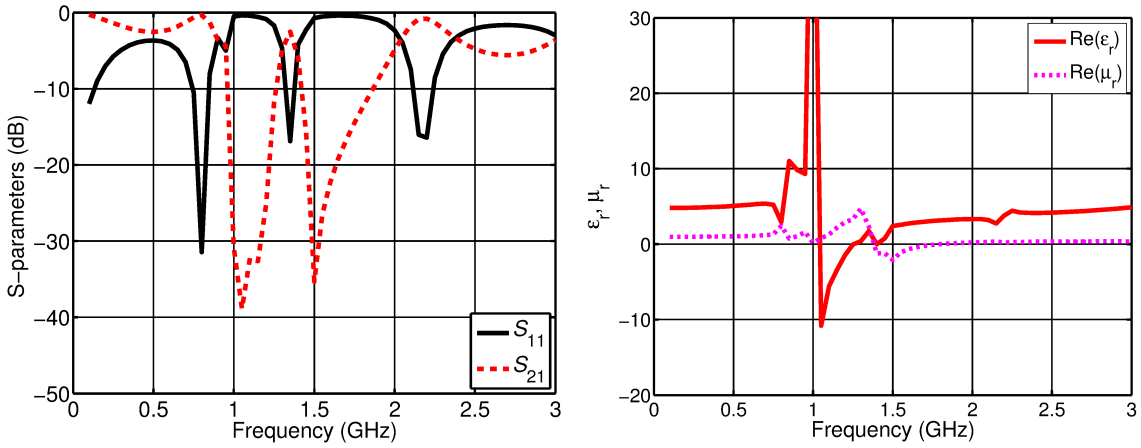

(a) (b)

Figure 4.13: (a) The reflection and transmission for three unit cells of the structure with a single gap on either side. (b) The extracted permeability and permittivity for three unit cells of the structure with a single gap on either side.

In the second case, shown in Fig. 4.14, the continuous part of the structure is identical to the original case, but the two detached side pieces have been removed. As shown in Fig. 4.15 (a), this structure shows four resonances, three of which are in close proximity, just as in Fig. 4.10. In this case, these three resonant frequencies occur at 1.4 GHz, 1.65 GHz, and 2.1 GHz. The extraction shown in Fig. 4.15 (b) reveals that, as previously, the three close resonances resulted in negative permittivity, spanning from 1.4 GHz to 2.45 GHz, which is a bandwidth of 55%. Thus, it is seen that the effect of the two loading pieces of the structure is to pull the electric response to lower frequencies, at the cost of bandwidth. The maximum dimension of the structure is 20 mm, which corresponds to $\lambda/10$ at 1.5 GHz. Thus, minimizing the size of the structure is more critical than increasing the bandwidth. The fourth resonance observed in Fig. 4.15 (a) is at 2.8 GHz. As shown, this resonance is much weaker than in the case of the original structure. As previously, it produced a slight dip in permeability, which is negative from 2.65 GHz to 2.8 GHz.

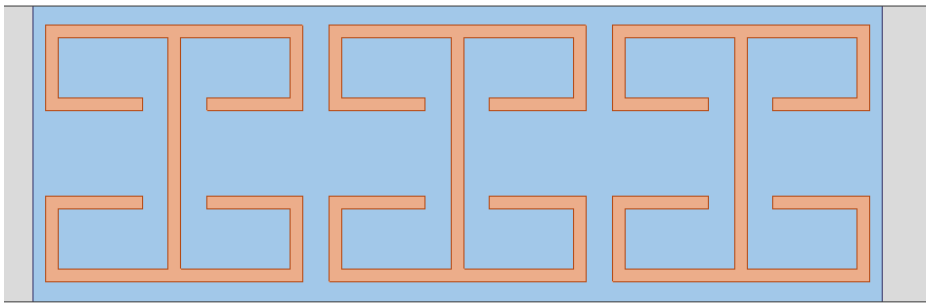

Figure 4.14: Three unit cells for a structure where a the loading element has been removed from either side of the unit cell.

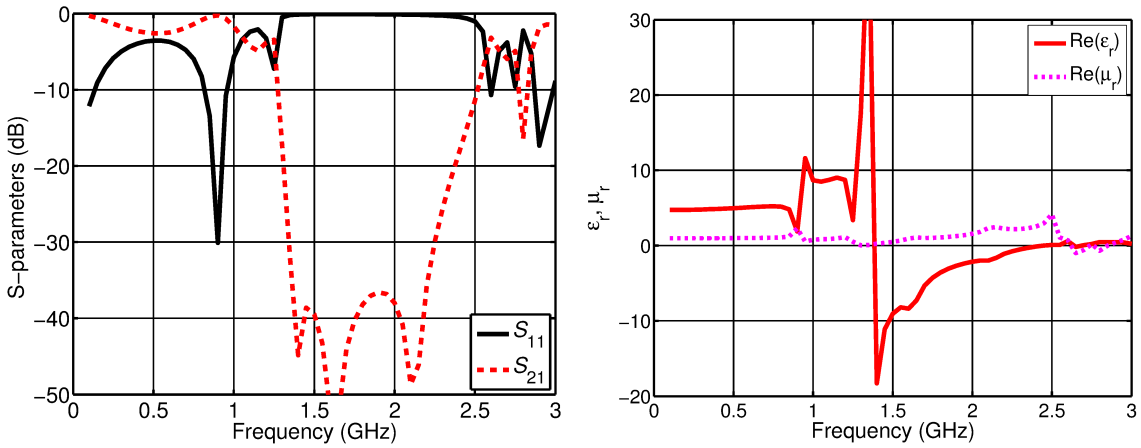

(a) (b)

Figure 4.15: (a) The reflection and transmission for three unit cells of the structure with the loading element removed from either side. (b) The extracted permeability and permittivity for three unit cells of the structure with the loading element removed from either side.

4.3 Measurement of Three Unit Cells

All the simulations up to this point have been conducted in parallel plate waveguide, because parallel plate waveguide has a field structure analagous to that of free space. However, the structure was measured in a 3D printed coaxial test fixture consisting of solid ABS plastic overlaid with copper foil, having an inner radius of 3.175 mm and an outer radius of 26.675 mm (see Fig. 4.16).

This structure is discussed in more detail in [45]. Though both parallel plate waveguides and coaxial transmission lines support TEM wave propagation, there

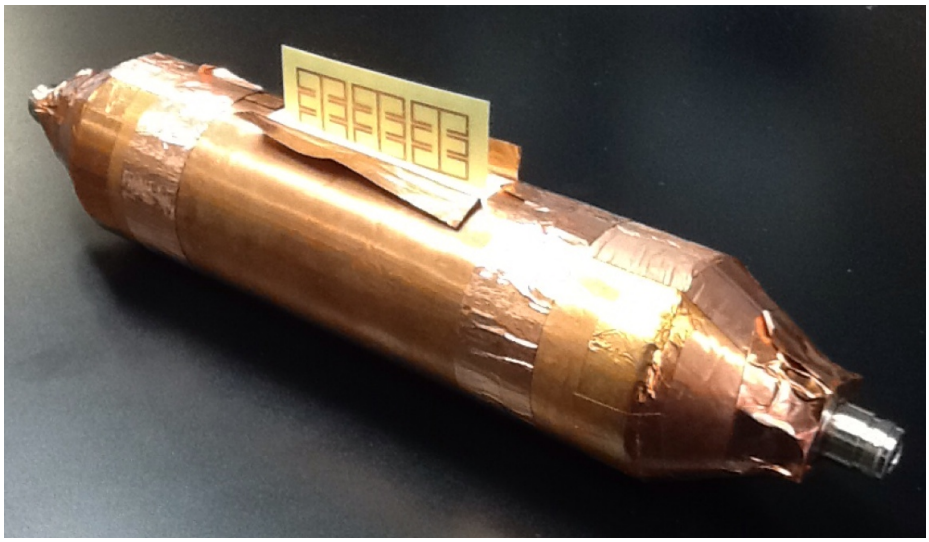

Figure 4.16: A 3D printed test fixture, consisting of solid ABS plastic overlaid with copper foil.

are several key differences between the two structures. Firstly, the images reflected by the PEC and PMC boundaries will be different. The parallel plate waveguide has straight PEC and PMC boundaries. These boundaries will result in infinitely repeating image currents in both the y-dimension and the z-dimension. In the z-dimension, the PEC boundaries will result in alternating reversal of the transverse currents, but consistently-directed normal currents. In the y-dimension, the PMC boundaries will result in alternating reversal of the normal currents, but consistently-directed transverse currents. Also, because the PEC and PMC boundaries are planar, the images will all have the same size as the actual metamaterial structure. The coaxial fixture has PEC boundaries, which will result in infinitely repeating images in the radial dimension, with alternately reversed transverse currents, and consistently-directed normal currents. However, the curvature of the PEC boundaries in the z- and y- dimensions will result in warping of the radial images, as discussed in [45]. For the sake of completeness, it should also be noted that the coaxial fixture has infinitely repeating currents in the azimuthal dimension as well, occurring every 2π radians, and having exactly the same shape and distribution as on the original structure.

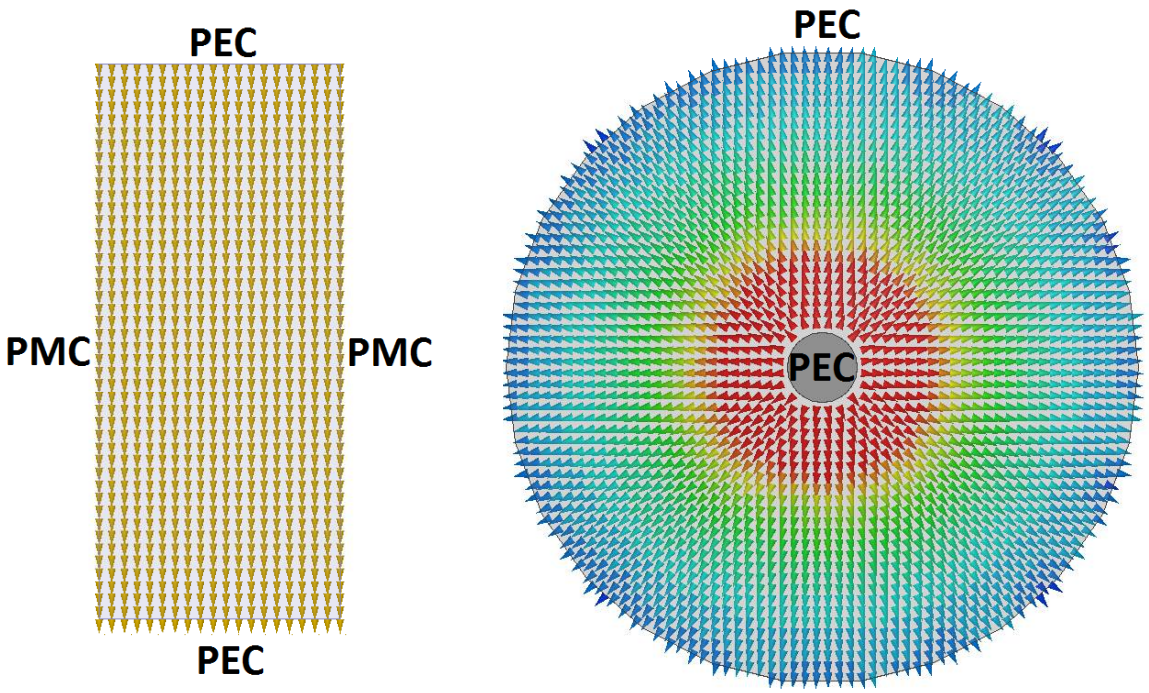

(a) (b)

Figure 4.17: (a) The distribution of the electric field in a parallel plate waveguide. (b) The distribution of the electric field in the coaxial fixture.

Secondly, the field distribution in the parallel plate case is different than the coaxial case. As shown in Fig. 4.17, the field in an empty parallel plate waveguide is uniformly distributed in both the y-dimension and the z-dimension. Also as shown, the field in a coaxial structure decays with the inverse of the radius. Thus, the field is significantly stronger just outside the center conductor than it is just inside the outer conductor.

Thirdly, because the cross-sectional area of the coaxial fixture is much larger than the cross-sectional area of the parallel plate waveguide, the inserted metamaterial structure will interact with a smaller percentage of the field, producing a weaker response. To illustrate this point, the coaxial fixture containing a 45° wedge of material with $\epsilon_r = -1$ was simulated in HFSS. The simulated structure, as well as the extracted permeability and permittivity, are shown in Fig. 4.18. As shown, the extracted value of relative permittivity is around 0.77. This suggests that perhaps a weighted average would be an appropriate approximation of the effect of a partial

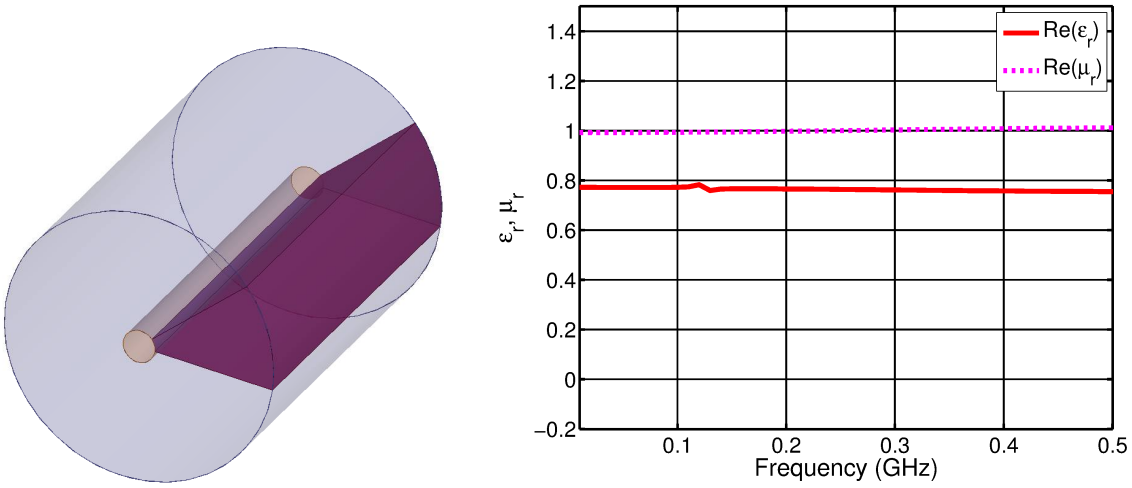

(a) (b)

Figure 4.18: (a) A section of coaxial waveguide with inner radius 3.175 mm and outer radius 26.675 mm, containing a 45° wedge of material with $\epsilon_r = -1$, and otherwise filled with a vacuum. (b) The extracted permeability and permittivity resulting from this simulation.

dielectric fill. For example,

$$\frac{\theta_w \epsilon_w}{360^\circ} + \frac{360^\circ - \theta_w}{360^\circ} = \frac{45^\circ(-1)}{360^\circ} + \frac{315^\circ}{360^\circ} = 0.75 \approx 0.77 \tag{4.1}$$

where θ_w is the angle of the wedge, and ϵ_w is its dielectric constant. However, in the case of the metamaterial being measured, there is no method for determining what 'effective angle' would be appropriate, since the effective permittivity ϵ_e of the metamaterial is not independently known.

The final difference between the coaxial and parallel plate test fixtures is that the material properties of the empty test fixtures are different. The parallel plate waveguide is vacuum-filled, but the coaxial test structure was printed of solid ABS plastic, which has a higher dielectric constant. The value of $\eta_\circ$ used in the extraction was adjusted to reflect the dielectric constant of the embedding medium.

The simulation was adjusted to reflect the geometry and material of the test fixture. Figure 4.19 (a) shows the simulated S-parameters for the three unit cells in the coaxial

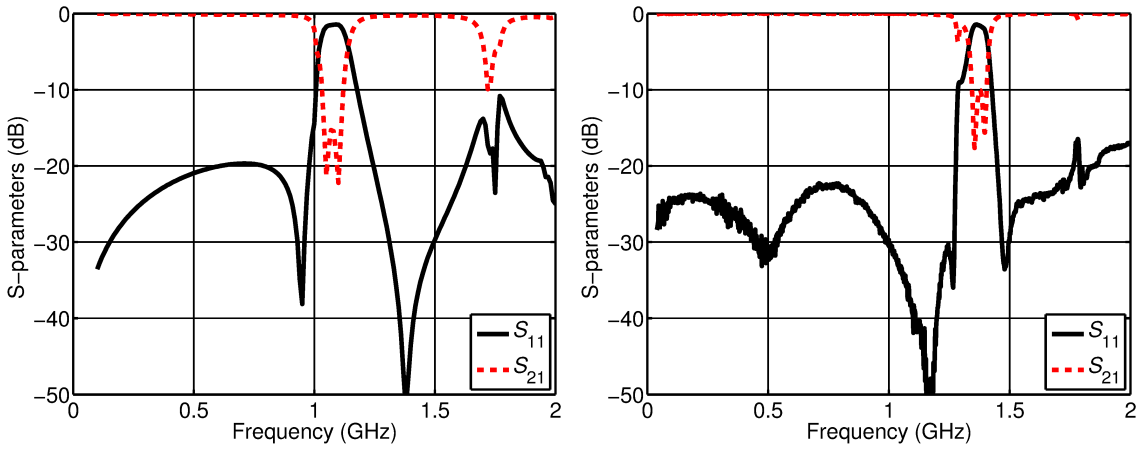

Figure 4.19: (a) S-parameters resulting from simulation of three side-by-side fractal unit cells in a coaxial fixture filled with ABS plastic. (b) S-parameters resulting from measurement of three side-by-side fractal unit cells in a coaxial fixture filled with ABS plastic.

fixture. As shown, the electric response is narrower than in the case of Fig. 4.10, and has shifted to a lower frequency range. There are only three visible resonant frequencies; two are closely spaced at 1.05 GHz and at 1.1 GHz, and one occurs at 1.72 GHz. The measured S-parameters are shown in Fig. 4.19 (b), and show nearly the same features as the simulated S-parameters, but shifted to slightly higher frequencies. Three resonances are observed at 1.29 GHz, 1.36 GHz, and 1.40 GHz, and a fourth, though very weak, appears at 1.79 GHz.

Figure 4.20 (a) shows the extracted permeability and permittivity resulting from the simulation. Permittivity is negative over a bandwidth of 7%, from approximately 1.045 GHz to 1.12 GHz. It is important to note that the difference in bandwidth between this simulation and the one shown in Fig. 4.11 is due solely to the change in test fixture. The 7% bandwidth in the coaxial ABS fixture is equivalent to the 36% bandwidth in the free-space analogue.

The fractal structure was milled out on 1/32" FR-4 epoxy; the measured S-parameters are shown in Fig. 4.19 (b). The measured bandwidth of extracted negative permittivity, shown in Fig. 4.20 (b), is 6.4%, which is 91% of the simulated band-

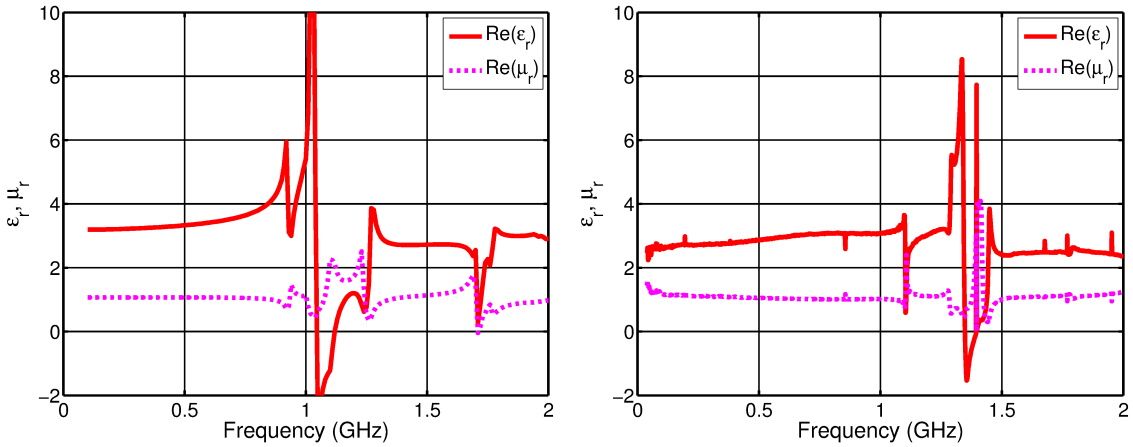

Figure 4.20: (a) Extracted permeability and permittivity resulting from simulation of three side-by-side fractal unit cells in a coaxial fixture filled with ABS plastic. (b) Extracted permeability and permittivity resulting from measurement of three side-by-side fractal unit cells in a coaxial fixture filled with ABS plastic.

width. If the effect of the differing test fixtures is linear, the measured bandwidth in the coaxial fixture corresponds to a bandwidth of 32.9% in a parallel plate waveguide.

4.4 Simulation and Measurement of Fractal Interlocking Grid

As an extension of this fractal structure, an interlocking grid was devised, following the same branching I-shape pattern. This grid is shown in Fig. 4.21. The unit cell of this interlocking grid is outlined with a dashed black line. The dimensions of the unit cell are 6.5 mm by 7 mm, which is equal to $\lambda/10$ at 4.3 GHz, and the height of the entire structure is 19 mm. This structure was first simulated in a parallel plate waveguide with height = 22.15 mm and width = 47.55 mm, where the vertical sides were defined as PMC and the horizontal sides were defined as PEC. These dimensions correspond to those of a WR-187 rectangular waveguide. The S-parameters resulting from this simulation are shown in Fig. 4.23 (a). This simulation shows two resonant frequencies in close proximity - one at 3.7 GHz, and the other at 3.8 GHz. The extracted permeability and permittivity are shown in Fig. 4.23 (b). This structure exhibits negative permittivity over the range 3.63 GHz – 4.35 GHz, corresponding to

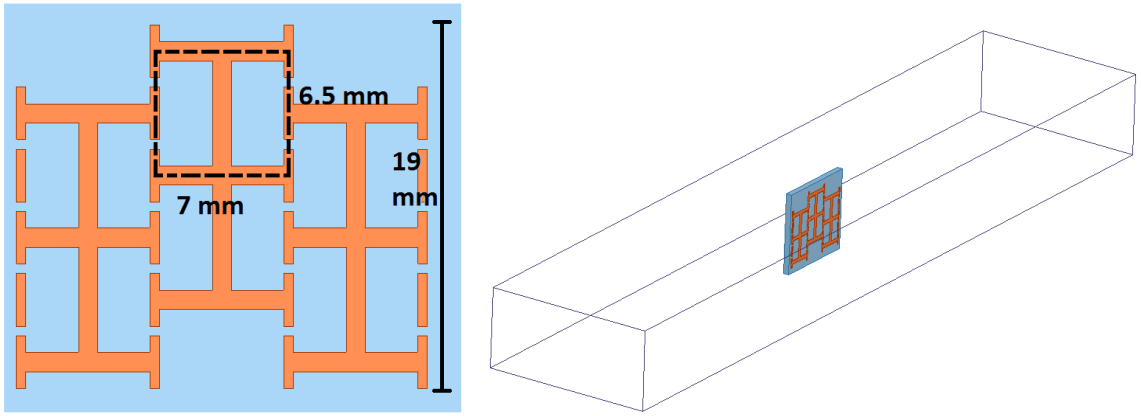

(a) (b)

Figure 4.21: (a) Extention of I-shaped fractal structure to an interlocking grid. (b) The parallel plate waveguide simulation, where the guide model has the same dimensions as a WR-187 rectangular waveguide.

a bandwidth of 18%. Again, though the parallel plate case gives the best free-space approximation, the metamaterial was measured in a more convenient structure, which in this case was a 3D printed WR-187 rectangular waveguide section (shown in Fig. 4.22). Unlike the parallel plate and coaxial waveguide structures, rectangular waveguide does not support TEM propagation. At these frequencies, the propagating mode is TE_{10}, with a cutoff frequency of 3.15 GHz. The next mode begins at 6.3 GHz. Because all four sides of rectangular waveguide are defined as PEC, the reflections will result in alternately directed transverse currents and consistently directed normal currents. Additionally, the electric field, which is evenly distributed in the parallel plate waveguide, is concentrated in the center of the rectangular waveguide, as shown in Fig. 4.24.

Figure 4.25 shows the S-parameters for the simulated and measured cases of the interlocking grid structure in a rectangular waveguide section where the height was 22.15 mm and the width was 47.55 mm. Note that these dimensions are identical to those used in the parallel plate case above; the only difference between the two simulations is that in this case both the vertical and the horizontal sides are defined as PEC. Like the parallel plate waveguide simulation, the rectangular waveguide

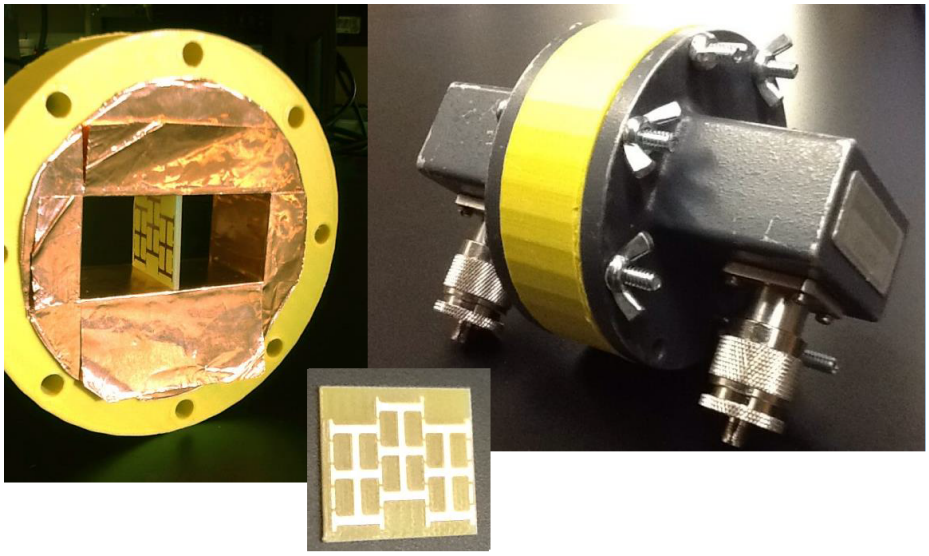

Figure 4.22: Measurement of interlocking grid.

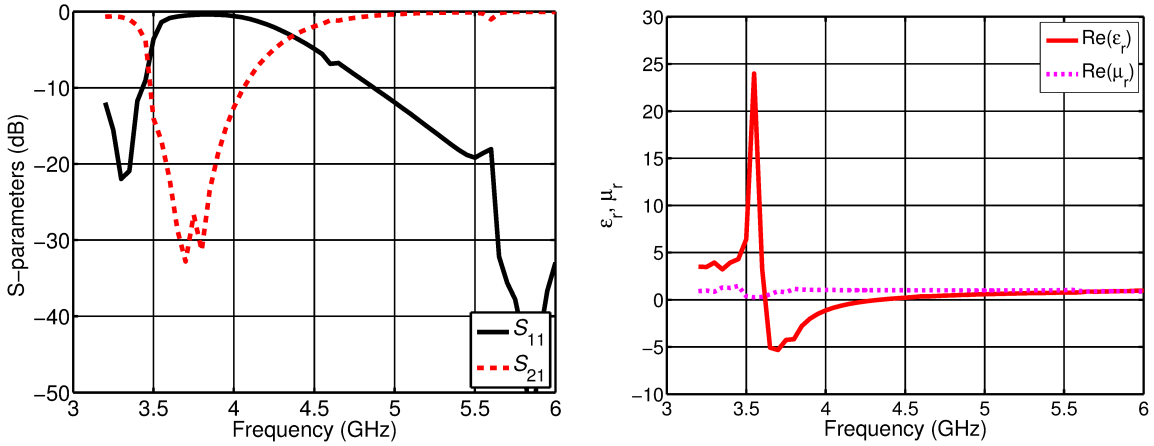

(a) (b)

Figure 4.23: (a) S-parameters resulting from simulation of interlocking fractal grid in a parallel plate waveguide. (b) Extracted permeability and permittivity resulting from simulation of interlocking fractal grid in a parallel plate waveguide.

simulation shows two resonant frequencies in S_{21}, located at 3.85 GHz and at 4.9 GHz. The wider spacing between these two resonances results in a wider bandwidth of negative permittivity, as shown in Fig. 4.26. The region of negative permittivity spans from 3.85 GHz to 5.9 GHz, corresponding to a bandwidth of 42%. The results shown in Fig. 4.23 are equivalent to the results shown in Fig. 4.25 (a) and Fig. 4.26 (a);

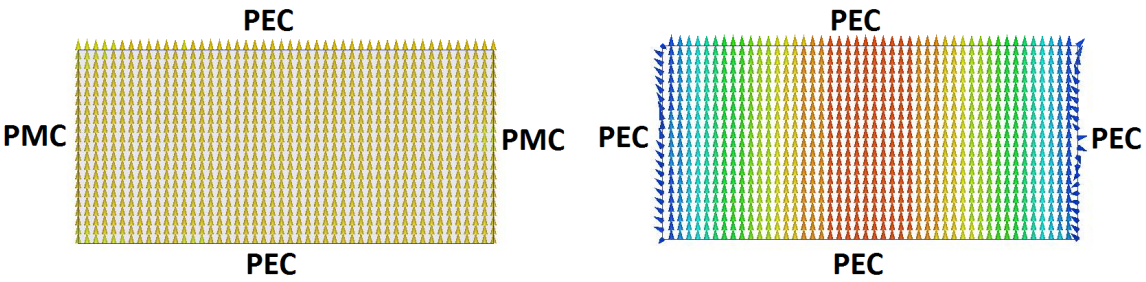

(a) (b)

Figure 4.24: (a) The distribution of the electric field in a parallel plate waveguide. (b) The distribution of the electric field in a rectangular waveguide.

the only difference between the two simulations was the definition of the boundaries on the test fixture.

The interlocking grid structure was milled out on 1/16" FR-4 epoxy, and measured in the 3D printed WR-187 waveguide section shown in Fig. 4.22. Figure 4.25 shows the measured S-parameters. In this figure, the two resonant frequencies are observed at 3.98 GHz and 4.93 GHz. These frequencies are slightly higher than those seen in simulation. The extraction shown in Fig. 4.26 (b) shows that the region of measured negative permittivity is from 3.9 GHz to 5.85 GHz, corresponding to a bandwidth of 40%. If the effect of the differing test fixtures is linear, the measured bandwidth in the rectangular waveguide fixture corresponds to a bandwidth of 17.1% in a parallel plate waveguide.

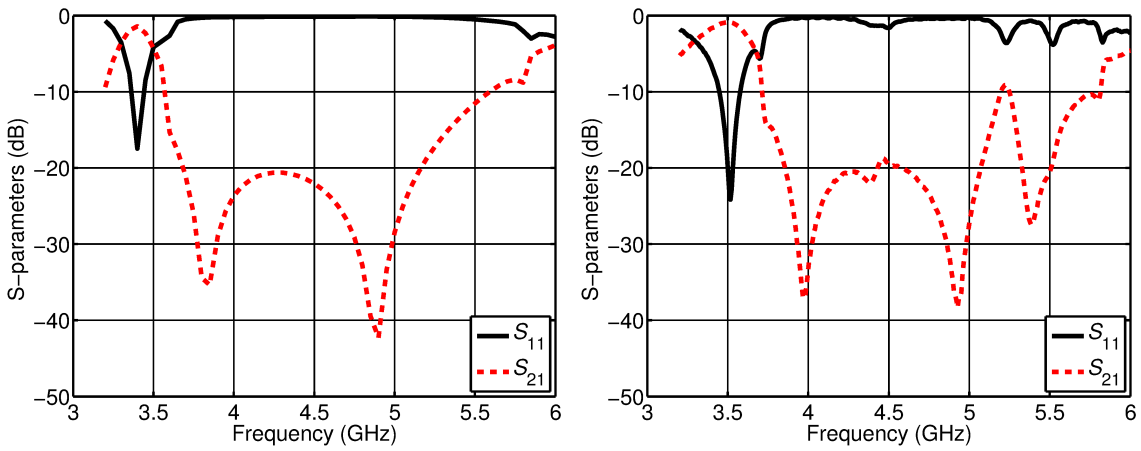

Figure 4.25: (a) S-parameters resulting from simulation of interlocking fractal grid in a WR-187 rectangular waveguide. (b) S-parameters resulting from measurement of interlocking fractal grid in a WR-187 rectangular waveguide.

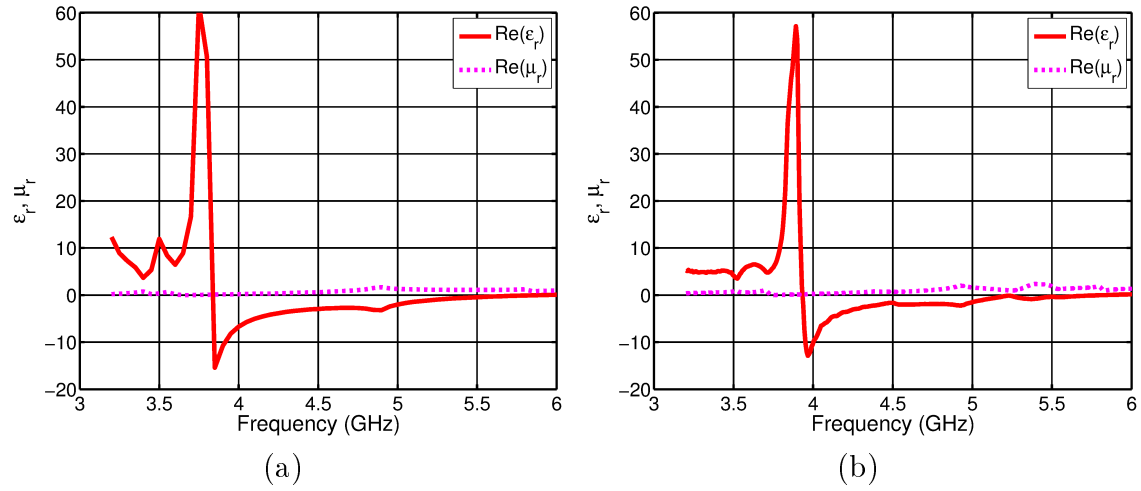

Figure 4.26: (a) Extracted permeability and permittivity resulting from simulation of interlocking fractal grid. (b) Extracted permeability and permittivity resulting from measurement of interlocking fractal grid.

CHAPTER 5: 3D FRACTAL TREE MONOPOLE ANTENNAS

Dipole antennas are widely utilized in communication applications, because they have excellent cross-polarization and a symmetric radiation pattern. They radiate over a very narrow band, typically at the frequency where the length of the antenna is half of the wavelength.. However, dipoles typically require complicated feed structures, such as baluns, to balance the feed to the two sides of the antenna [17]. Monopole antennas overcome this complication by using a ground plane to mirror a single radiating element, emulating the behavior of a dipole without the necessity of feeding two sides. Monopole antennas are attractive alternatives to dipoles because of their simple construction and because they are smaller than dipoles without sacrificing a dipole's excellent cross-polarization and symmetric radiation pattern. However, like dipoles, they also are extremely narrowband. The antennas presented here have a monopole configuration, but use fractal methods to improve the bandwidth.

Fractal geometries are formed by scaled repetitions of a basic shape [27]. When applied to antennas, these geometries have been shown to support multiband and wideband performance, as different portions of the structure become active at different frequencies. This property is demonstrated clearly in [33], where a forth-order Sierpinski fractal monopole antenna is reported to operate at multiple frequencies, with similar current patterns setting up in progressively smaller portions of the antenna as the frequency increased. It was also reported that at high frequencies the inactive portions acted as loading on the active portions, pulling their resonance to lower frequencies.

In [38], a two-dimensional fractal tree monopole antenna like that shown in Fig. 5.1 (a) is presented. The curve in the ground plane acts as a matching network for the

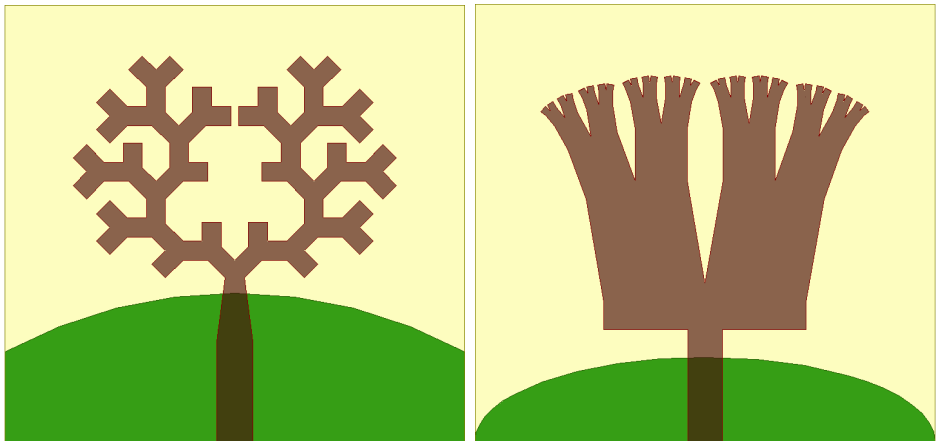

(a) (b)

Figure 5.1: (a) A two-dimensional fractal tree antenna, as presented in [38]. (b) A two-dimensional fractal tree antenna, as presented in [39].

radiating element. This antenna has a height of 11.57 mm, and its measured S_{11} is reported to be below -10 dB over a band from 2.1 GHz to 11.52 GHz.

A second two-dimensional fractal tree monopole antenna is presented in [39], like that shown in Fig. 5.1 (b). Again, a curved ground plane is used to match the radiating element to the microstrip feed line. This antenna has a height of 13.41 mm, and its measured S_{11} is reported to be below 10 dB from 2.6 GHz to 11.14 GHz.

These antennas demonstrate excellent return loss over a wide band of frequencies, but their radiation characteristics are poor, with high cross-polarization and asymmetric radiation in both the E-plane and the H-plane.

A collection of three-dimensional fractal tree dipole antennas consisting of very thin wires are presented in [40]. These antennas are shown to have multiple narrow bands of performance, tunable by changing the branch angles, number of rotational repetitions, and number of fractal iterations. Their radiation characteristics are much better than the two-dimensional antennas in [38] and [39]. However, these antennas are explored only through simulation, because of the prohibitive complexity of fabricating such structures.

This chapter will present two three-dimensional fractal tree monopole antennas

with buildable dimensions. The first antenna consists of three iterations of four-way branching cubes. This antenna exhibits less than 10 dB return loss over a 181.0% bandwidth, but shows poor polarization characteristics, especially at high frequencies. It is noted that high frequencies also result in high current concentrations at the corners of the highly angular fractal body. In an attempt to eliminate this odd current distribution, a cone-based antenna is presented. This second antenna consists of an iterated branching conical structure, with a much smoother profile than the cube-based antenna. This antenna is shown to have much better polarization behavior than the cube-based antenna, while maintaining a high bandwidth of 180.7%. This antenna is explored in more detail than the previous, with several simulated variations presented. Finally, the best of the simulated variations was fabricated with a 3D printer, and measured results are presented.

5.1 Geometry of Cubic Fractal Tree Monopole Antenna

The cubic fractal monopole antenna presented in this chapter consists of three iterations of progressively smaller cubes in a branching pattern. as shown in Fig. 5.2. Each iteration n is made up of four cubes with side length ℓ_n, as shown in Fig. 5.3. The low inside corner of each cube meets the low inside corners of the other three cubes in the center of the structure. The low outside corner of each cube meets one corner of a square having side length ℓ_{n-1} (shown in Fig. 5.3). As shown, the cubes have some slight spatial overlap, which assures that, when the cubes are united, the underside of the the structure forms a continuous surface. The vertical space between the square and the surface formed by the undersides of the cubes was filled, to produce a single solid form. For each iteration n, the process was repeated, using the tops of the cubes from iteration $n-1$ as the base square for iteration n. Three such iterations form the main body of the radiating element. In order to transition from an RG-58C/U 50Ω coaxial line to this body, a tapering section was designed. This taper was formed of a cone with a height of 15 mm, a lower radius of 1 mm, and an

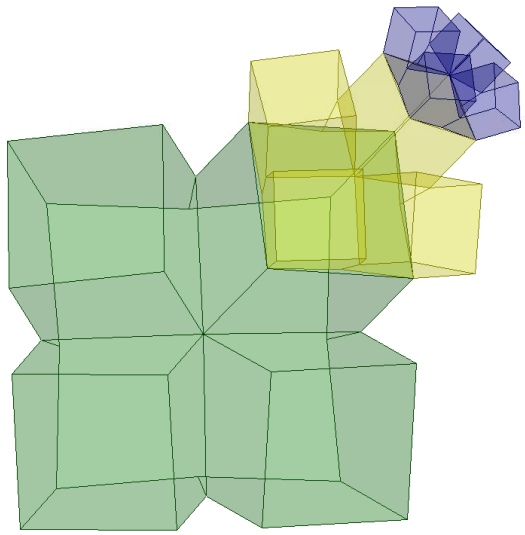

Figure 5.2: Three iterations of the cubic fractal monopole antenna.

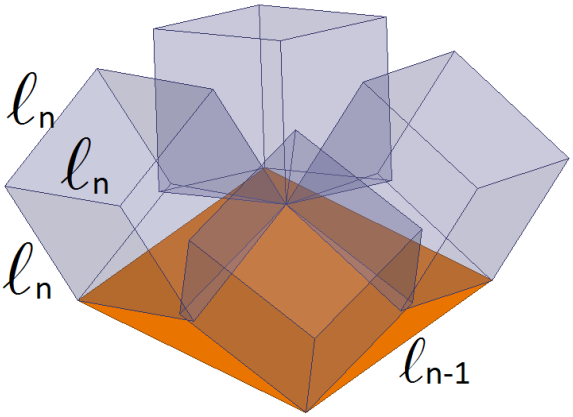

Figure 5.3: The initiator of the cubic fractal monopole antenna.

upper radius equal to $\frac{1}{\sqrt{2}}$ of ℓ_0, the side length of the base square upon which the first iteration was built. Four planar facets were cut into this cone from the first iteration square to the lower cone radius, resulting finally in a tapered solid that transitions from a circle with a 1 mm radius to a square with a side length of ℓ_0. This structure is shown in Fig. 5.4. The ground surface of the monopole antenna was formed of the upper half of an oblate spheroid having major radius 30 mm and minor radius 9 mm, which is separated from the taper section of the antenna by an 0.8 mm gap.

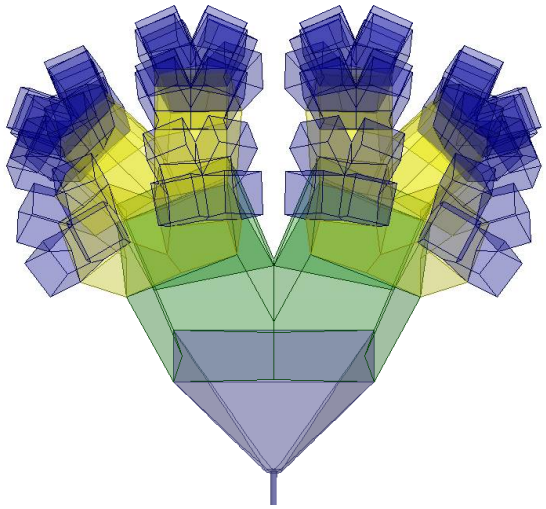

Figure 5.4: The fractal body of the antenna and taper section for transition from the feed coax.

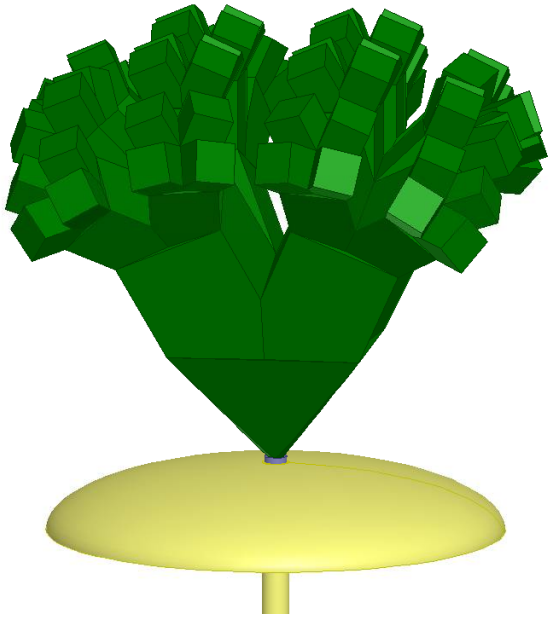

Figure 5.5: The cubic fractal monopole antenna.

The major and minor radii of the ground, the height of the taper section, and the separation between the ground and the main body of the antenna were optimized for maximum power transfer. The entire resulting antenna is shown in Fig. 5.5.

Table 5.1: Dimensions of cubic fractal tree monopole antenna

Iteration #	ℓ (mm)
0	25.32
1	15.16
2	9.08
3	5.43

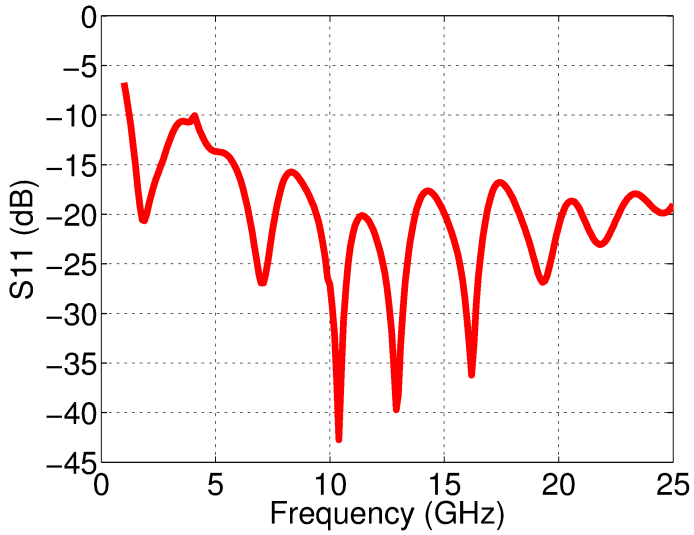

Figure 5.6: The return loss of the cubic fractal monopole antenna.

5.2 Simulation of Cubic Fractal Tree Monopole Antenna

The cubic fractal tree monopole antenna with three fractal iterations shown in Fig. 5.5 was built in HFSS, having the cube dimensions given in Table 5.1. The antenna had an overall height, not including the ground, of 57.3 mm, and a maximum radius of 41.3 mm. This antenna was simulated in a cylindrical airbox with a radius of 60 mm and height of 113.6 mm. In order to ensure valid far-field simulation results from 5 GHz to 10 GHz, this box was required to be at least $\lambda/4 = 15$ mm away from the antenna at 5 GHz, and to have a mesh operation on its surface to constrain the mesh length to $\lambda/6 = 5$ mm at 10 GHz. The simulation converged with 204,406 tetrahedra, after two consecutive adaptive passes with $|\Delta S| < 0.01$. The return loss resulting from this simulation is given in Fig. 5.6.

As shown, the return loss of this antenna is less than 10 dB from 1.24 GHz to 25 GHz, corresponding to a bandwidth of 181%. Two more simulations were performed, adjusting the size of the airbox and the mesh constraint to validate the results for far field radiation at 1.5 GHz and 15 GHz. The E-plane radiation pattern and cross-polarization of this antenna in dB are shown at 1.5 GHz, 5.5 GHz, 10 GHz, and 15 GHz in Fig. 5.7. The corresponding H-plane radiation pattern and cross-polarization are shown in Fig. 5.8.

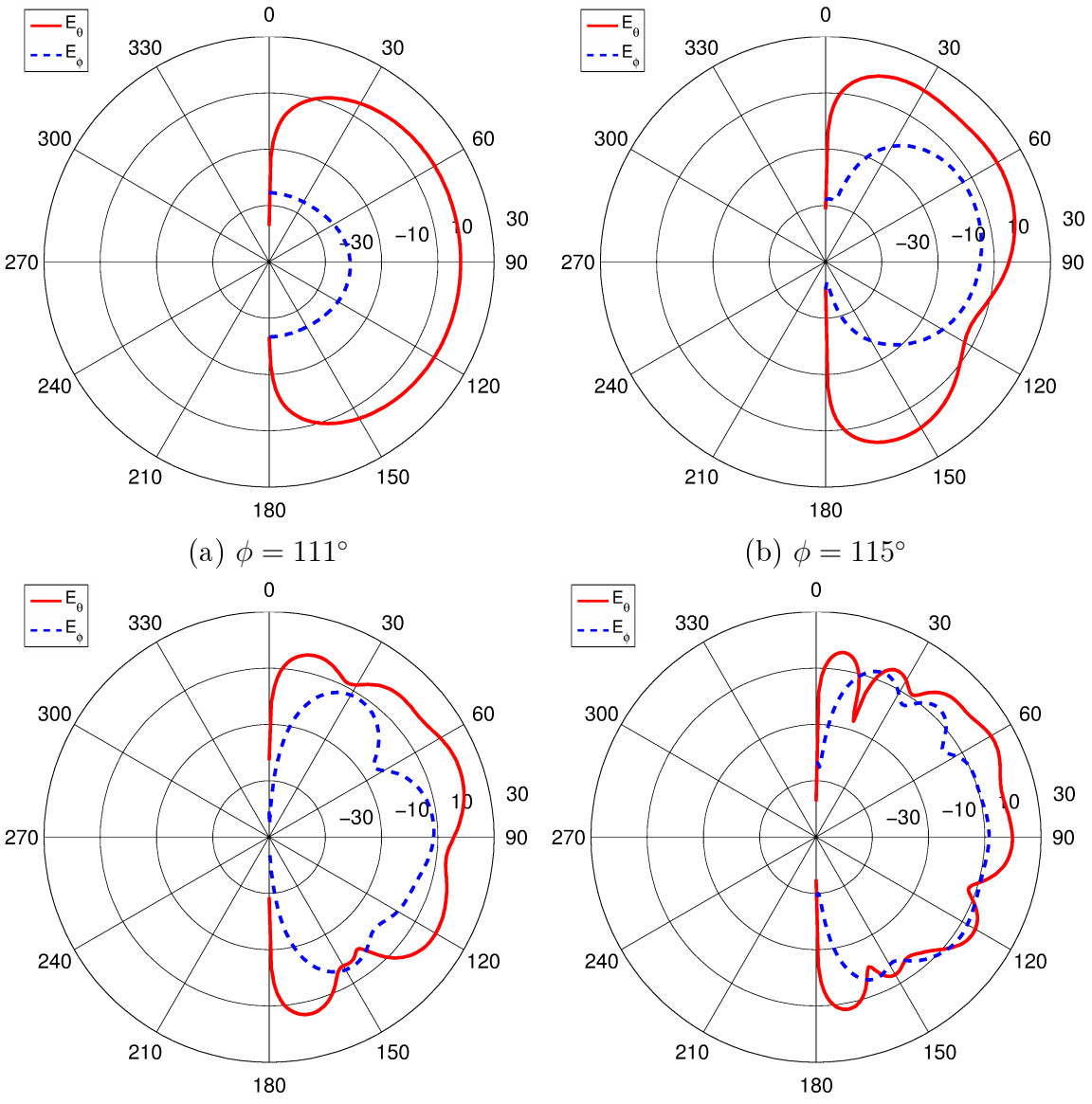

(a) $\phi = 111°$ (b) $\phi = 115°$

(c) $\phi = 79°$ (d) $\phi = 15°$

Figure 5.7: E-plane radiation pattern for cubic three-iteration fractal tree antenna at (a) 1.5 GHz. (b) 5.5 GHz. (c) 10 GHz. (d) 15 GHz.

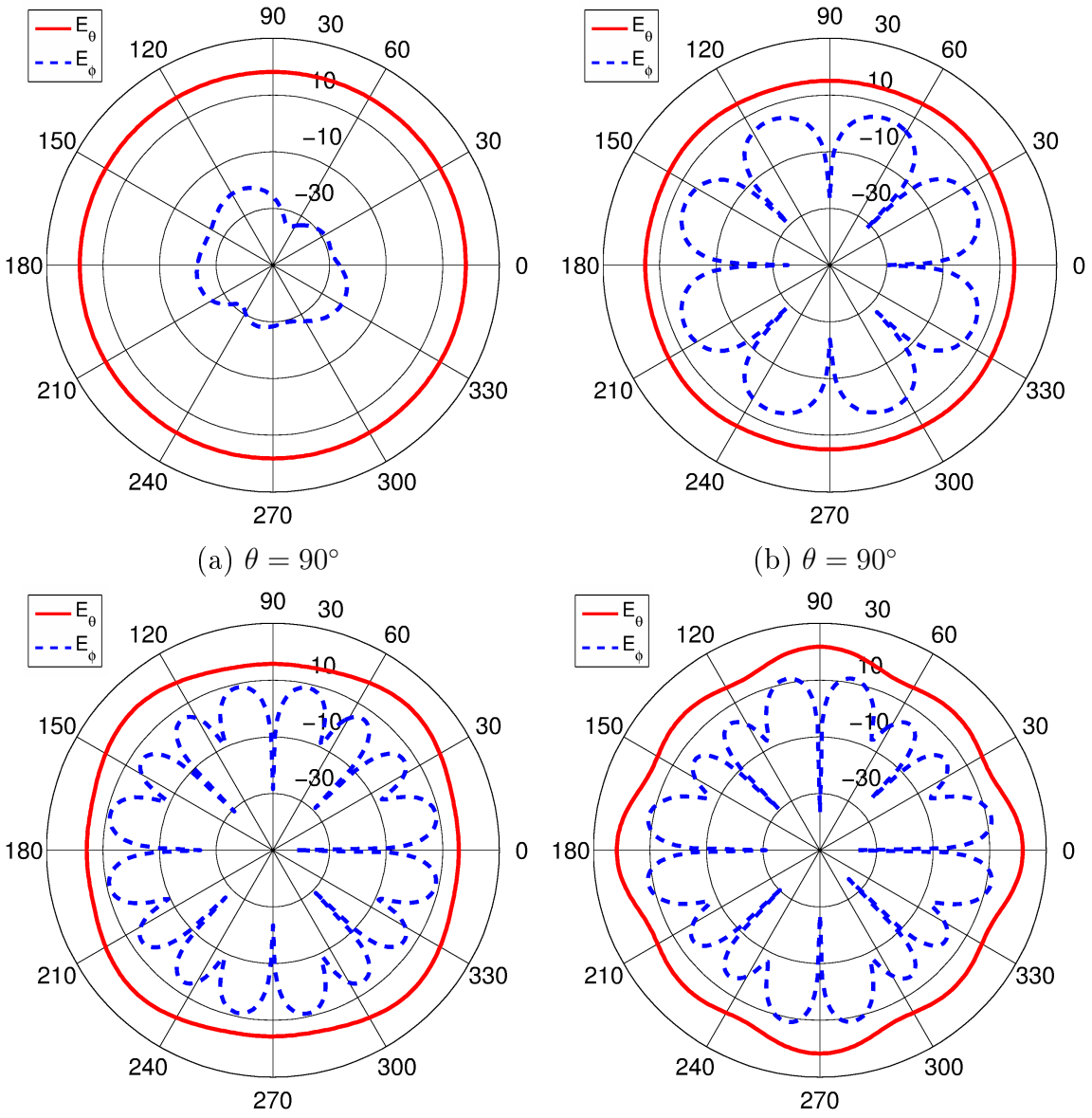

(a) $\theta = 90°$ (b) $\theta = 90°$

(c) $\theta = 90°$ (d) $\theta = 90°$

Figure 5.8: H-plane radiation pattern for cubic three-iteration fractal tree antenna at (a) 1.5 GHz. (b) 5.5 GHz. (c) 10 GHz. (d) 15 GHz.

Table 5.2: Worst-case cross-polarization at four representative frequencies

Frequency (GHz)	Cross-Polarization (dB)
1.5	10.1
5.5	5.8
10	- 4.8
15	- 18.3

As can be seen from these plots, the cross-polarization grows drastically worse with increasing frequency. At 1.5 GHz, the cross-polarization is better than 10.1 dB (excluding at the extreme angles of $\theta = 0°$ and $\theta = 180°$). At 5.5 GHz, the worst-case cross-polarization has increased to 5.8 dB. At 10 GHz and 15 GHz, the cross-polarization is actually higher in places than the co-polarization by 4.8 dB and 18.3 dB, respectively. These results are tabulated in Table 5.2.

Figure 5.9 shows the magnitude of the surface currents on the antenna at 1.5 GHz, 5.5 GHz, 10 GHz, and 15 GHz. The range from blue to red is 0 A/m–3 A/m in every

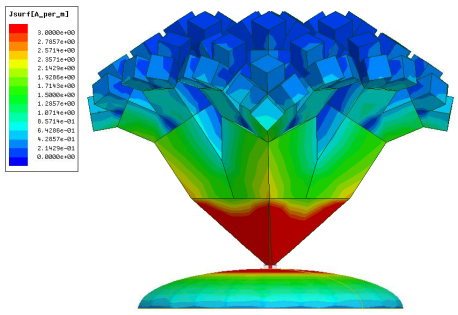

(a) 1.5 GHz

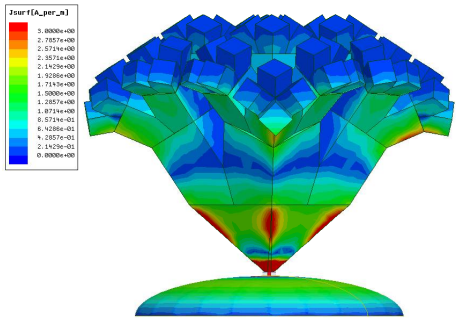

(b) 5.5 GHz

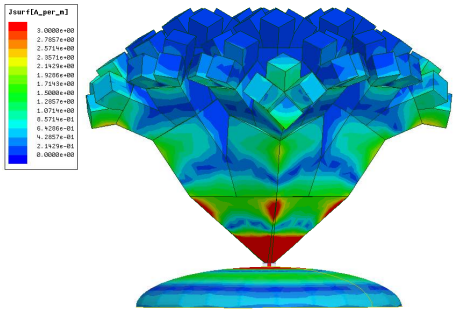

(c) 10 GHz

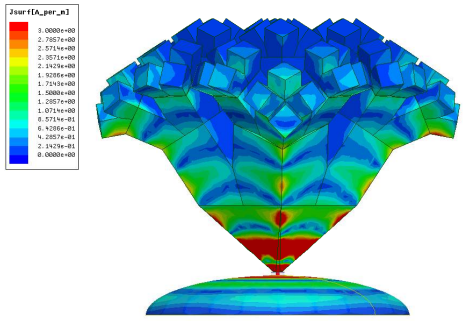

(d) 15 GHz

Figure 5.9: Surface currents on the cubic three-iteration fractal tree antenna at four representative frequencies

case. As shown, the current stays mostly on the outside of the fractal iterations. The inner branches see only minimal current. Also noteworthy is that at higher frequencies, the corners of the structure see much higher concentration of current than the flat sides. This is probably a significant contributing factor in the poor polarization seen at those frequencies. Because of its very poor polarization, this antenna design was abandoned in favor of a less angular design, which is presented in the next section.

5.3 Geometry of Conical Fractal Tree Monopole Antenna

The cube-based fractal antenna presented in the preceding section was shown to have very poor polarization at high frequencies, which seemed to correspond to high concentration of current on the corners of the structure. To counter this problem, a cone-based fractal tree was proposed. This structure almost eliminates the sharp

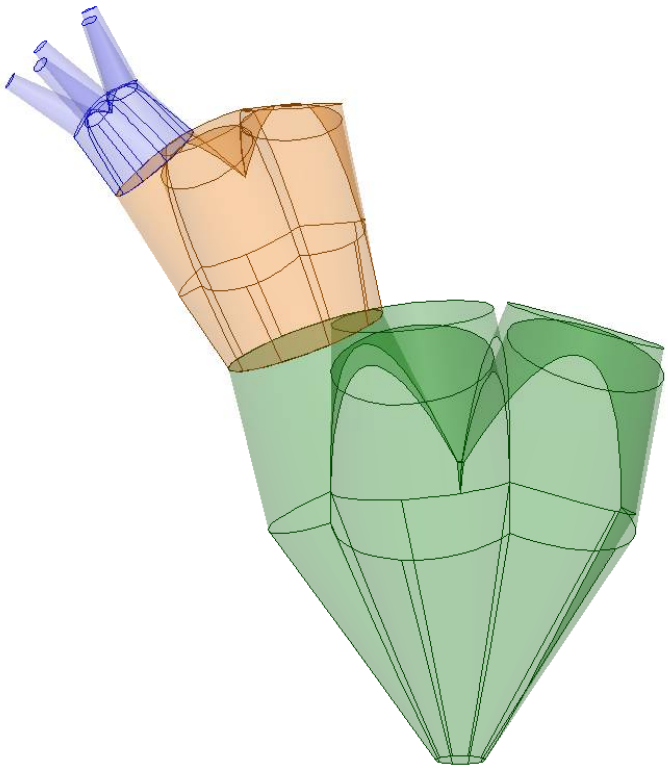

Figure 5.10: Three fractal iterations of the conical fractal tree monopole antenna.

Table 5.3: Dimensions of conical fractal tree monopole antenna

Iteration #	rl (mm)	ru (mm)	h_c (mm)	h_r (mm)
0	NA	1.475	NA	NA
1	7	4.9	10	17
2	4	3.02	7	7
3	1	0.5	5	5

edges, instead transitioning smoothly from one branch to another. The conical fractal monopole antenna presented in this chapter consists of three iterations of progressively smaller alternating conical and interconnecting sections in a branching pattern, as shown in Fig. 5.10. Each branch is formed of a cone with height h_c, lower radius rl_n, and upper radius ru_n, and a circular tapering transition with height h_r, lower radius ru_{n-1} and upper radius rl_n, where n is the iteration number. The vertical axis of each iteration is offset from the axis of the previous iteration by $\alpha = 20°$. Figure 5.11 shows a single branch of the iterative shape. The cone is the upper half of the branch, and the transition section is the lower half. It should be noted that the transition

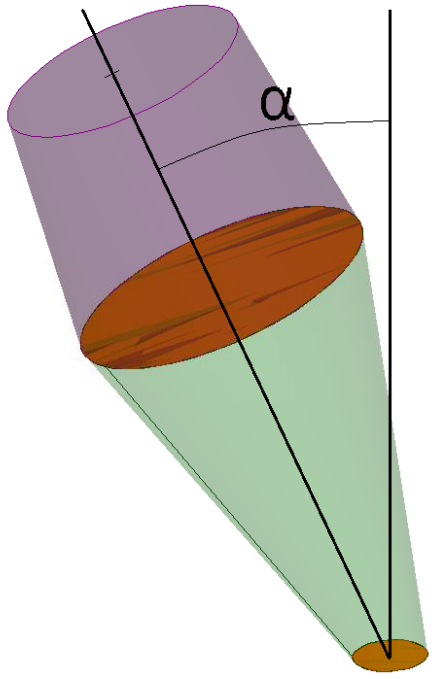

Figure 5.11: The initiator of the conical fractal tree monopole antenna.

Figure 5.12: A wire monopole antenna, for comparison.

section is formed as a connection between the two circles at its ends. The lower circle is normal to the axis of iteration $n-1$, and the upper circle is normal to the axis of iteration n. Since the circles are not parallel, this section is not a cone. Each progressive iteration is built on the previous by using the upper tip of the n^{th} cone as the lower circle of the $(n+1)^{th}$ transition section. The dimensions of the conical fractal tree monopole antenna shown in Fig 5.12 are given in Table 5.3.

An N-pronged structure is formed by duplicating each iteration around the axis of the previous iteration N times, at intervals of $\frac{360^\circ}{N}$. The antenna is matched to an RG-58C/U 50Ω coaxial line using a hemisphere of an oblate spheroidal shaped ground, having a major axis of 25 mm and a minor axis of 15 mm. There is a gap between the ground and the fractal of 0.8 mm. A wire monopole antenna with the same ground as the fractal, having a length of 51 mm and a radius of 0.419 mm, was used for comparison. This antenna is shown in Fig. 5.12.

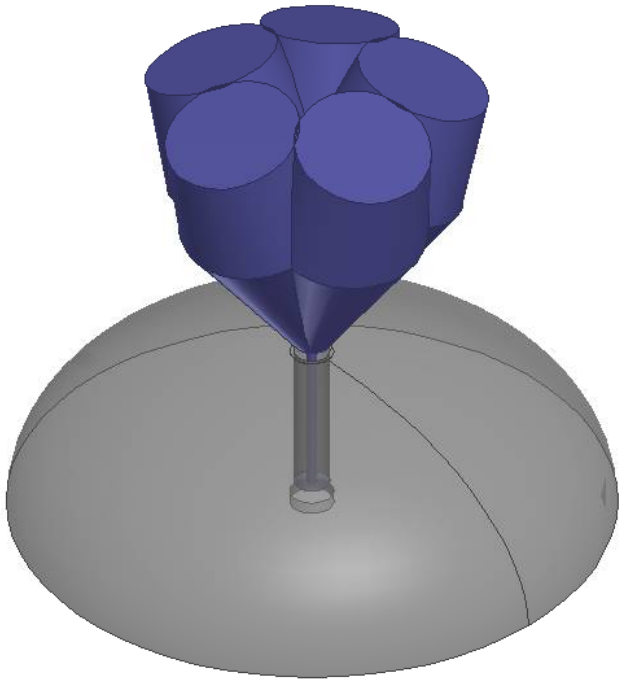

Figure 5.13: A five-pronged fractal tree monopole antenna with a single fractal iteration.

5.4 Simulation of Conical Fractal Tree Monopole Antenna

This section will present several antennas with similar geometries, evaluating each with respect to return loss and radiation pattern. One of these antennas will be chosen for fabrication and measurement in the succeeding section. Two major variations are explored - firstly, the number of fractal iterations, and secondly, the number of duplications around the z-axis, or "prongs". Each of the antennas was simulated in a cylindrical air box with a diameter of 90 mm and a height of 95.8 mm. These dimensions were chosen so that the largest of the antennas was separated from the air box by at least $\lambda/4 = 15$ mm at 5 GHz. There was also a mesh operation defined

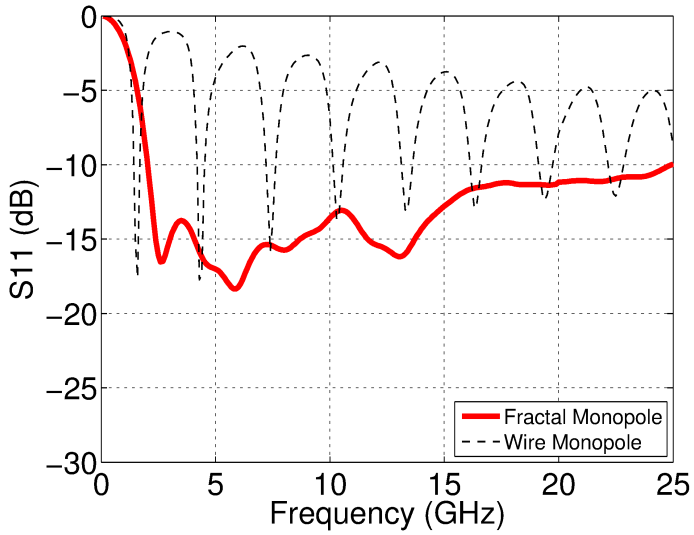

Figure 5.14: The return loss of the five-pronged fractal tree monopole antenna with a single fractal iteration.

on the surface of the air box, which constrained the mesh length on that surface to $\lambda/6 = 5$ mm at 10 GHz. These constraints were required to allow HFSS to perform a near to far field transformation valid from 5 GHz to 10 GHz. It was desireable to minimize the range of frequencies over which the far field simulation was valid, to speed simulation and prevent an unreasonable number of tetrahedra from being required to solve the problem. The consistant size of the air box allows meaningful comparison of the number of tetrahedra used for each simulation, which provides a rough measure of the complexity of the design.

The first antenna to be evaluated is a five-pronged fractal tree monopole antenna with a single fractal iteration, shown in Fig. 5.13. This antenna has an approximate height, not including the ground, of 28 mm, and an approximate radius, not including the ground, of 15 mm. The antenna was simulated in Ansys HFSS, using a mesh of 69,312 tetrahedra, and a convergence criteria of $|\Delta S| < 0.01$ for two consecutive adaptive passes. The return loss for the antenna resulting from this simulation is shown in Fig. 5.14 in solid red, as well as the return loss for the wire monopole antenna shown in Fig. 5.12 in dashed black, for comparison. The radiation pattern

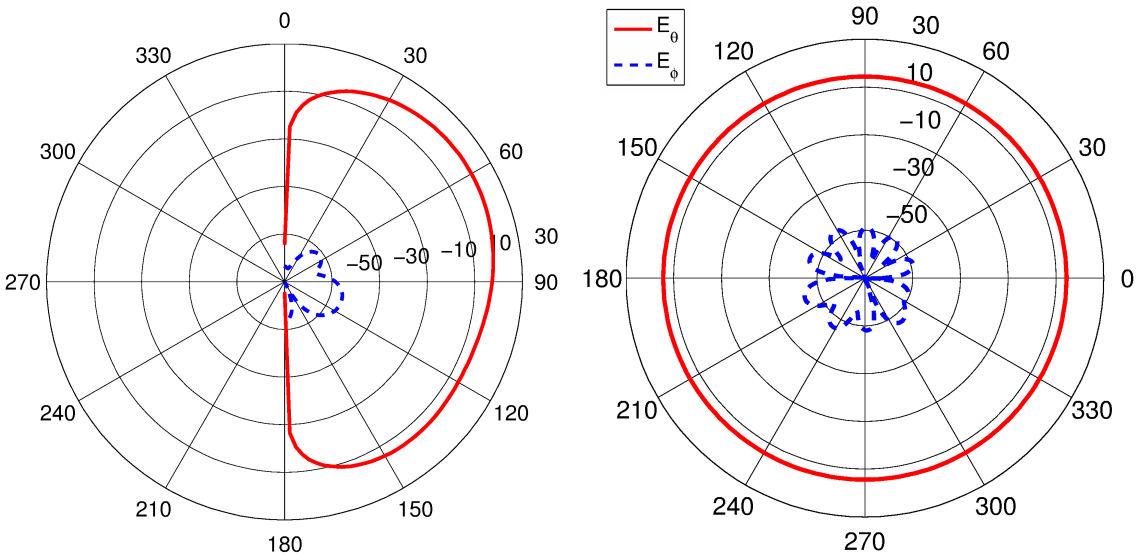

(a) E-plane radiation, $\phi = 160°$ (b) H-plane radiation, $\theta = 120°$

Figure 5.15: Radiation pattern for single-iteration fractal antenna at 5.5 GHz.

and cross-polarization in dB of the single-iteration fractal tree monopole antenna at 5.5 GHz is shown in Fig. 5.15.

The five-pronged, single-iteration antenna is shown to have return loss less than -10 dB from 2 GHz to 24.9 GHz, corresponding to a bandwidth of 170.3%. The radiation pattern in dB at a representative frequency of 5.5 GHz closely resembles that of a wire monopole, with very high symmetry about the z-axis, very smooth E-plane pattern with respect to θ, and cross-polarization better than 46 dB, except at the extremes of $\theta = 0°$ and $\theta = 90°$.

The second antenna is shown in Fig. 5.16. This is a five-pronged fractal tree monopole antenna with two fractal iterations. This antenna has an approximate height, not including the ground, of 40 mm, and an approximate radius, not including the ground, of 21 mm. The simulation converged using 90,057 tetrahedra, with $|\Delta S| < 0.01$ for two consecutive passes. Figure 5.17 shows the return loss of this antenna in dB, and Fig. 5.18 shows its radiation pattern and cross-polarization at 5.5 GHz.

As shown, the five-pronged, two-iteration fractal antenna has return loss better than -10 dB starting at approximately 1.43 GHz and continuing to 24.9 GHz. This

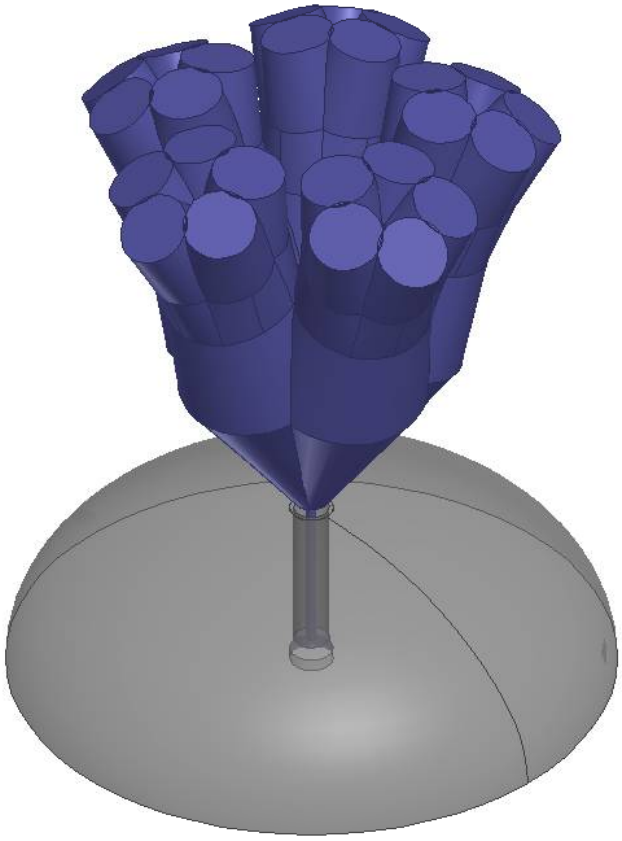

Figure 5.16: A five-pronged fractal tree monopole antenna with two fractal iterations.

corresponds to a bandwidth of 178.3%. This antenna also has a radiation pattern that is symmetric about the z-axis, and displays cross-polarization only slightly worse than the single-iteration model. Cross-polarization for this antenna is better than 34 dB except at the extremes of $\theta = 0°$ and $\theta = 180°$. The E-plane radiation maintains the smoothness with respect to θ of the previous model.

Thirdly, a three-iteration model was simulated. This antenna, shown in Fig. 5.19, has a height of approximately 51 mm, not including the ground, and a radius of approximately 27 mm. The simulation converged with 210,702 tetrahedra, after two consecutive passes with $|\Delta S| < 0.01$. This simulation results in the return loss shown in Fig. 5.20. The radiation pattern and cross-polarization at 5.5 GHz is shown in

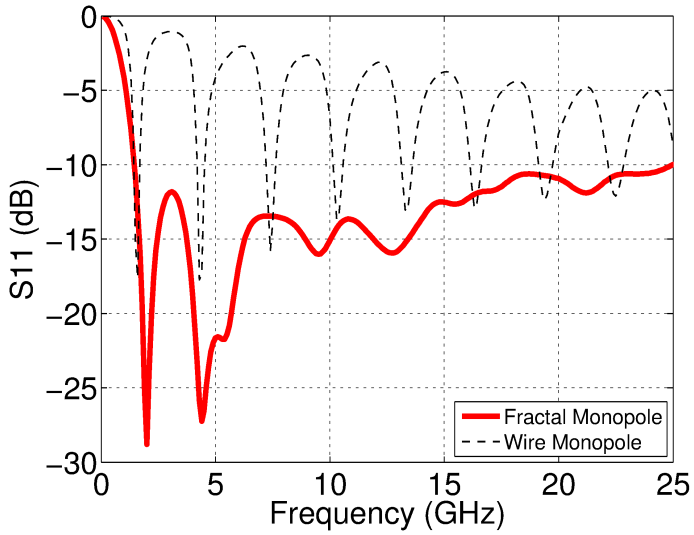

Figure 5.17: The return loss of the five-pronged fractal tree monopole antenna with two fractal iterations.

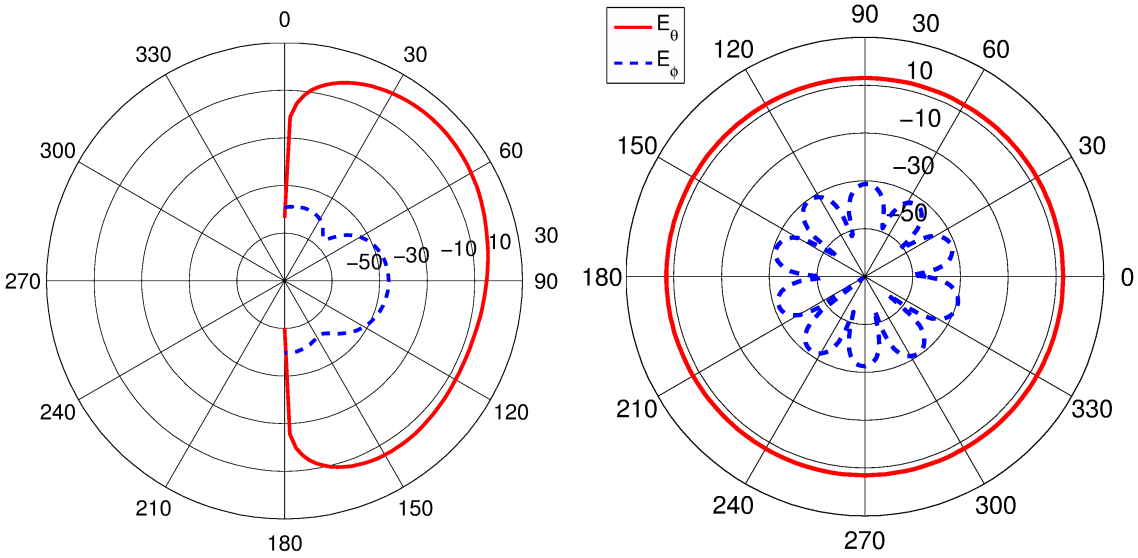

(a) E-plane radiation, $\phi = 160°$ (b) H-plane radiation, $\theta = 120°$

Figure 5.18: Radiation pattern for two-iteration fractal antenna at 5.5 GHz.

Fig. 5.21.

The five-pronged, three-iteration fractal tree monopole antenna is shown to have return loss less than -10 over the range 1.22 GHz–24.1 GHz, corresponding to a bandwidth of 180.7%. Its radiation pattern maintains symmetry with respect to ϕ, but the smoothness of the E-plane pattern with respect to θ is slightly degraded in compar-

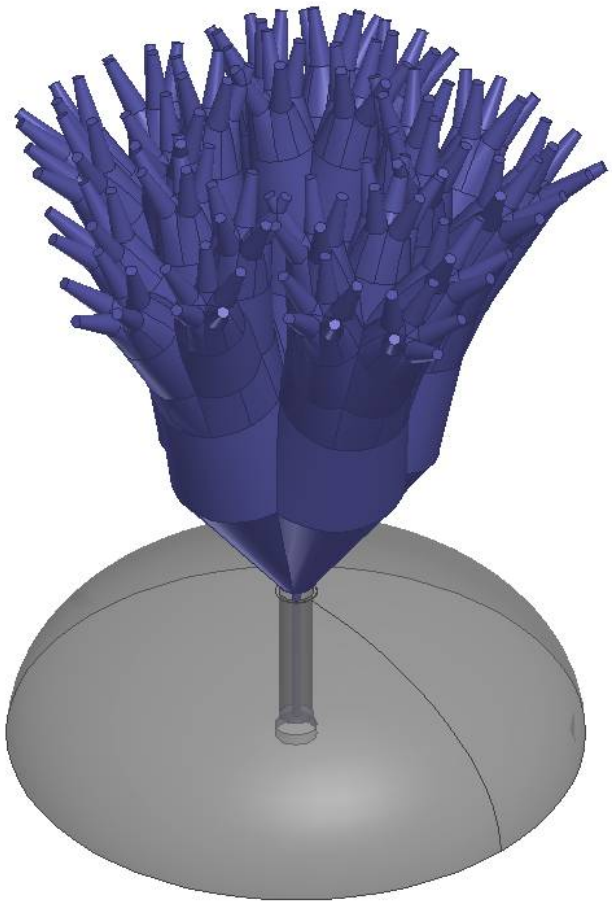

Figure 5.19: A five-pronged fractal tree monopole antenna with three fractal iterations.

ison to the previous two models. At 5.5 GHz, the cross-polarization of this antenna is better than 21 dB (except at the extremes of $\theta = 0°$ and $\theta = 90°$. Because of the resolution limitations of the 3D printer used for fabrication, further increase of the number of iterations was not feasible. Table 5.4 summarizes the results of these three simulations, for easy comparison. As shown, the bandwidth increases by 9% from the single-iteration model to the two-iteration model, but only increases by 4% from the two-iteration model to the three-iteration model. The cross-polarization degrades by 12 dB from the single-iteration model to the two-iteration model, and degrades by a further 13 dB from the two-iteration model to the three-iteration model. Assuming this trend holds, a fourth iteration would increase the bandwidth only marginally,

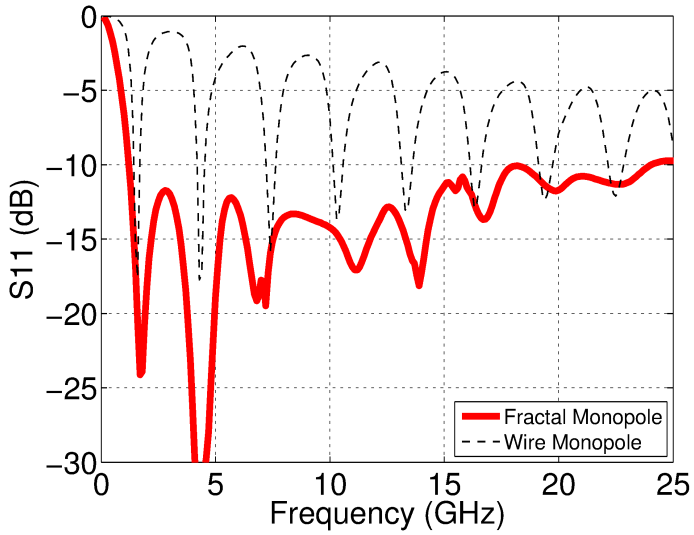

Figure 5.20: The return loss of the five-pronged fractal tree monopole antenna with three fractal iterations.

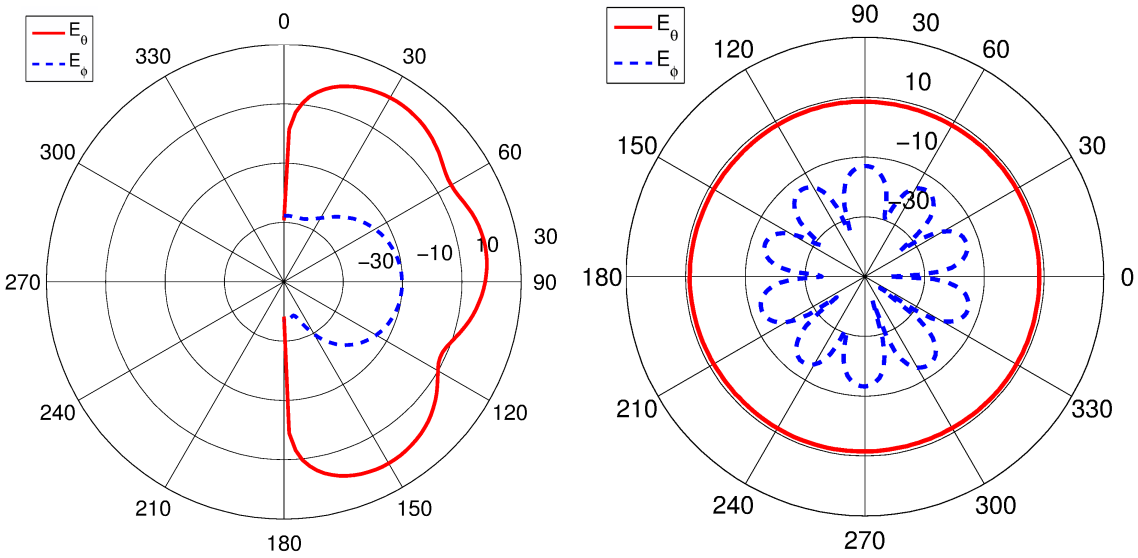

(a) E-plane radiation, $\phi = 90°$ (b) H-plane radiation, $\theta = 116°$

Figure 5.21: Radiation pattern for five-pronged fractal antenna at 5.5 GHz.

while the cross-polarization would become significantly worse. Of the three models that were simulated, the three-iteration model has the highest bandwidth, while also maintaining good cross polarization.

Table 5.4: Summary of simulation results for one- two- and three-iteration fractal tree monopole antennas

# of Iterations	Height (mm)	Radius (mm)	Bandwidth (%)	Cross-polarization (dB)	# of Tetrahedra
1	28	15	170.3	46	69,312
2	40	21	178.3	34	90,057
3	51	27	180.7	21	210,702

5.5 Variations of Conical Fractal Tree Monopole Antenna

All three of the antennas simulated thus far were five-pronged antennas. The effect of changing the number of prongs on the antenna is investigated next. Three-pronged, four-pronged, five-pronged, and six-pronged fractal monopole antennas are shown in Fig. 5.22.

Each of these antennas has an overall height, not including the ground, of approximately 51 mm, and a maximum radius of 27 mm. They were each simulated in Ansys HFSS, using a convergence criteria of $|\Delta S| < 0.01$ for two consecutive passes. The magnitude of S_{11} in dB resulting from these simulations is shown in Fig. 5.23 for each permutation in solid red. The S_{11} of the wire monopole antenna shown in 5.12 is shown in dashed black for comparison.

The three-pronged fractal antenna converged with 128,303 tetrahedra. This antenna is shown to have S_{11} below -10 dB from approximately 1.26 GHz to 18 GHz, corresponding to a bandwidth of 173.0%. The four-pronged fractal antenna, which converged with 153,518 tetrahedra, has better bandwidth than the three-pronged version; S_{11} is shown to be -10 dB from approximately 1.23 GHz to 24 GHz, corresponding to a bandwidth of 180.5%. The five-pronged fractal, which was discussed previously, has only slightly larger bandwidth than the four-pronged version; S_{11} is below -10 dB from approximately 1.22 GHz to 24.1 GHz, corresponding to a bandwidth of 180.7%. The six-pronged fractal, which converged with 332,737 tetrahedra, has a lower bandwidth than the five-pronged fractal. Its S_{11} is below -10 dB only from 1.2 GHz to

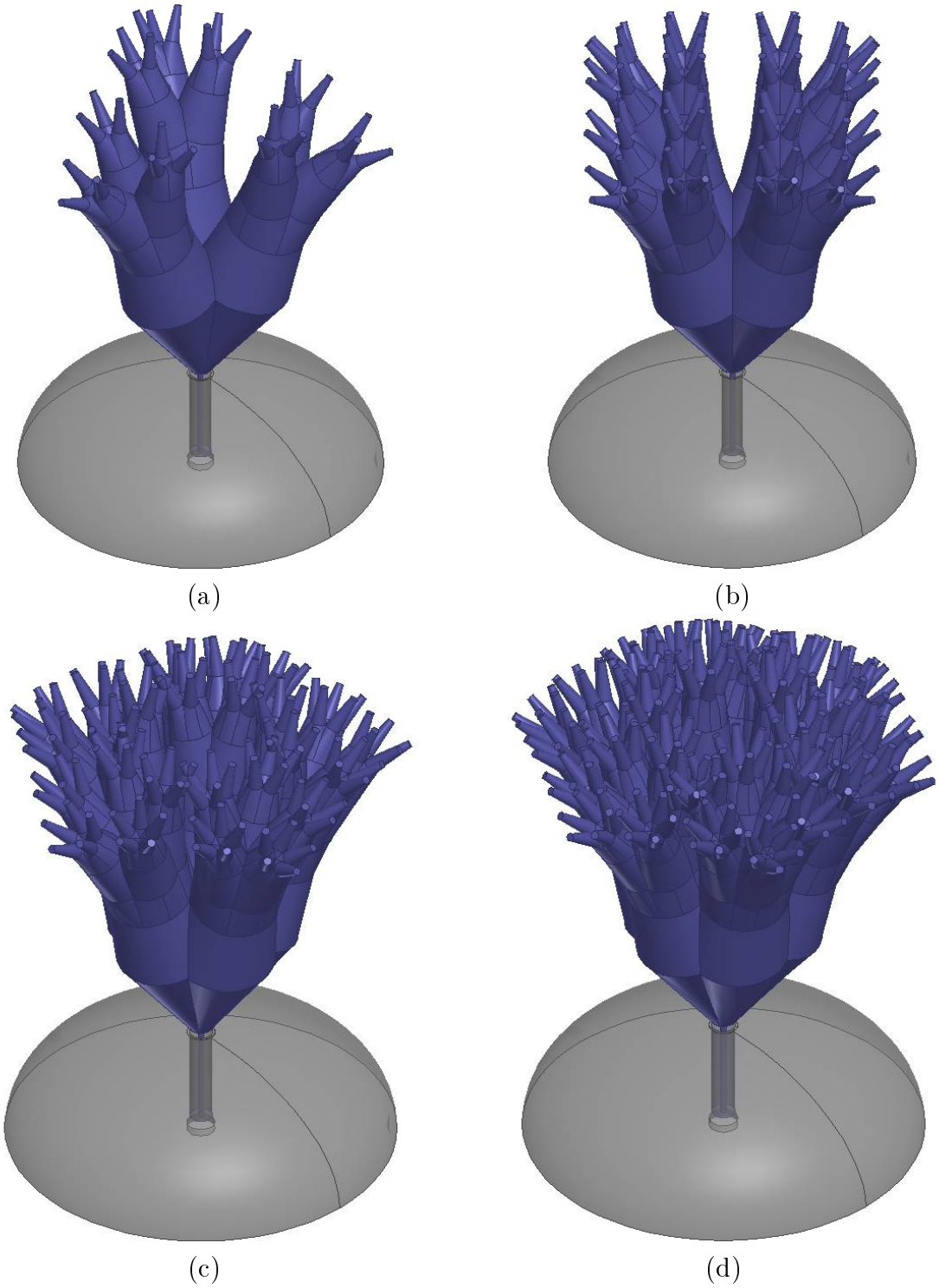

(a) (b)

(c) (d)

Figure 5.22: (a) Three-pronged fractal tree antenna. (b) Four-pronged fractal tree antenna. (c) Five-pronged fractal tree antenna. (d) Six-pronged fractal tree antenna.

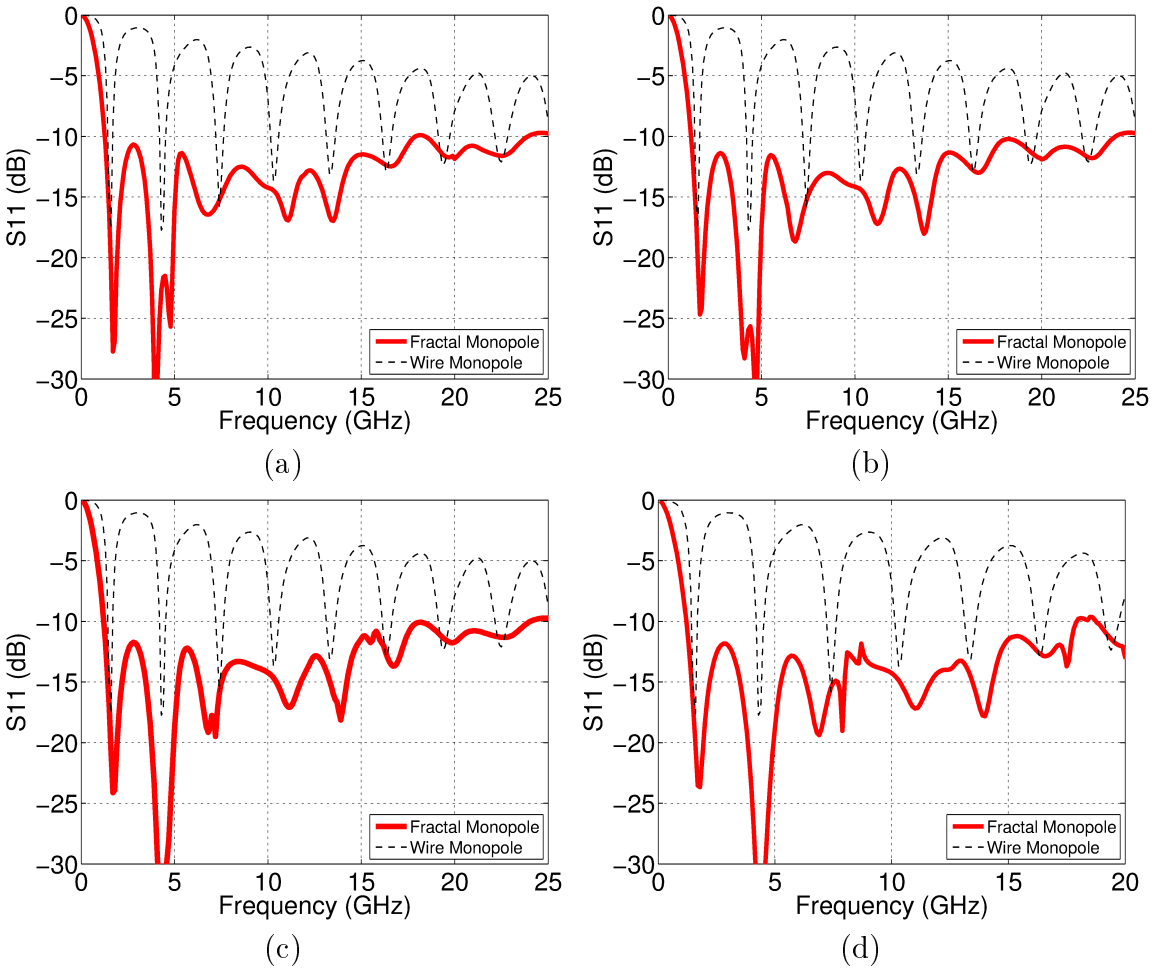

Figure 5.23: (a) Return loss in dB for the three-pronged fractal tree antenna. (b) Return loss in dB for the four-pronged fractal tree antenna. (c) Return loss in dB for the five-pronged fractal tree antenna. (d) Return loss in dB for the six-pronged fractal tree antenna.

17.9 GHz, corresponding to a bandwidth of 174.9%.

The radiation pattern for the three-pronged antenna at a representative frequency of 5.5 GHz is shown in Fig. 5.24. The cross-polarization of this antenna is very poor, as shown. At ($\theta = 109°$, $\phi = 90°$), the cross-polarized power is only 0.54 dB less than the co-polarized power. Also, the radiation is notably asymmetric with respect to ϕ, with minima at approximately $\phi = 0°$, $\phi = 120°$, and $\phi = 240°$, corresponding to the angles of the three prongs. The radiation maxima occur at approximately $\phi = 60°$, $\phi = 180°$, and $\phi = 300°$, corresponding to the angles of the valleys between the prongs. It is also interesting to note that the cross-polarization has six lobes, with

the minima at $\phi = 0°$ and at 60° intervals all the way around, corresponding to both the prongs and valleys.

The radiation pattern for the four-pronged antenna is shown in Fig. 5.25. This antenna has only slightly better polarization characteristics than the three-pronged case. At ($\phi = 90°$, $\theta = 112°$), the cross-polarized radiation is only 7.19 dB below the co-polarized radiation. Again, the radiation pattern is noticeably asymmetric, with maxima at $\phi = 0°$, $\phi = 90°$, $\phi = 180°$, and $\phi = 270°$, at the angles of the prongs, and minima at $\phi = 45°$, $\phi = 135°$, $\phi = 225°$, and $\phi = 315°$, at the angles of the valleys. The cross-polarization has eight distinct lobes, with minima at $\phi = 0°$ and at 45° intervals all the way around, corresponding to both the prongs and the valleys.

The radiation pattern for the five-pronged antenna at 5.5 GHz is shown previously, in Fig. 5.21. The five-pronged antenna shows a much better radiation pattern than either of the previous two variations, with cross-polarization better than 21 dB (excluding the extremes of $\theta = 0°$ and $\theta = 180°$). The radiation appears to be symmetric with respect to ϕ. Following the trend of the previous two simulations, the cross-polarization has ten distinct lobes, with minima at $\phi = 0°$ and at 36° intervals all the way around, corresponding to both the prongs and the valleys.

Finally, the radiation pattern for the six-pronged antenna at 5.5 GHz is shown in Fig. 5.26. This antenna has the best polarization of the four, with cross-polarization better than 31 dB (excluding at the extremes). The radiation appears to be symmetric with respect to ϕ, and the cross-polarization has twelve lobes, with minima at $\phi = 0°$ and at 30° intervals, corresponding to the prongs and valleys.

Table 5.5 summarizes the simulation results for the three-pronged, four-pronged, five-pronged, and six-pronged three-iteration fractal tree antennas.

Since the five-pronged fractal has the best bandwidth and the second-best polarization of these four simulated antennas, it was selected to be fabricated and tested. However, we will first look at the simulation in more detail. Two more simulations

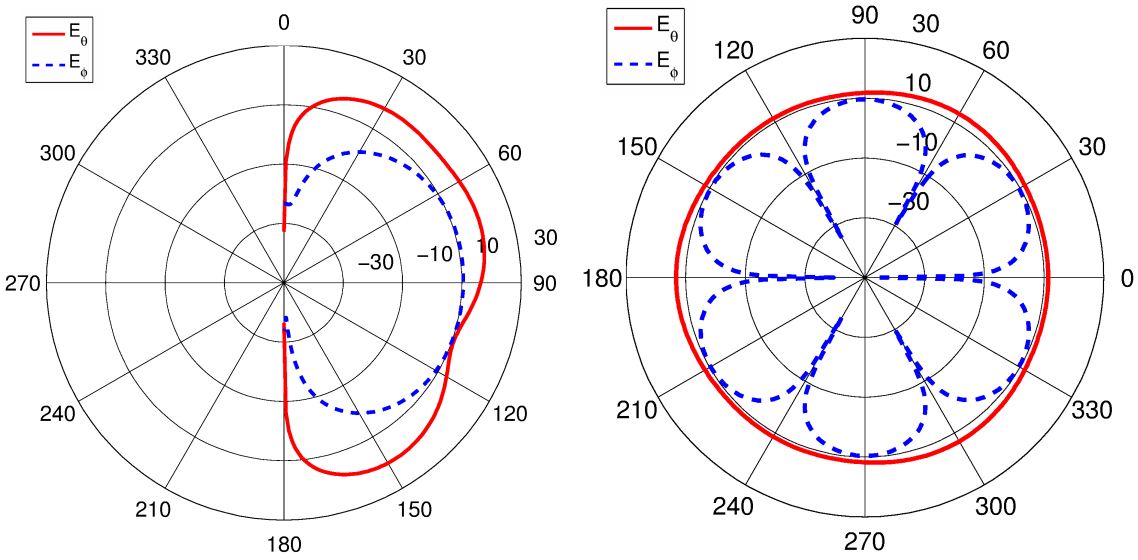

(a) E-plane radiation, $\phi = 60°$ (b) H-plane radiation, $\theta = 116°$

Figure 5.24: Radiation pattern for three-pronged fractal antenna at 5.5 GHz.

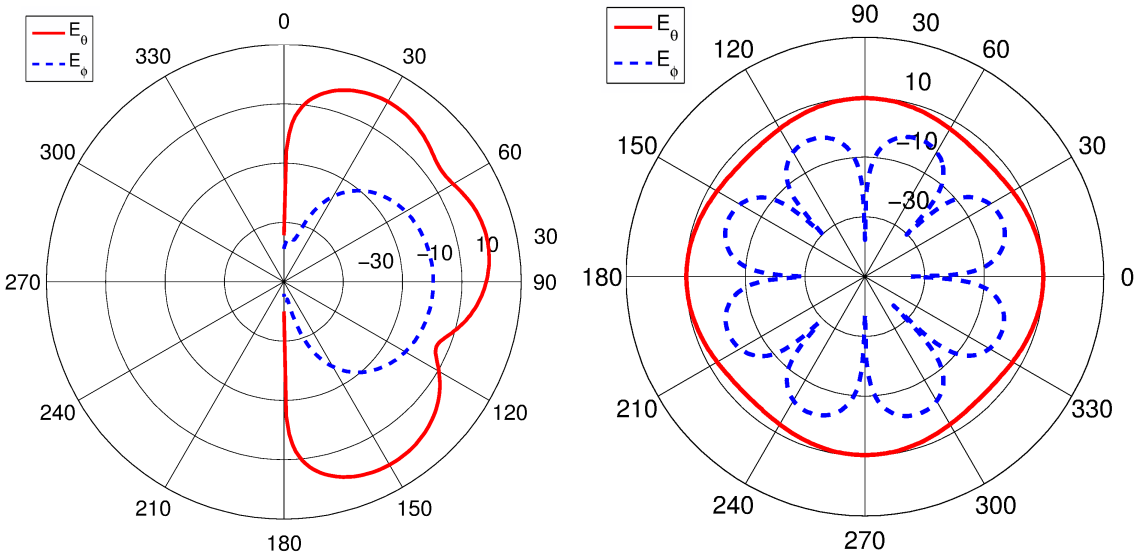

(a) E-plane radiation, $\phi = 90°$ (b) H-plane radiation, $\theta = 116°$

Figure 5.25: Radiation pattern for four-pronged fractal antenna at 5.5 GHz.

were performed in HFSS to obtain far field results valid from 1 GHz to 5 GHz, and from 10 GHz to 20 GHz. Figure 5.27 shows the E-plane radiation pattern of the five-pronged, three-iteration fractal tree monopole antenna at 1.3 GHz, 10 GHz, 15 GHz, and 20 GHz, and Fig. 5.28 shows the H-plane radiation pattern at the same frequencies.

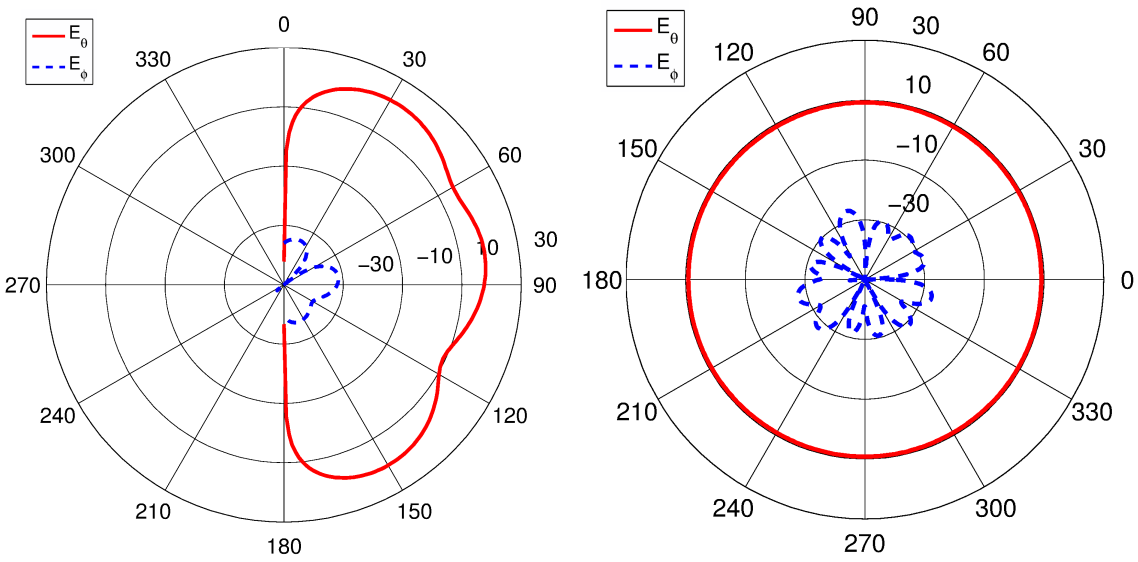

(a) E-plane radiation, $\phi = 90°$ (b) H-plane radiation, $\theta = 116°$

Figure 5.26: Radiation pattern for six-pronged fractal antenna at 5.5 GHz.

These graphs clearly show that the polarization gets better as the frequency decreases. The polarization at 1.3 GHz is better than 46 dB, excluding the extremes of $\theta = 0°$ and $\theta = 90°$. The polarization at 10 GHz is better than 24 dB, excluding the extremes. The polarization at 15 GHz is much worse, with co-polarized power actually 0.29 dB less than cross-polarized power at approximately $\theta = 130°$, $\phi = 90°$. The cross-polarization at 20 GHz is only 0.63 dB below the co-polarized power at $\theta = 156°$, $\phi = 90°$.

Figure 5.29 shows the magnitude of the surface currents on the antenna at 1.3 GHz, 5.5 GHz, 15 GHz, and 20 GHz. The range from blue to red is 0 A/m–3 A/m in every

Table 5.5: Summary of simulation results for three-pronged, four-pronged, five-pronged, and six-pronged fractal tree monopole antennas

# of Prongs	Height (mm)	Radius (mm)	Band-width (%)	Cross-polarization (dB)	# of Tetrahedra
3	51	27	173.0	0.54	128,303
4	51	27	180.5	7.19	153,518
5	51	27	180.7	21	210,702
6	51	27	174.9	31	332,737

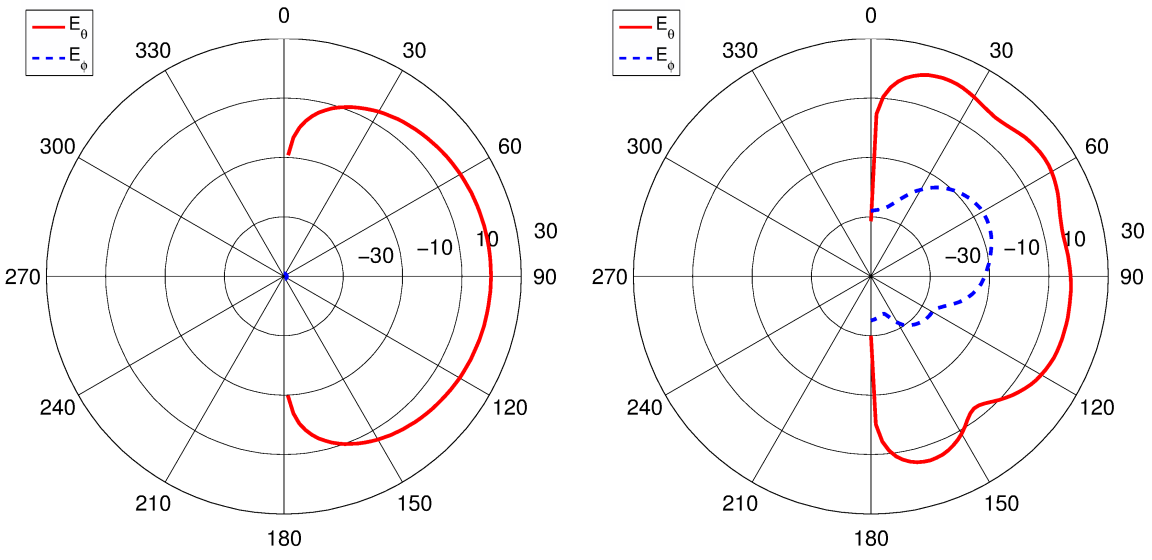

(a) $\phi = 90°$ (b) $\phi = 90°$

(c) $\phi = 90°$ (d) $\phi = 90°$

Figure 5.27: E-plane radiation pattern for five-pronged three-iteration fractal tree antenna at (a) 1.3 GHz. (b) 10 GHz. (c) 15 GHz. (d) 20 GHz.

case. As shown, the center of the structure does not carry much current at any of the four investigated frequencies. Figure 5.29 (a) shows the currents at 1.3 GHz, where the current is almost entirely on the outside surface of the structure, with some current on the upper branches of the tree at approximately 1 A/m. High-density current reaches halfway up the arms of the fractal, as it does in none of the other three figures. Figure 5.29 (b) shows the currents at 5.5 GHz, where higher current densities are seen in

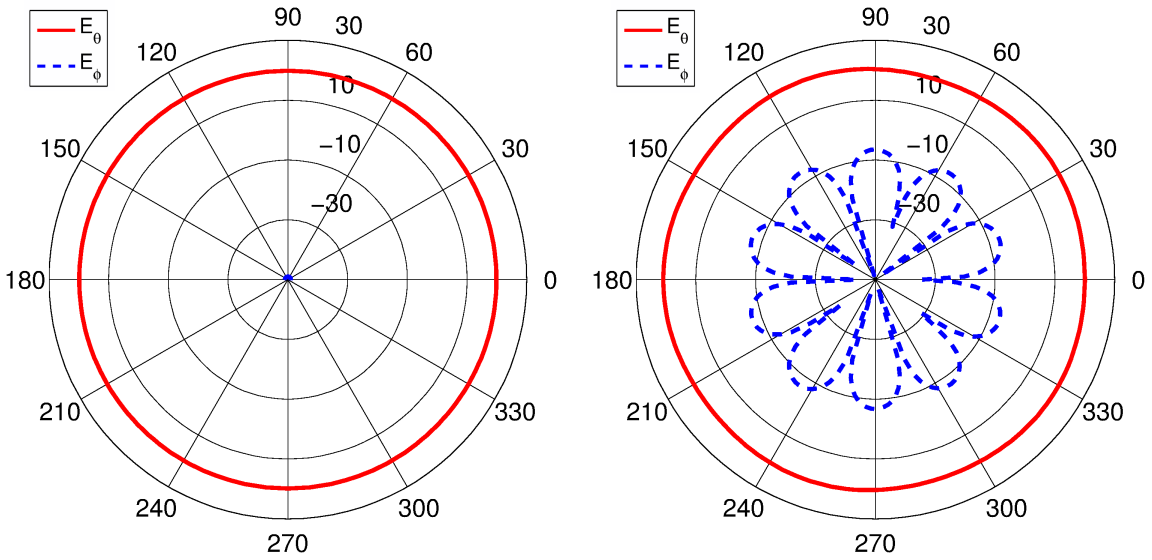

(a) $\theta = 90°$ (b) $\theta = 60°$

(c) $\theta = 116°$ (d) $\theta = 60°$

Figure 5.28: H-plane radiation pattern for five-pronged three-iteration fractal tree antenna at (a) 1.3 GHz. (b) 10 GHz. (c) 15 GHz. (d) 20 GHz.

the upper branches of the fractal tree, reaching 3 A/m in the valleys between the second-iteration branches. The high current densities in the upper branches are also visible in Fig. 5.29 (c), at 15 GHz, but in this case they are located in the valleys between the third-iteration branches. Figure 5.29 (d), shows that the currents at 20 GHz are concentrated most highly at the base of the figure, on the lower half of the first iteration.

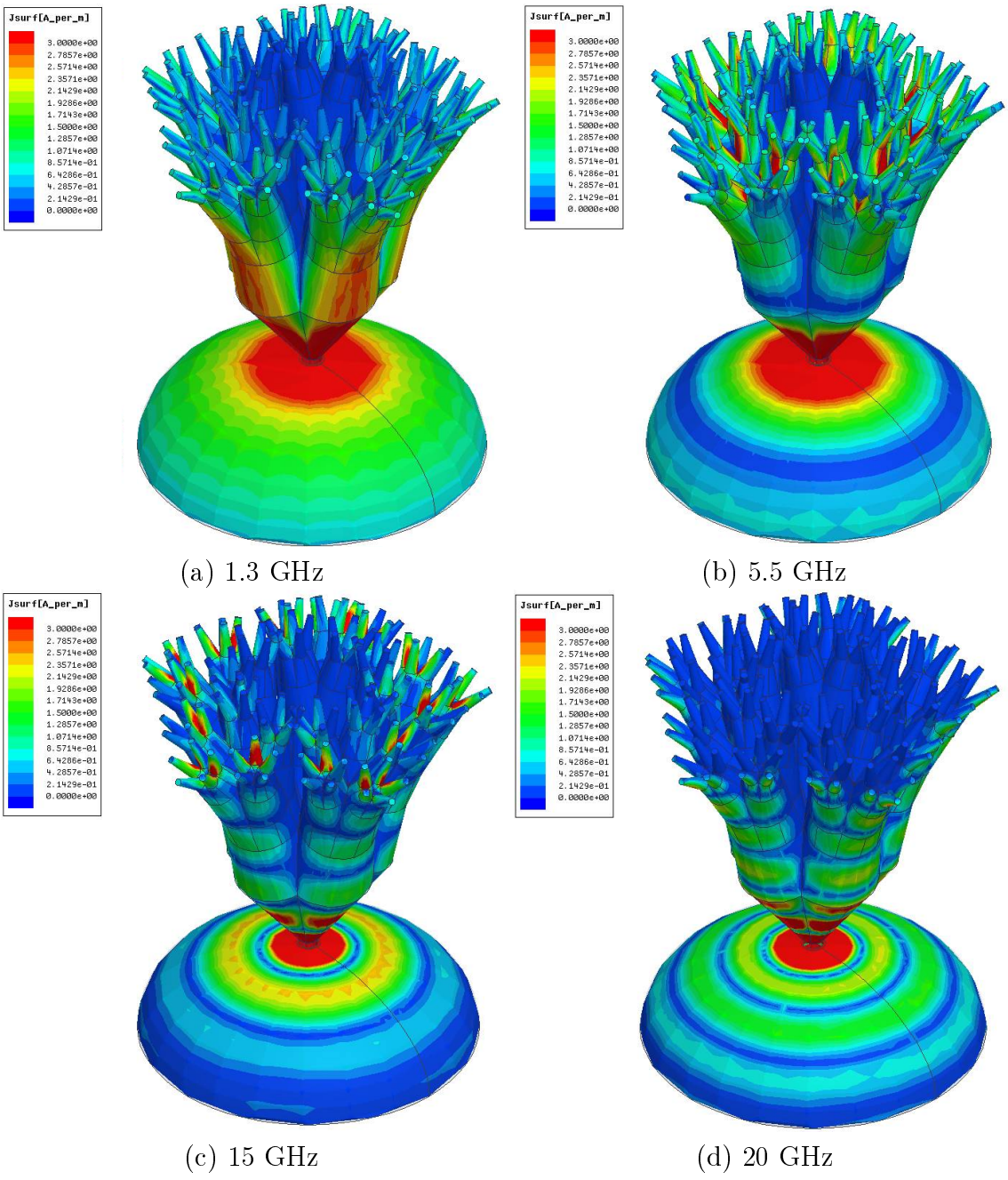

(a) 1.3 GHz (b) 5.5 GHz

(c) 15 GHz (d) 20 GHz

Figure 5.29: Surface currents on the antenna at four representative frequencies

5.6 Fabrication and Measurement of Conical Fractal Tree Monopole Antenna

The 3D printer requires any model it prints to have a qualitatively large base, otherwise the print will not adhere to the build plate. It also requires that the model only have minimal spreading with each progressive layer, or the print will become stringy and ill-defined. To facilitate high-quality printing, therefore, the body of the

fractal tree was split into two pieces. The upper half of the fractal was printed from bottom to top, and the lower half was printed from top to bottom. The ground was naturally large at the base, and tapered with each layer, so it was not adjusted in any way for the print. Figure 5.30 shows the HFSS model used for printing. Since the 3D printer requires Stereo Lithography (.stl) files, and HFSS cannot output this file type, an Standard for the Exchange of Product Data (.step) file was exported from HFSS, imported into AutoCad, and exported from AutoCad as a Stereo Lithography file. This was then loaded into the 3D printer Makerware software. The fractal tree and hemispherical oblate spheroidal ground were then 3D printed of ABS plastic with a MakerBot Replicator 2X, using a layer height of 0.1 mm. The bottom and top halves of the fractal body were glued together with superglue. The antenna form shown in 5.31 (a) resulted.

This form was spray painted with several layers of an acrylic-based conductive paint from M. G. Chemicals. The conductivity of this spray paint was measured

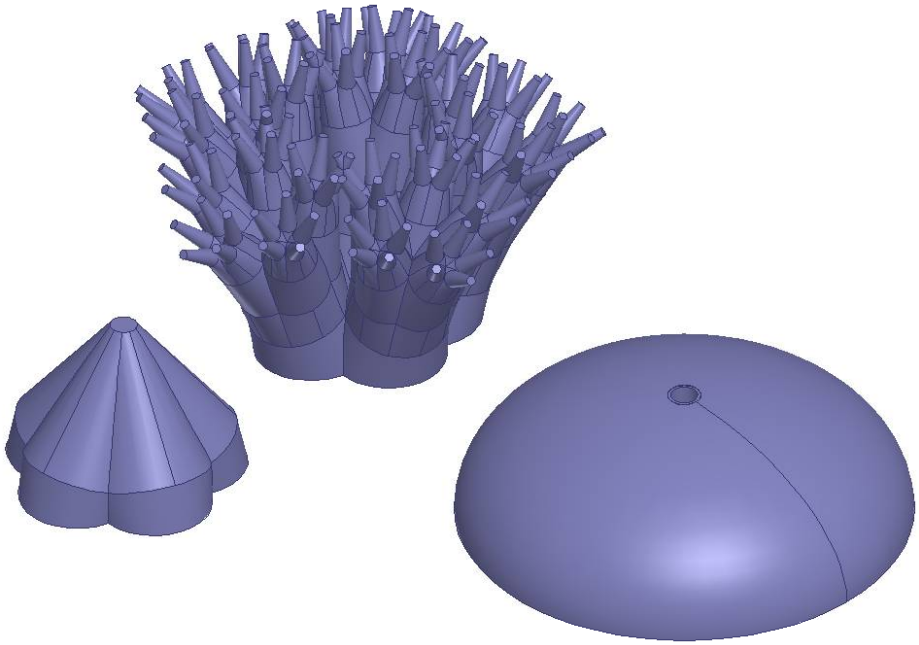

Figure 5.30: 3D printed pieces of fractal monopole antenna.

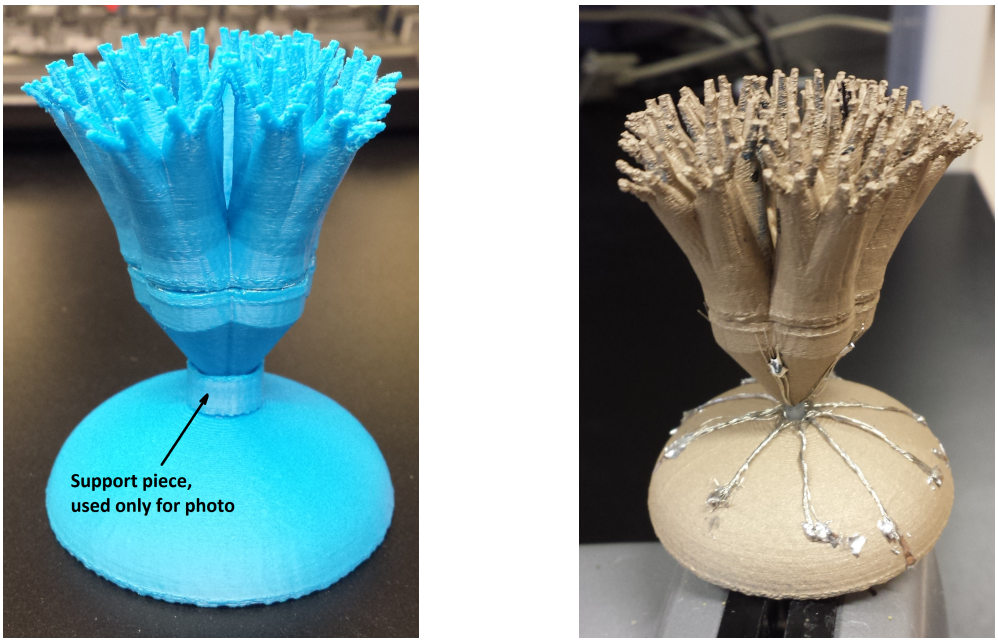

(a) (b)

Figure 5.31: (a) 3D-printed form of the five-pronged fractal tree antenna. (b) Final fractal tree antenna.

at 0.6 Ω/square for a thoroughly coated square. The paint-covered form was then connected to an RG-58C/U coaxial cable, as shown in Fig. 5.31 (b). The wires of the outer conductor of the coax were divided into several small bundles and splayed back along the ground. Low-temperature solder was used to very carefully connect each bundle of wires to the painted ground without melting the plastic. Similarly, the wires of the center conductor were divided into five small bundles, and soldered in the valleys between the prongs on the main body of the antenna. The return loss of this antenna was measured using an Anritsu 37297D network analyzer, and is shown in Fig. 5.32. The simulated return loss for the five-pronged, three-iteration fractal tree is also shown, for comparison. This antenna was shown to have less than -10 dB return loss over a range of 1.2 GHz – 25 GHz, which is a bandwidth of 181.7%.

The measured antenna differed from the simulated model in that the indentations between the first-iteration cones were partially filled with wire and solder, and the ground also had wires and solder on its upper surface. Furthermore, the gap between

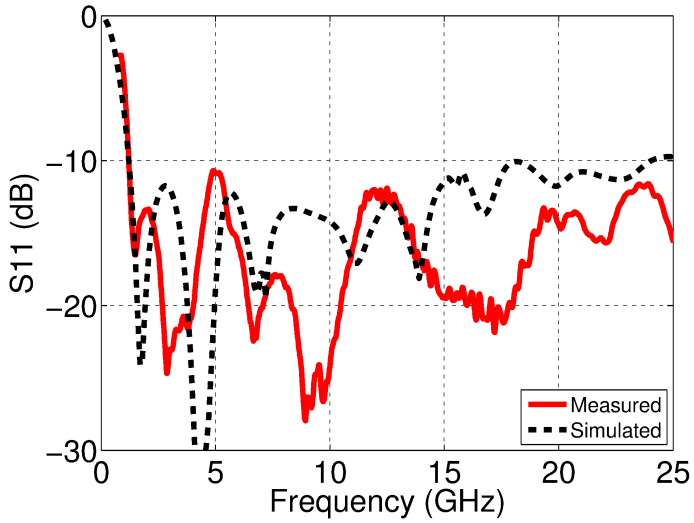

Figure 5.32: Measured return loss for fractal monopole antenna.

the fractal and the ground, which was set at 0.8 mm in the simulations, was much harder to fix in reality, and may have varied from the target value by as much as a millimeter or two. Also, because the fractal body was printed in two pieces, there was a noticeable seam around the circumference of the body, as shown in Fig. 5.31. Finally, in simulation the antenna body and ground were defined as PEC, but in reality they had a finite conductivity that almost certainly varied over the surface, since some areas were extremely difficult to access with the spray paint. Any or all of these variations may have contributed to the difference between simulated and measured results shown in Fig. 5.32.

CHAPTER 6: CONCLUSION

6.1 Summary of Work Presented

This work began by providing an overview of the topics that would be covered, as well as explaining the motivation behind this research. Some background information was provided on metamaterials in general, including the definitions of permeability and permittivity. The four possible combinations of sign for real-valued permeability and permittivity were presented, and the propagation characteristics of each were examined. The special properties of materials having simultaneously negative permeability and permittivity were discussed, and simulation results were shown demonstrating negative phase velocity and the reversal of Snell's law for such materials. The evanescence of waves in a single-negative medium was also shown in simulation. The concept of fractals was introduced, using fern fronds and Romanesco broccoli as naturally-occurring examples.

The narrowband behavior of split ring resonators and capacitively loaded strips near resonance was discussed, as well as the motivation for developing wideband metamaterials. Non-Foster loading was presented as a possible means of achieving wideband performance, since the negative impedance of the non-Foster circuit can be engineered to cancel the intrinsic reactance of the unit cell. The utilization of fractal geometries in the design of new metamaterial unit cells was also discussed, as well as their potential to provide broadband performance when the structures are engineered to resonate at several closely spaced frequencies. Fractal geometries were also discussed in the context of antenna design, since the same property of multiple resonances that makes fractal metamaterials appealing also can be utilized to engineer broadband antennas.

A new coaxial fixture in which metamaterials could be tested was discussed, and four control samples were first simulated in HFSS then measured in the fixture, to ensure continuity of simulated and measured results. The detailed dimensions for the 3D printed pieces of the test fixture are given in Appendix A. Two methods for extracting relative permeability and permittivity from measured S-parameters were discussed and compared, and the results of each were shown for two of the four control measurements, to demonstrate that both methods returned the same results.

A capacitively loaded strip unit cell loaded with a non-Foster negative inductor was presented next. The effects of parasitic resistance in the non-Foster load were discussed mathematically, and calculated and simulated results for ideal and realistic loads in parallel plate waveguides were presented. The CLS with a realistic non-Foster load in the coaxial test fixture was first simulated in HFSS, then simulated in ADS using the S-parameters from HFSS. Finally, it was measured in the coaxial fixture, and extracted permeability and permittivity obtained from that measurement were presented. Tunability of the extracted permittivity was demonstrated in both simulation and measurement by varying the value of the negative capacitance load. This structure demonstrated sub-unity permittivity in measurement over a bandwidth of 133%, for a parallel resistance of approximately 220 kΩ and a series resistance of approximately -133 Ω.

Next, a split ring resonator unit cell loaded with a non-Foster negative capacitor was presented. The effects of parasitic resistance in the non-Foster load were discussed mathematically, and calculated and simulated results for ideal and non-ideal loads in parallel plate waveguides were presented. The SRR with a realistic non-Foster load in the coaxial fixture was simulated in HFSS, and shown to demonstrate negative permeability over a bandwidth of 100% for a parallel parasitic resistance of 2 kΩ and a series parasitic resistance of -0.5 Ω. Tunability of permeability was demonstrated in simulation by varying the value of the negative inductance load.

A fractal metamaterial unit cell that demonstrated wideband negative permittivity was presented next. The structure also demonstrated negative permeability, but at a frequency where the unit cell was not electrically small. This unit cell was simulated in a parallel plate waveguide in HFSS, and the currents on the structure and fields in the guide were presented at each resonant frequency. A test fixture similar to that used to measure the fractal unit cell was presented, and the differences between parallel plate and coaxial waveguides were discussed in detail. A set of three unit cells was simulated and measured in the coaxial test fixture, and extracted results were presented and compared. This structure was shown to have negative permittivity over approximately a 32.9% bandwidth. An interlocking grid structure was simulated in both a parallel plate and rectangular waveguide, and the differences between these two measurement structures were discussed at length. The measured results for the interlocking grid in a rectangular waveguide were presented. This structure was shown to provide negative permittivity over approximately a 17.1% bandwidth.

Finally, two fractal tree monopole antennas were presented. The first was formed of cubic fractal iterations, and was found to have broadband performance but highly asymmetric radiation at high frequencies, as well as poor cross-polarization. A second design was presented, formed of conical fractal iteration. This structure was explored in more detail than the previous, with a comparison of several simulated variations of the structure. The five-pronged version with three fractal iterations was selected to be fabricated, and measured return loss is presented. This antenna was shown in measurement to have return loss better than -10 dB over a bandwidth of 181.7%.

6.2 Future Work

The non-Foster metamaterials research will be continued through development of a stable non-Foster negative capacitor to match the SRR simulations, and measurement of wideband negative permeability. A unit cell integrating both the CLS and the SRR will be developed, and the load impedances will be adjusted for the new configura-

tion. This should result in measureable wideband negative index of refraction at low frequencies. The bandwidth of both the CLS and the SRR were shown to depend strongly on the values of the parallel and series parasitic resistances. Therefore, it will be appropriate to make a concentrated effort to reduce these effects.

The fractal metamaterials research will be expanded by applying similar fractal methods to a split ring resonator, in an attempt to develop a structure that provides negative permeability over the same frequencies over which the existing unit cell provides negative permittivity. Three-dimensional fractal metamaterials will also be explored, to minimize the anisotropy of the unit cell.

The radiation pattern of the fractal antenna will be measured, to confirm agreement with simulation. If the limited conductivity of the antenna surface is shown to result in degraded radiation characteristics, the antenna form can be 3D printed in metal by an outside party, such as Shapeways.

REFERENCES

[1] D. Gregoire, C. White, and J. Colburn, "Wideband artificial magnetic conductors loaded with non–Foster negative inductors," *Antennas and Wireless Propagation Letters, IEEE*, vol. 10, pp. 1586–1589, 2011.

[2] A. Alù, N. Engheta, A. Erentok, and R. W. Ziolkowski, "Single-negative, double-negative, and low-index metamaterials and their electromagnetic applications," *Antennas and Propagation Magazine, IEEE*, vol. 49, no. 1, pp. 23–36, 2007.

[3] J. B. Pendry, "Negative refraction makes a perfect lens," *Physical Review Letters*, vol. 85, no. 18, pp. 3966–3969, 2000.

[4] D. Schurig, J. J. Mock, B. J. Justice, S. A. Cummer, J. B. Pendry, A. F. Starr, and D. R. Smith, "Metamaterial Electromagnetic Cloak at Microwave Frequencies," *Science*, no. 5801, pp. 977–980.

[5] V. Veselago, "The electrodynamics of substances with simultaneously negative values of epsilon and mu," *Sov. Phys. Usp.*, vol. 10, pp. 509–514, 1968.

[6] J. Pendry, A. Holden, D. Robbins, and W. Stewart, "Magnetism from conductors and enhanced nonlinear phenomena," *Microwave Theory and Techniques, IEEE Transactions on*, vol. 47, no. 11, pp. 2075–2084, Nov. 1999.

[7] D. R. Smith, W. J. Padilla, D. C. Vier, S. C. Nemat-Nasser, and S. Schultz, "Composite medium with simultaneously negative permeability and permittivity," *Phys. Rev. Lett.*, vol. 84, no. 18, pp. 4184–4187, May 2000.

[8] T. P. Weldon, K. Miehle, R. S. Adams, and K. Daneshvar, "A wideband microwave double-negative metamaterial with non-Foster loading," in *Southeast-Con, 2012 Proceedings of IEEE*, Mar. 2012, pp. 1–5.

[9] K. L. Smith, T. P. Weldon, and R. S. Adams, "Measurement, simulation, and theory of a non-foster unit cell with parasitic resistance," to appear in Antennas and Propagation Society International Symposium (APSURSI), 2015 IEEE.

[10] R. Ziolkowski, "Design, fabrication, and testing of double negative metamaterials," *IEEE Trans. Antennas Propag.*, vol. 51, no. 7, pp. 1516–1529, Jul. 2003.

[11] R. A. Shelby, D. R. Smith, and S. Schultz, "Experimental verification of a negative index of refraction," *Science*, vol. 292, no. 5514, pp. 77–79, 2001.

[12] K. Miehle, T. Weldon, R. Adams, and K. Daneshvar, "Wideband negative permeability metamaterial with non-Foster compensation of parasitic capacitance," in *Antennas and Propagation Society International Symposium (APSURSI), 2012 IEEE*, Jul. 2012, pp. 1–2.

[13] K. Smith, R. Adams, and T. Weldon, "A novel broadband fractal metamaterial unit cell," in *Antennas and Propagation Society International Symposium (APSURSI), 2014 IEEE*, July 2014, pp. 549–550.

[14] F. Miyamaru, Y. Saito, M. W. Takeda, B. Hou, L. Liu, W. Wen, and P. Sheng, "Terahertz electric response of fractal metamaterial structures," *Physical Review B*, vol. 77, pp. 045 124.1–045 124.6, 2008.

[15] R. Liu, A. Degiron, J. J. Mock, and D. R. Smith, *Applied Physics Letters*, no. 26, p. 263504.

[16] K. L. Smith and R. S. Adams, "A novel ultra-wideband fractal monopole antenna," to appear in Antennas and Propagation Society International Symposium (APSURSI), 2015 IEEE.

[17] C. A. Balanis, *Advanced Engineering Electromagnetics*, 2nd ed. John Wiley and Sons, Inc., 2012.

[18] D. M. Pozar, *Microwave Engineering*, 4th ed. John Wiley and Sons, Inc., 2012.

[19] J. B. Pendry, D. Schurig, and D. R. Smith, "Controlling Electromagnetic Fields," *Science*, vol. 312, no. 5781, pp. 1780–1782, 2006.

[20] J. B. Pendry, "Time Reversal and Negative Refraction," *Science*, vol. 322, no. 5898, pp. 71–73, 2008.

[21] P. K. Martin W. McCall, Alberto Favaro and A. Boardman, "A spacetime cloak, or a history editor," *Journal of Optics*, vol. 13, no. 2, pp. 024 003.1–024 003.9, February 2011.

[22] R. M. Foster, "A reactance theorem," *Bell Syst. Tech. J.*, vol. 3, pp. 259–267, 1924.

[23] J. Linvill, "Transistor negative-impedance converters," *Proceedings of the IRE*, vol. 41, no. 6, pp. 725–729, Jun. 1953.

[24] J. Covington, K. Smith, V. Kshatri, J. Shehan, T. Weldon, and R. Adams, "A cross-coupled CMOS negative capacitor for wideband metamaterial applications," in *Southeastcon, 2014 Proceedings of IEEE*, Mar. 2014, pp. 1–4.

[25] J. Covington, K. Smith, J. Shehan, V. Kshatri, T. Weldon, and R. Adams, "Measurement of a CMOS negative inductor for wideband non-Foster metamaterials," in *Southeastcon, 2014 Proceedings of IEEE*, Mar. 2014, pp. 1–4.

[26] V. Kshatri, J. Covington, K. Smith, J. Shehan, T. Weldon, and R. Adams, "Measurement and simulation of a CMOS current conveyor negative capacitor for metamaterials," in *Southeastcon, 2014 Proceedings of IEEE*, Mar. 2014, pp. 1–4.

[27] B. B. Mandelbrot, *The fractal geometry of nature.* Macmillan, 1983.

[28] L. F. Richardson, "The problem of contiguity," *General systems yearbook*, vol. 6, pp. 139–187, 1961.

[29] J. Sullivan, "Fractal broccoli," 2004, [accessed 4-March-2015]. [Online]. Available: http://en.wikipedia.org/wiki/Romanesco_broccoli#mediaviewer/File:Fractal_Broccoli.jpg

[30] Wikipedia, "Fern frond trichomes," 2010, [accessed 4-March-2015]. [Online]. Available: http://upload.wikimedia.org/wikipedia/commons/0/01/Fern_Frond_Trichomes.jpg

[31] H. von Koch, "Sur une courbe continue sans tangente, obtenue par une construction géométrique élémentaire," *Arkiv för Matematk*, vol. 1, pp. 681–704, 1904.

[32] M. Sierpinski, "Sur une courbe dont tout point est un point de ramification," *Compte Rendus hebdomadaires des séances de l´Académie des Science de Paris*, vol. 160, pp. 302–305, 1915.

[33] C. Puente-Baliarda, J. Romeu, R. Pous, and A. Cardama, "On the behavior of the Sierpinski multiband fractal antenna," *IEEE Transactions on Antennas and Propagation*, vol. 46, no. 4, pp. 517–524, April 1998.

[34] G. Liu, L. Xu, and Z. Wu, "Miniaturized circularly polarized microstrip RFID antenna using fractal metamaterial," *International Journal of Antennas and Propagation*, vol. 2013, pp. 1–4, Jul. 2013.

[35] V. Crnojević-Bengin, V. Radonić, and B. Jokanović, "Fractal geometries of complementary split-ring resonators," *Microwave Theory and Techniques, IEEE Transactions on*, vol. 56, no. 10, pp. 2312–2321, Oct. 2008.

[36] R. Mathur, S. Joshi, and K. C. Roy, "A novel multiband Koch loop antenna using fractal geometry for wireless communication system," *International Journal of Wireless & Mobile Networks*, vol. 3, no. 5, 2011.

[37] C. P. Baliarda, J. Romeu, and A. Cardama, "The Koch monopole: A small fractal antenna," *IEEE Transactions on Antennas and Propagation*, vol. 48, no. 11, pp. 1773–1781, November 2000.

[38] M. Naser-Moghadasi, R. A. Sadeghzadeh, T. Aribi, T. Sedghi, and B. S. Virdee, "UWB monopole microstrip antenna using fractal tree unit-cells," *Microwave and Optical Technology Letters*, vol. 54, no. 10, pp. 2366–2370, October 2012.

[39] J. Pourahmadazar, C. Ghobadi, and J. Nourinia, "Novel modified pythagorean tree fractal monopole antennas for UWB applications," *IEEE Antennas and Wireless Propagation Letters*, vol. 10, pp. 484–487, May 2011.

[40] J. S. Petko and D. H. Werner, "Miniature reconfigurable three-dimensional fractal tree antennas," *IEEE Transactions Antennas and Propagation*, vol. 52, no. 8, pp. 1945–1956, August 2004.

[41] K. Smith, R. Adams, and T. Weldon, "A novel broadband fractal metamaterial unit cell," in *Antennas and Propagation Society International Symposium (APSURSI), 2014 IEEE*, July 2014, pp. 549–550.

[42] S. Arslanagic, T. Hansen, N. Mortensen, A. Gregersen, O. Sigmund, R. Ziolkowski, and O. Breinbjerg, "A review of the scattering-parameter extraction method with clarification of ambiguity issues in relation to metamaterial homogenization," vol. 55, no. 2, pp. 91–106, Apr. 2013.

[43] Z. Szabó and, G.-H. Park, R. Hedge, and E.-P. Li, "A unique extraction of metamaterial parameters based on Kramers-Kronig relationship," *Microwave Theory and Techniques, IEEE Transactions on*, vol. 58, no. 10, pp. 2646–2653, Oct. 2010.

[44] H.-X. Xu, G.-M. Wang, and Q. Peng, "Fractal-shaped complementary electric-lc resonator for bandstop filter," *Progress In Electromagnetics Research C*, vol. 23, pp. 205–217, 2011.

[45] J. W. Shehan, R. S. Adams, and T. Weldon, "Metamaterial measurement in a cylindrical coaxial fixture with consideration for inter-element coupling," in *IEEE Radio Science Meeting*, Memphis, TN, July 2014, p. 138.

APPENDIX A: MEASUREMENT FIXTURE

The cylindrical fixture in which the metamaterial structures described in Chapter 3 were measured is described here, along with standards to allow Thru-Reflect-Line (TRL) calibration. Each of the Thru and Reflect standards, as well as the Measurement fixture, was designed as a collection of several smaller pieces that could be 3D printed individually, covered in 0.005" copper foil from Online Metals, part # 110 060, and fitted together into a cohesive whole for measurement. The empty Measurement fixture doubled as the Line standard.

The small ends of each inner taper were inset with soft copper tubes from Hobby Lobby, having outer diameter 4 mm and tube thickness 0.1 mm. This tube was frayed on the outside edge, and the frayed pieces were splayed back at the end of the taper piece, to allow a solid connection to the N-connector, as shown in Fig. A.1.

Figure A.1: Photo of connection between N-connector and 3D printed taper.

The twelve necessary pieces are listed in Table A.1, and the geometry and dimensions of each are presented in Figs. A.2–A.13. The configurations of the Thru, Reflect, and Measurement/Line standards are shown in Figs. A.14–A.16. The final 3D printed Thru, Reflect, and Measurement/Line standards are shown in Figs. A.17–A.19, as well as the bolt and metal-plate devices that were used to press-fit each standard together.

Table A.1: Pieces for measurement fixture

Part #	Part Name	Quantity Needed
1	Outer Taper	5
2	Inner Taper	5
3	Outer Connector	5
4	Inner Connector	5
5	End Washer	5
6	Outer Measurement Section	1
7	Inner Measurement Section	1
8	Outer Thru Section	1
9	Inner Thru Section	1
10	Outer Reflect Section	1
11	Inner Reflect Section	1
12	Reflect Cap	1

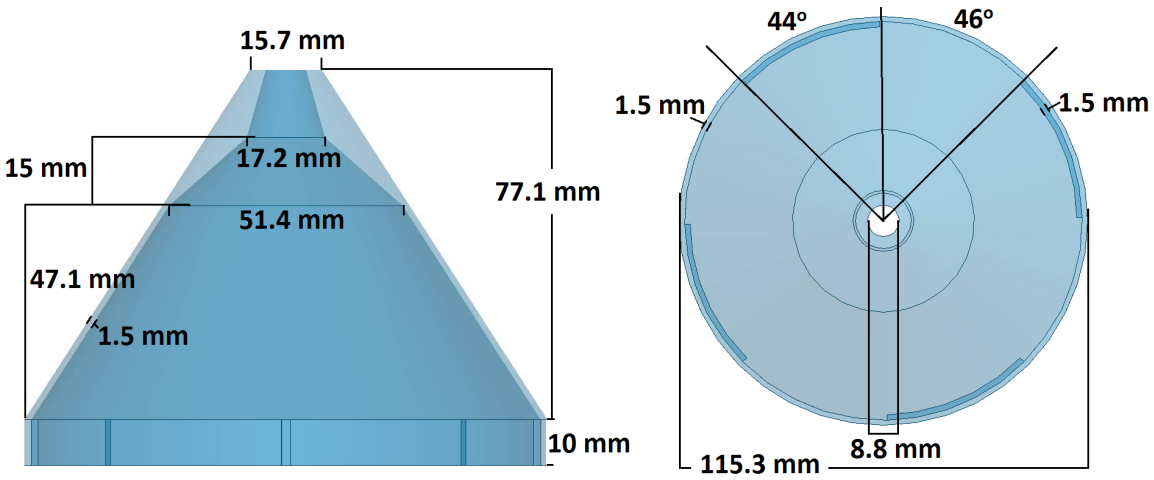

Figure A.2: Part #1: The outer taper.

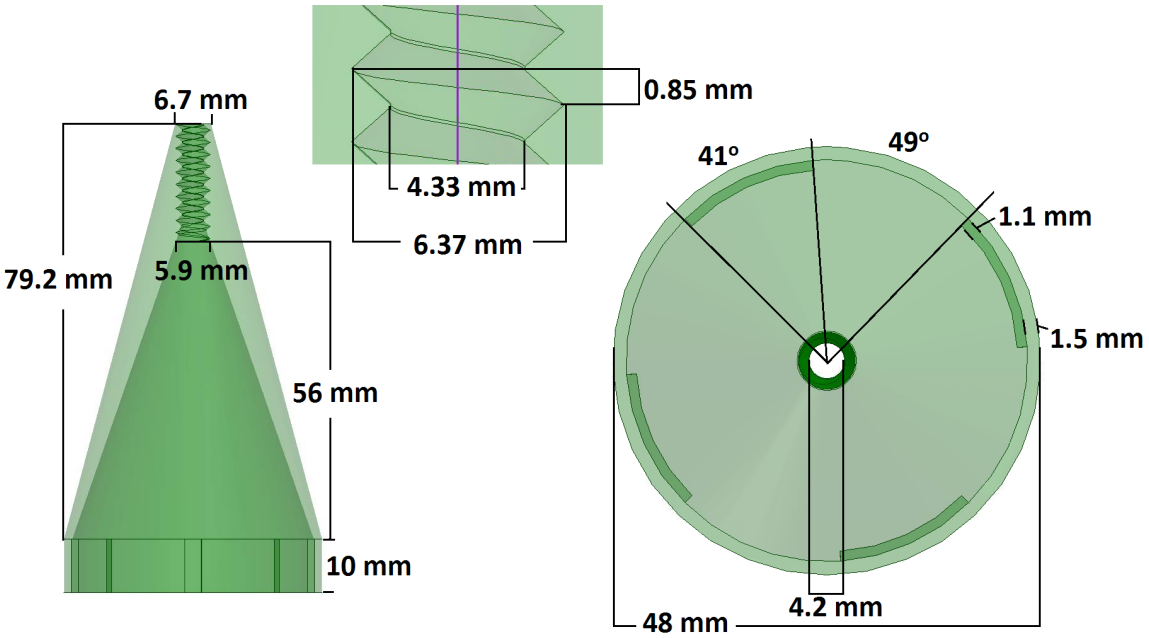

Figure A.3: Part #2: The inner taper.

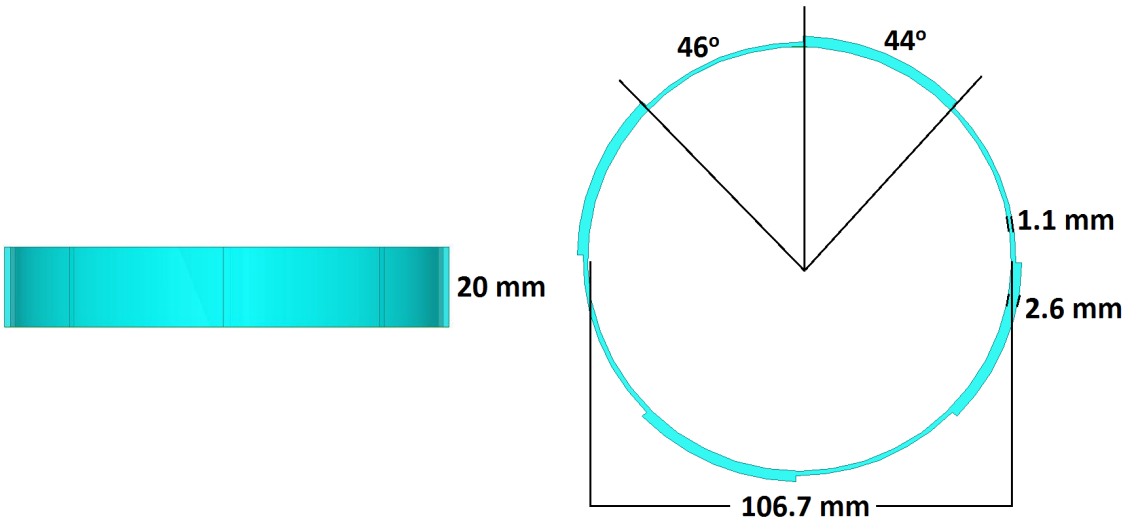

Figure A.4: Part #3: The outer connector.

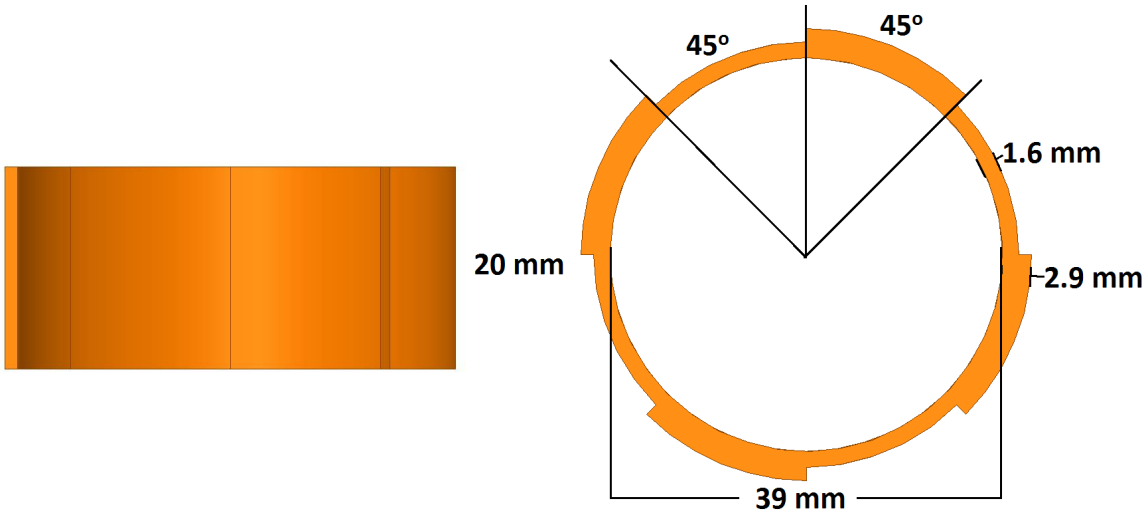

Figure A.5: Part #4: The inner connector.

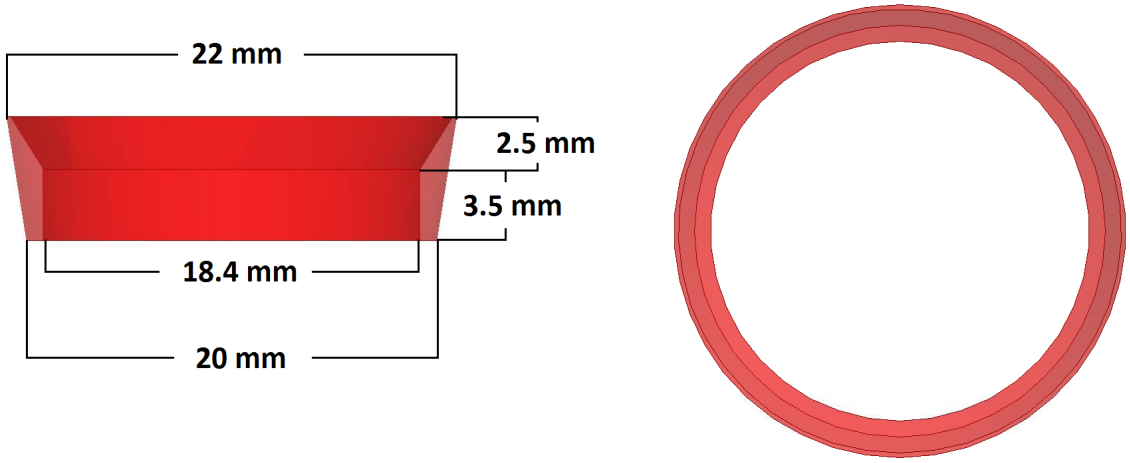

Figure A.6: Part #5: The end washer.

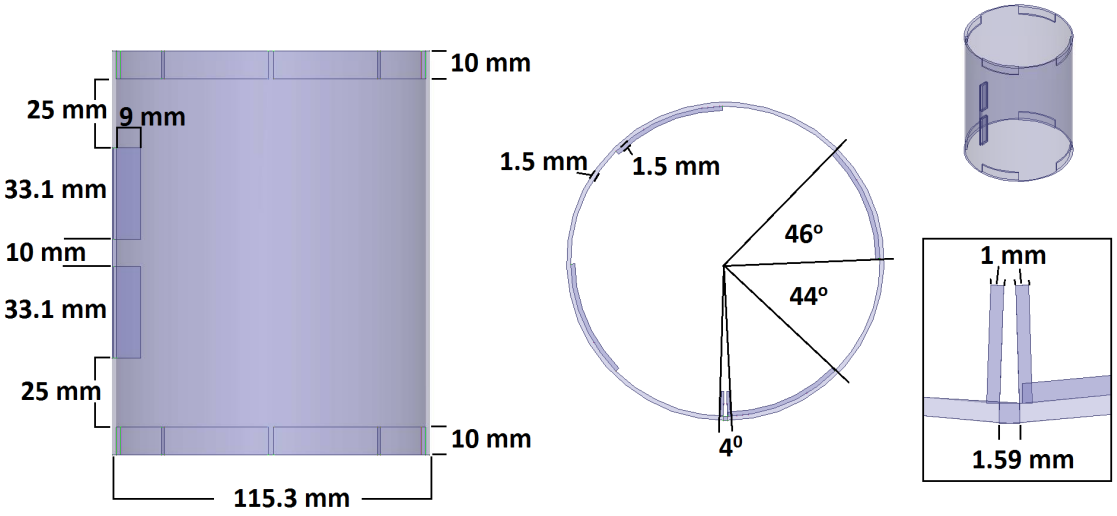

Figure A.7: Part #6: The outer Measurement section.

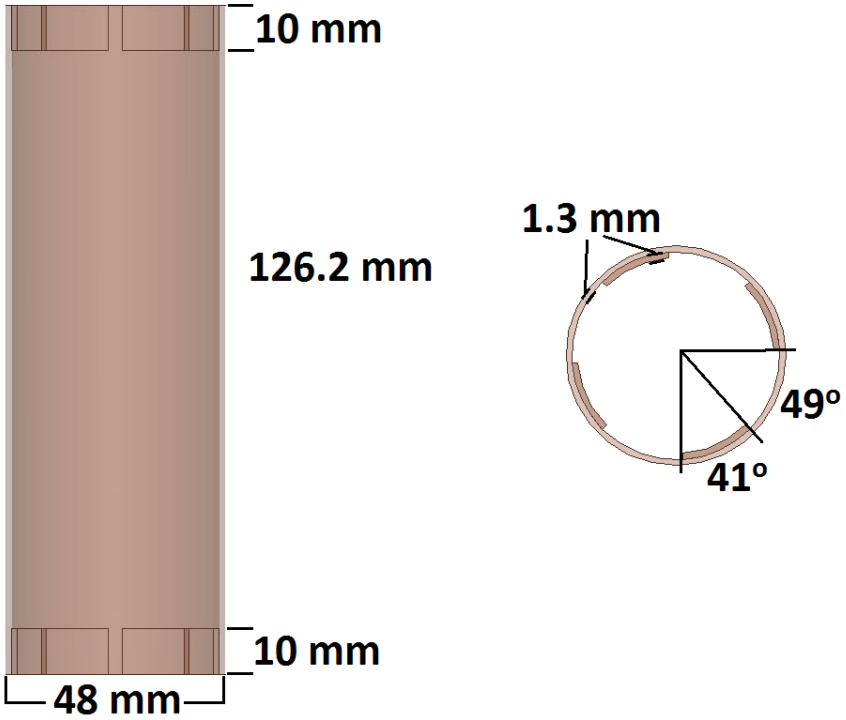

Figure A.8: Part #7: The inner Measurement section.

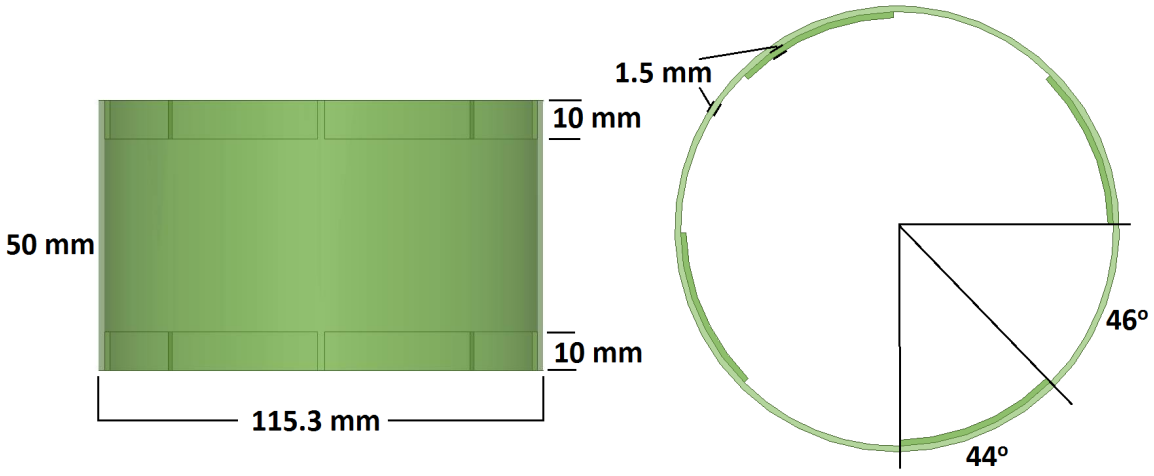

Figure A.9: Part #8: The outer Thru section.

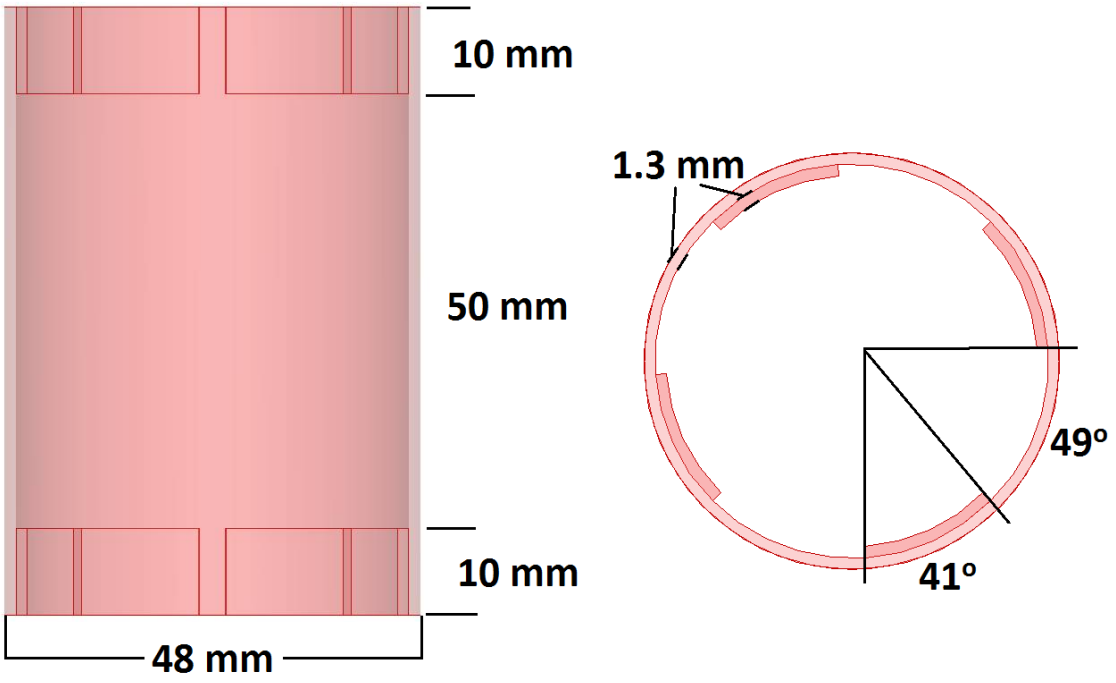

Figure A.10: Part #9: The inner Thru section.

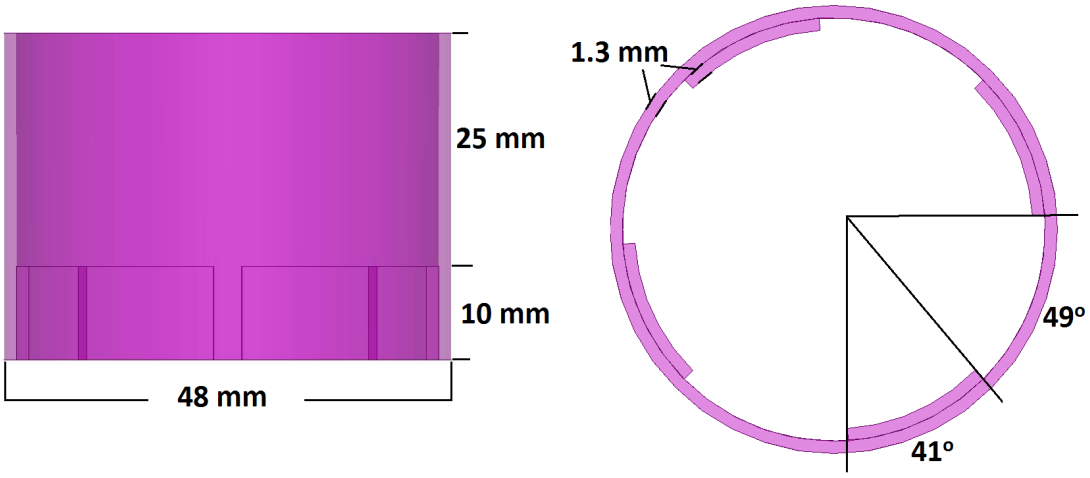

Figure A.11: Part #10: The inner Reflect section.

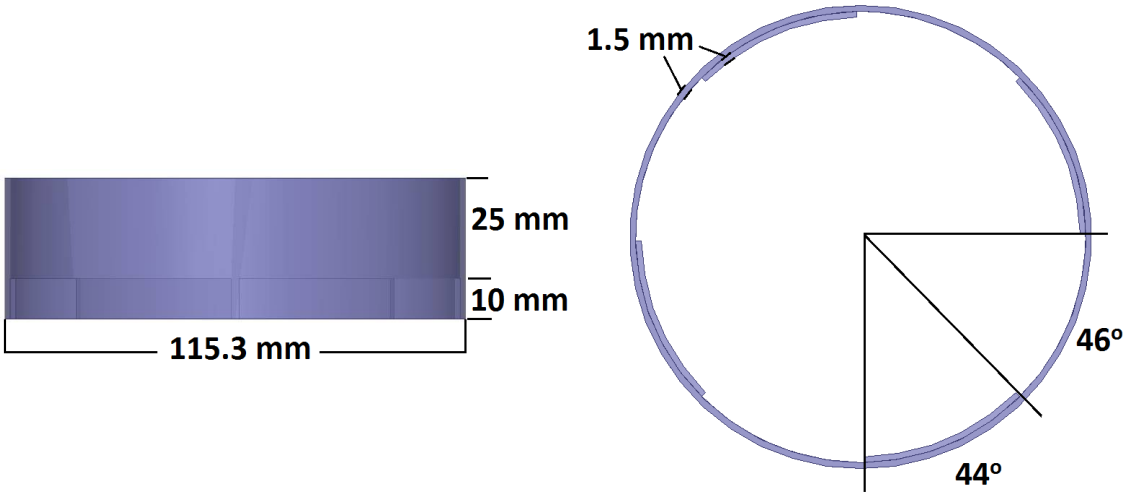

Figure A.12: Part #11: The outer Reflect section.

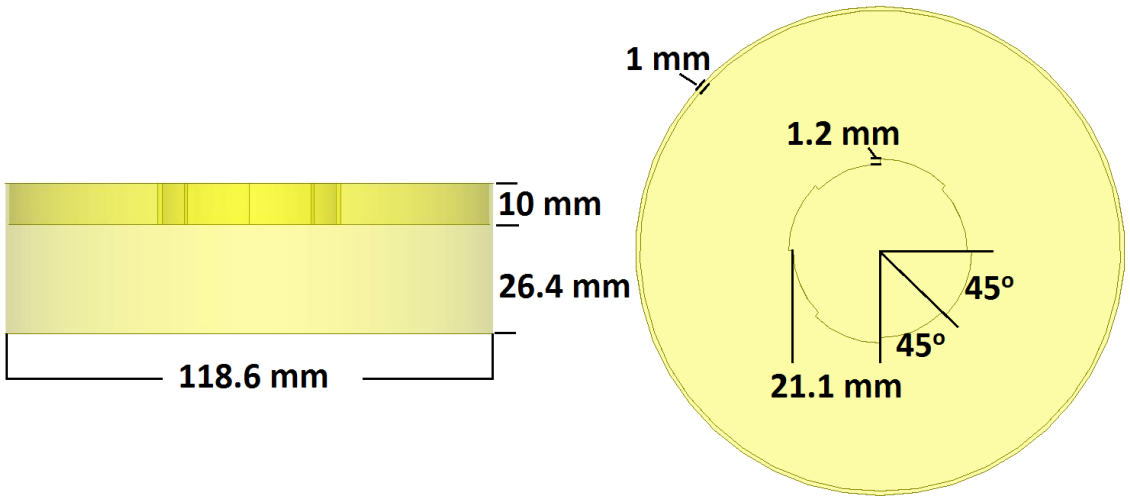

Figure A.13: Part #12: The Reflect cap.

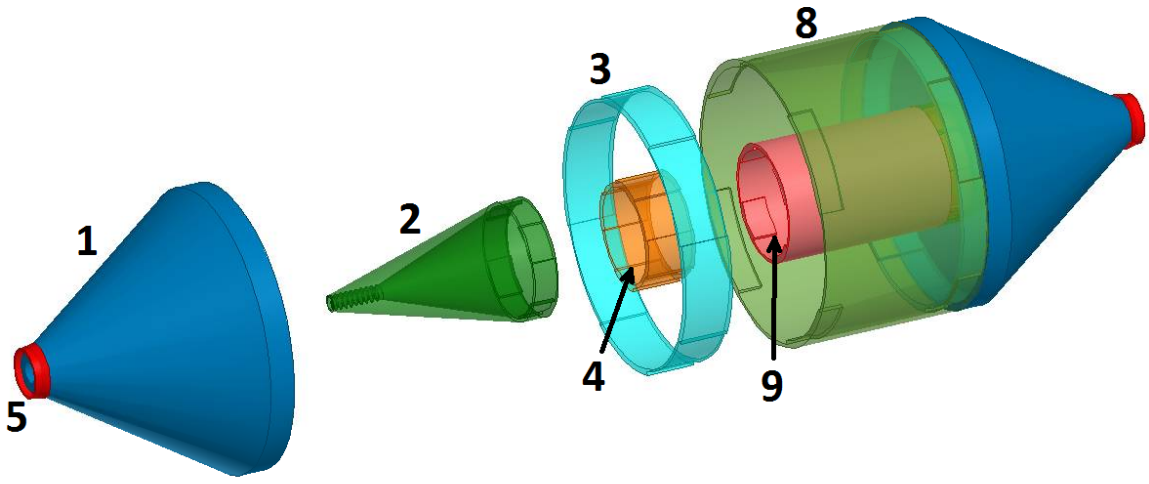

Figure A.14: The Thru configuration.

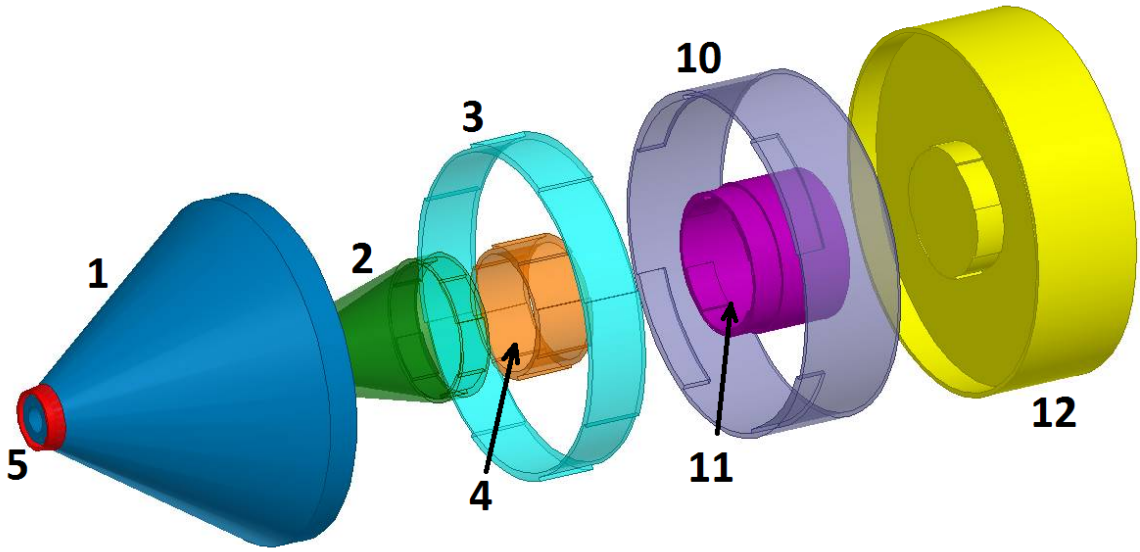

Figure A.15: The Reflect configuration.

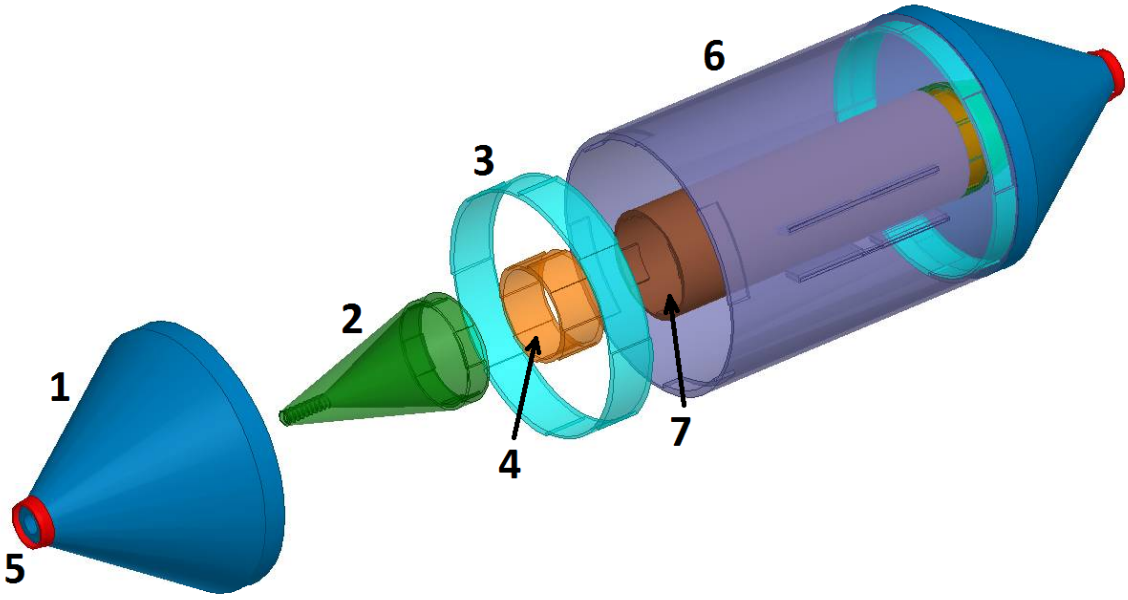

Figure A.16: The Measurement/Line configuration.

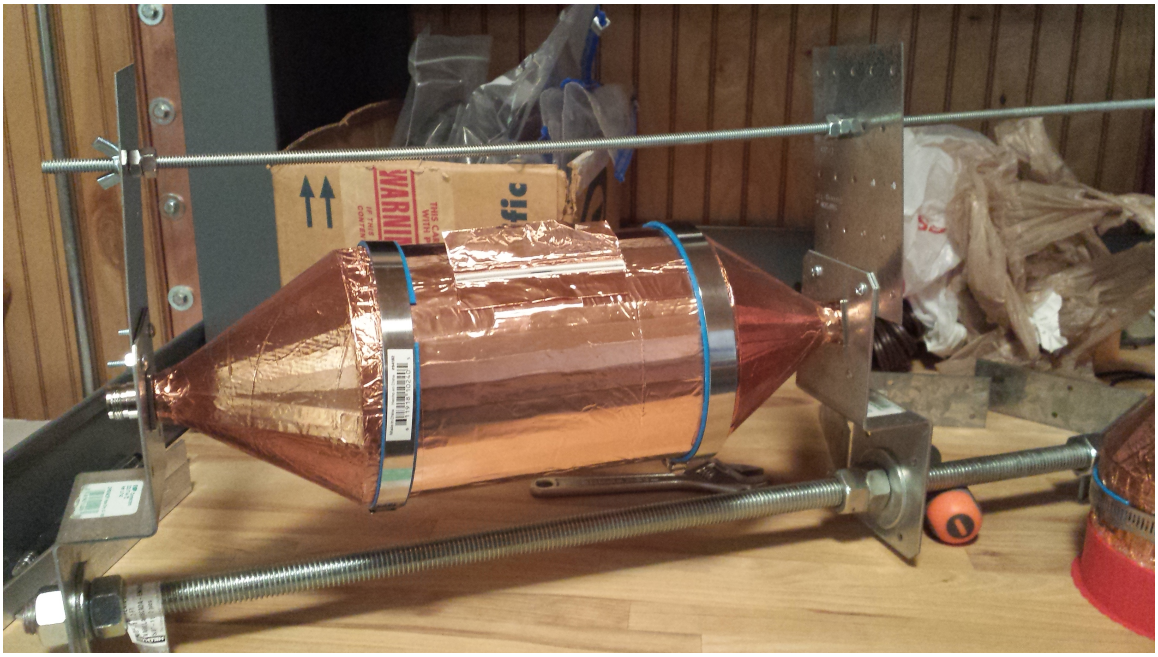

Figure A.17: Photo of the completed measurement fixture/Line standard.

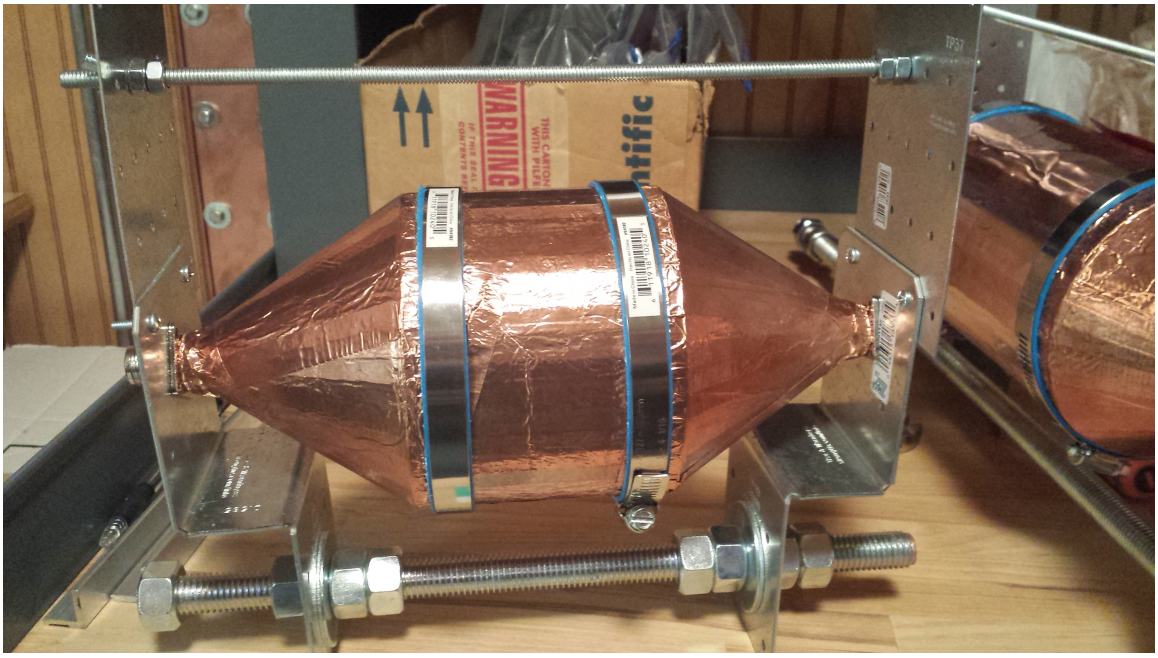

Figure A.18: Photo of the completed Thru standard.

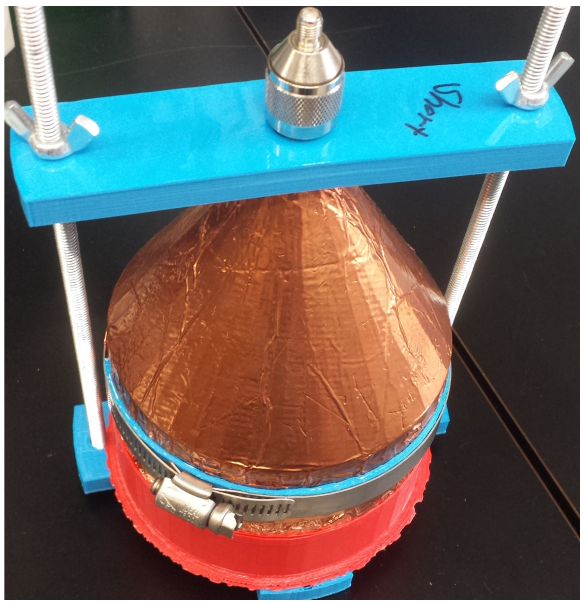

Figure A.19: Photo of the completed Reflect standard.